LAGRANGIAN INVESTIGATIONS OF TURBULENT DISPERSION AND MIXING USING PETASCALE COMPUTING

A Thesis
Presented to
The Academic Faculty

by

Dhawal Buaria

In Partial Fulfillment
of the Requirements for the Degree
Doctor of Philosophy in the
School of Aerospace Engineering

Georgia Institute of Technology
August 2016

LAGRANGIAN INVESTIGATIONS OF TURBULENT DISPERSION AND MIXING USING PETASCALE COMPUTING

Approved by:

Prof. P. K. Yeung, Advisor
School of Aerospace Engineering
Georgia Institute of Technology

Prof. Stephen Ruffin
School of Aerospace Engineering
Georgia Institute of Technology

Prof. Edmund Chow
School of Computational Science and Engineering
Georgia Institute of Technology

Prof. Suresh Menon
School of Aerospace Engineering
Georgia Institute of Technology

Prof. Donald Webster
School of Civil Engineering
Georgia Institute of Technology

Date Approved: May 2016

To my beloved parents

ACKNOWLEDGEMENTS

This work was supported by the Fluid Dynamics Program of the National Science Foundation (NSF), under Grant CBET-1235906. The computations and data analyses reported in this thesis were performed primarily using advanced computational facilities provided by the Texas Advanced Computation Center (TACC) under the XSEDE program supported by NSF and the Blue Waters project at the University of Illinois at Urbana-Champaign under the Petascale Resource Allocations program supported by NSF, via Grant ACI-1036170. We also used resources provided by Oak Ridge National Laboratories (ORNL), the National Energy Research Scientific Computing Center (NERSC) and the National Institute for Computational Sciences (NICS). We would also like to acknowledge the Extended Collaborative Support Service (ECSS) project under the XSEDE program.

I would like to express my deepest gratitude to my advisor, Prof. P.K. Yeung, for his support and guidance throughout this work. He has taught me, both consciously and unconsciously, how to be a good researcher and a critical thinker. His work ethic, dedication, humility, attention to details, constant striving for high-quality research and numerous other traits, have been and will always continue to be a source of inspiration. I am also grateful to him for providing the opportunities to interact and work with many highly respected researchers in the field, most notably Prof. Brian Sawford. I am much grateful to Prof. Sawford for constantly providing invaluable feedback and direction to my research work. His deep understanding of the field, kindness and keen eye for the smallest of details has without any doubt greatly enhanced the quality of this work. It also has been a great honor to have published alongside him and Prof. Yeung. Though my stay at Georgia Tech will soon come to an end, I hope to continue to learn from them for the rest of my life.

I would like to thank the help from all the consultants at the different supercomputing centers, most notably, Lars Koesterke (TACC) for his constant help through the ECSS project, Jing Li, Robert Fiedler and everyone else at NCSA, who have always been quick to

help with any issues on Blue Waters and Jeff Larkin (NVIDIA) for providing some invaluable insights related to GPUs and OpenACC.

I would like to extend my appreciation to my committee members, Professors S. Ruffin, E. Chow, S. Menon and D. Webster for taking the time to review my work. I am also thankful to Professors V. Yang and J. Jagoda for their support during my master's degree preceding this work. I am also grateful to all the professors whose have positively influenced me through the courses I have taken at Georgia Tech. It was a wonderful experience to learn from them. Special thanks to my labmates, Kartik, Shine, Matthew and Jacob for keeping me on my toes with all the intriguing questions and discussions and in general for their help with everything. I am forever indebted to all my friends for accompanying me through what has been a hell of a roller coaster ride. The list is too long to enumerate, but I will always remember their help and the moments that I shared with them.

Most importantly, none of this would have been possible without the love and patience of my family. I am very grateful to my brother Minesh and my sister-in-law Pooja for their constant love and encouragement. My adorable niece Prapti, constantly reminds me of all the innocent little things which we forget to cherish as adults. Lastly, I dedicate this thesis to my parents, whose unconditional love and unbounded support are the pillars of my every accomplishment.

TABLE OF CONTENTS

LIST OF TABLES

LIST OF FIGURES

SUMMARY

In many fields of science and engineering important to society, such as study of air and water quality, pollutant dispersion, cloud physics, design of improved combustion devices, etc., the ability of turbulent flow to provide efficient transport of entities such as pollutants, vapor droplets, fuel and oxidizer, etc. is of critical importance. To understand and hence develop proper predictive tools for such transported entities it is necessary to understand turbulence from a Lagrangian perspective (of an observer moving with the flow), including the interaction between turbulent transport and molecular diffusion. Usually, in both direct numerical simulations (DNS) and experiments, a population of fluid particles is tracked forward in time (forward tracking) from specified initial conditions to understand how a cloud of material spreads in a turbulent flow. However, the process of turbulent mixing occurs when material from different regions is brought together at a later time. In such a scenario, it is more important to track the particles backward in time (backward tracking). Backward tracking is also important from a modeling perspective, which would help address questions about the dynamical origins of a patch of contaminant material, or a highly convoluted multi-particle cluster. Furthermore, it can also be shown that the n^{th} moment of a passive scalar field can be directly related to the backward in time statistics of an n-particle cluster. Although conceptually simple, backward tracking is very difficult to accomplish due to time irreversibility of Navier-Stokes equations, and thus not very well understood in literature.

In this work, DNS of stationary isotropic turbulence is performed to investigate the fundamental differences between forward and backward dispersion. A new massively parallel algorithm using one-sided communication has been developed and applied to enable particle tracking in DNS at Petascale problem sizes. Simulations up to 4096^3 in size with more than 100 million particles have been performed, while a new simulation with 8192^3 grid

points with 300 million particles on $262,144$ processors is currently underway. Also a new massively parallel postprocessing algorithm is developed and applied to obtain well-sampled backward and forward statistics of pairs and clusters of fluid particles and molecules that undergo Brownian motion relative to the fluid.

Detailed results are first obtained for pairs of fluid particles, over a range of initial separations ranging from Kolmogorov to energy-containing scales and up to Taylor-scale Reynolds numbers (R_λ) of 1000, which is higher than in recent work in the literature. Backward dispersion is faster, especially at intermediate times, after the ballistic range and before the long-time diffusive behavior is reached. Richardson scaling has been demonstrated for the mean-squared separation, and the forward and backward Richardson constants are estimated to be 0.55 and 1.5 respectively, which are close to or comparable to other estimates. Extensions to higher order moments of the separation are also investigated. Analysis of the so-called distance-neighbor function showed only transitory agreement with the well-known Richardson prediction. The predicted asymmetry between backward and forward relative displacements at early times, manifested in a t^3 variation, was confirmed numerically and explicitly traced to Eulerian property at the small scales. However, this t^3 growth is not simply connected to the t^3 growth in the Richardson regime and the asymmetry manifested there by the difference in the backward and forward Richardson constants. Asymmetry in time for higher order moments is also explained using a Taylor-series analysis at small times.

Statistics of the trajectories of molecules diffusing via Brownian motion, are obtained for Schmidt numbers (Sc) from 0.001 to 1000 at Taylor-scale Reynolds number up to 1000. Statistics of displacements of single molecules compare well with the earlier theoretical work of Saffman (*J. Fluid Mech.* **8**, 273-283, 1960) except for the scaling of the integral time scale of the fluid velocity following the molecular trajectories. For molecular pairs we extend Saffman's theory to include pairs of small but finite initial separation, in excellent agreement with numerical results provided data are collected at sufficiently small times. At intermediate times the separation statistics of molecular pairs exhibit a more robust Richardson scaling behavior than for the fluid particles. The forward scaling constant is

very close to 0.55, whereas the backward constant is about 1.53–1.57, with a weak Schmidt number dependence, although no scaling exists if $Sc \ll 1$, at the Reynolds numbers presently accessible. An important innovation in this work is to demonstrate explicitly the practical utility of a Lagrangian description of turbulent mixing, where molecular displacements and separations in the limit of small backward initial separation can be used to calculate the evolution of scalar fluctuations resulting from a known source function in space. Lagrangian calculations of production and dissipation rates of the scalar fluctuations are shown to agree very well with Eulerian results for the case of passive scalars driven by a uniform mean gradient. Although the Eulerian-Lagrangian comparisons are made only for $Sc \sim \mathcal{O}(1)$, the Lagrangian approach is more easily extended to both very low and very high Schmidt numbers. The well known scalar dissipation anomaly is accordingly also addressed in a Lagrangian context.

Some results for dispersion of four-particle clusters (tetrads) are also reported. The statistics of tetrad size, namely volume (V) and gyration radius (R), are qualitatively similar to that of the mean-square separation of particle pairs, i.e., stronger backward dispersion at intermediate times with larger backward Richardson constant. The statistics of tetrad shape show more robust inertial range scaling compared to the statistics of tetrad size. The general behavior of forward and backward statistics of tetrad shape, further suggests that the distorting effects of turbulence at intermediate times are stronger in the backward frame.

Extensions of the current work to study of, for example, clusters of molecules, velocity gradients following fluid particles, inertial particles, etc. are also addressed.

CHAPTER I

INTRODUCTION

1.1 Background and Motivation

Turbulence is the most common state of fluid motion both in nature and engineering. Understanding of turbulence is essential for a range of applications such as atmospheric sciences, oceanography, pollutant transport, cloud physics, aerospace vehicles, combustion devices, etc. Turbulent flows are characterized by disorderly fluctuations spanning a wide range of scales in time and three-dimensional (3D) space, resulting in a set of governing equations, the Navier-Stokes equations, which are highly non-linear and stochastic in nature. Because of these complexities, the study of turbulence is very challenging (Lumley & Yaglom 2001) and still remains a major 'unsolved' problem in classical physics (Sreenivasan 1999). It is clear that theory, computations and experiments (Warhaft 2009) are all important in turbulence research. However, in recent years advances in high-performance computing (Ishihara *et al.* 2009) have led to increasing opportunities for understanding flow physics at a degree of detail surpassing most experiments.

All turbulent flows are characterized by a high Reynolds number $Re = ul/\nu$, where u and l are the characteristic velocity and length scales of the flow and ν is the kinematic viscosity of the fluid. Due to the non-linear interactions arising from inertial motions, larger eddies in the flow progressively break down into smaller and smaller eddies, until they are small enough to be dissipated by the viscosity (Richardson 1926). This results in an energy cascade from the largest to the smallest scales of motion, at a rate controlled by the mean dissipation rate of the turbulent kinetic energy. Since the largest scales are characterized by u and l, the Reynolds number quantifies the range of scales in the flow and hence also the extent of the energy cascade. A fundamental question in the study of turbulence is how these wide range of scales behave and interact with each other. Since a deterministic approach is almost impossible, one has to rely on similarity scaling to devise a statistical description of turbulence. The most well-known theory in this regard is that of Kolmogorov (1941), which hereafter will be referred to as K41. The first hypothesis of K41 states that, in all turbulent flows at sufficiently high Reynolds number, the small scales are locally isotropic regardless of the nature of large scales and their statistics have an universal form completely determined by the mean dissipation rate and the kinematic viscosity. The second hypothesis states that at sufficiently higher Reynolds number there exists an intermediate range of scales (the so-called inertial subrange) between the large scales and the smallest scales, such that the statistics are further independent of viscosity (and hence depend only on the mean dissipation rate). This universality allows us to treat all turbulent flows at high Reynolds number in a similar fashion, often leading to simple algebraic statistical expressions. This greatly simplifies the analysis and prediction of otherwise complex flows.

Many important problems in environmental science related to air and water quality and cloud physics are tied to the transport of contaminants, particulate matter, water vapor droplets and other entities in a turbulent flow. These transport processes often involve complex interactions such as those between turbulence and multiphase flow, or between turbulence and buoyancy and atmospheric dynamics. However the key element of advective transport by turbulence is naturally described using a Lagrangian viewpoint of fluid mechanics (Monin & Yaglom 1971, 1975). In the Lagrangian approach, we consider the flow from the viewpoint of an observer traveling along with a large number of infinitesimal material fluid elements, usually referred to as fluid particles (also called passive tracers in literature). In effect, the continuum fluid motion is represented by a collection of discrete fluid particles, which are of zero size and move with local flow velocity (Yeung 2002). The concept can also be applied to Brownian particles or "molecules" which move due to the combined effects of the fluid motion and of molecular diffusion, and to inertial particles whose trajectories differ from those of fluid particles because of the effects of inertia and gravitational settling or buoyancy (Sawford & Pinton 2013). This approach is in contrast to the typical Eulerian approach, where the motion of the fluid is treated as a continuum and measurements (in experiments or numerical simulations) are made at fixed spatial locations at various time instants in a stationary inertial frame. The Lagrangian description is also more useful in capturing the temporal evolution of a turbulent flow, as it is not affected by large-scale turbulence sweeping (Tennekes 1975; L'vov *et al.* 1997). Several reviews covering a broad range of modern Lagrangian approaches have been given by Sawford (2001), Yeung (2002), Salazar & Collins (2009) and Toschi & Bodenschatz (2009).

The Lagrangian approach to study turbulent dispersion goes back at least as far as the work of Taylor (1921), who studied the statistics of of displacement of a single fluid particle and first introduced the Lagrangian velocity autocorrelation function. Soon later, Richardson (1926) studied the dispersion of particle pairs relative to each other and observed the first signs of universal inertial range scaling, which paved the way for the K41 theory. While these earlier Lagrangian investigations were aimed at understanding turbulent dispersion, Batchelor (1949, 1952*a*) established direct connections between Lagrangian statistics and turbulent mixing of passively diffusing scalars. He showed that the statistics of fluid particle motion can determine the mean concentration field of a scalar, whereas two-particles statistics can determine the variance of the concentration for any random source distribution (Corrsin 1952; Batchelor 1952*a*). Many other classical ideas, including the application of K41 theory to Lagrangian statistics, were summarized by Monin & Yaglom (1971, 1975). In the past few decades, the Lagrangian viewpoint has been expanded to stochastic modeling of many practical dispersion and mixing applications, covering environmental problems in the atmosphere (Sawford 1985, 1993, 2001; Wilson & Sawford 1996; Rodean 1996), the oceans (Griffa 1996) and engineering flows (Pope 1994; Meneveau 2011). Thus the Lagrangian viewpoint serves both as an alternative representation of the flow and as a means of developing practical models for turbulent transport of scalar materials.

A fundamental question in the Lagrangian view of turbulent diffusion is, given a cloud of material, how will it spread. To answer this question it is usual to track a collection of particles forward in time, i.e. to set initial positions at some time $t = 0$ and follow their subsequent trajectories, over some suitably long period of observation (T). This is convenient both in numerical simulations based on advancing the velocity field forwards in time according to the Navier Stokes equations, and in experiments where some tracer material is released in a controlled manner upstream of the observation volume. However, provided the density is constant, at the same time as fluid elements move apart (becoming dispersed from one another), other fluid particles initially far apart will also have a chance to come into close proximity of each other — leading to mixing of local inhomogeneities in the flow. In the latter case, instead of focusing on a source and asking where the material under consideration will go, we need to trace back in time to determine the origins of some observed material and ask where it came from. In such a scenario, it is more relevant to study the trajectories of fluid particles inverse in time, given their final location. This idea of describing the statistics of particle positions at times earlier than a prescribed labeling time is known as backward tracking and is crucial in formulating the Lagrangian description of turbulent mixing (Sawford & Pinton 2013). Fundamentally at the molecular level, dispersion and mixing are the same process. In problems related to dispersion, it is usually desirable to know how some material will spread or 'disperse', whereas in mixing it is desirable to understand how material from different regions comes together to 'mix'. Hence in the latter case, from a Lagrangian viewpoint, it is very convenient to start the observation at the final time at which the molecules arrive from different regions, reversing the temporal axis to trace back in time the trajectories of these molecules. In effect, the mixing process at a given observation time, now can be described as a dispersion process traced backward to earlier times. As discussed in details in Chapter 5 (also see review by Sawford & Pinton (2013)), this reversal of reference frame greatly simplifies the mathematical formulation for turbulent mixing and is also the motivation for many practical models for scalar mixing.

The underlying concept of backward tracking is useful in a myriad of other problems in which the transport or aggregation of particles in turbulence is important. One such important example is the formation of clouds (Shaw 2003; Bodenschatz *et al.* 2010). The formation of clouds is fundamentally governed by two physical processes, (1) formation of water droplets by condensation of water vapor in different regions of atmosphere and (2) transport and coalescence of such droplets (which is controlled by turbulence, buoyancy and various other atmospheric dynamics) leading to formation and growth of clouds. In the latter case, the backward tracking perspective is particularly useful to understand the process of coalescence (Bragg *et al.* 2016). Backward tracking is also useful in problems related to biological spread and growth (Garrett 2003; Garabato *et al.* 2004; Visser 2007; Durham *et al.* 2013). For example, understanding the spread of organisms in oceans or in critical epidemic or bioterrorism-driven situations, when it is important to trace an air- or water-borne pathogen to its origin. Also in many astrophysical applications, such as galaxy formation (Ryu *et al.* 2008; Charbonnel & Talon 2007) and stellar evolution (Humphreys & Davidson 1984; Ward-Thompson 2002), backward tracking is an useful tool. While most of these physical processes are too complex to be simulated directly, the study of backward tracking in simpler settings is nevertheless important in developing high fidelity models applicable to such complex problems.

While the change in reference temporal frame is a simple matter of perspective, it still has major implications on the understanding of the underlying physical process due to time irreversibility of Navier-Stokes equations. Needless to say backward tracking does not involve backward time integration of Navier-Stokes equations, which are not time-reversible. It involves tracking backwards in time, some tracer which can be some invisible pollutant, passive scalar, or airborne pathogen, to determine its origin. Given the final time T, the position of such a tracer is tracked backward in time to its initial position at $t = 0$, while the fluid flow still satisfies the Navier-Stokes as integrated forward from $t = 0$ to $t = T$. As a result, backward tracking is far more challenging in both computations and experiments compared to forward tracking (Sawford *et al.* 2005; Berg *et al.* 2006), even though conceptually it is as simple. In computations, backward tracking can be accomplished if complete velocity fields stored at every time step in a previously-conducted simulation are available. Such a calculation was performed by Sawford *et al.* (2005) on a 64^3 grid at Taylor-scale Reynolds number [1] $R_\lambda = 38$ and more recently on a larger scale by Eyink (2011); Benveniste & Drivas (2014) using a large turbulence database at 1024^3 resolution at $R_\lambda = 433$. This approach allows particles to be tracked back in time from any designated final position and hence provides complete control over final separations of particles or form geometries

---

[1] Taylor-scale Reynolds number is defined as $R_\lambda = u\lambda/\nu$, where λ is the Taylor length scale. The Taylor length scale is defined as $\lambda = \left[\sigma_u^2/\langle(\partial u_1/\partial x_1)^2\rangle\right]^{1/2}$, where σ_u is the root-mean-square velocity component and $\partial u_1/\partial x_1$ is the longitudinal gradient of one velocity component. Both are often used to characterize turbulence, especially in direct numerical simulations.

of desired shapes. However this approach requires velocity fields at N^3 grid points to be stored at a very large number of time steps, such that the total data storage requirement grows as fast as R_λ^6 (similar to the computational cost of DNS as discussed in Chapter 3). As a result at Petascale problem sizes associated with large R_λ, this approach would be unsustainable at even the largest supercomputing installations in operation today. On the other hand in experiments, while one can release the tracers in a controlled manner and track them forwards in time, it is very difficult to control the final separations of tracers. Also experiments do not provide the degree of details available from simulations (Yeung & Pope 1989). While some progress has been made in backward tracking of fluid particles in experiments (Berg *et al.* 2006; Jucha *et al.* 2014), the scope these studies is still limited. Consequently, new strategies and algorithms are needed to make backward tracking more viable. One of the objectives of the work reported in this thesis is to develop new algorithms to generate and use a large numerical simulation database, enabling the study of backward dispersion of fluid particles across a wide range of Reynolds numbers.

A central idea in study of turbulent dispersion, is applicability of Kolmogorov's hypotheses to Lagrangian statistics. In general the K41 theory can be applied to statistics of single particles and pairs (and as we will see later clusters of three and four particles also). While the application of K41 has been very well studied for forward Lagrangian statistics (see reviews by Sawford 2001; Yeung 2002; Salazar & Collins 2009; Toschi & Bodenschatz 2009), very limited studies have been reported in literature for backward statistics (Sawford *et al.* 2005; Berg *et al.* 2006; Eyink 2011). For single particle statistics, under the assumption of stationarity, the backward results are equivalent to the forward results and hence require no extra effort (Sawford *et al.* 2005). However, for statistics of particle pairs, backward dispersion is fundamentally different from forward dispersion due to irreversibility of Navier-Stokes equations. Arguably the most pivotal result for particle pairs is the Richardson's t^3 law (Richardson 1926; Obukhov 1941) given as

$$\langle r^2 \rangle = g \langle \epsilon \rangle t^3 \quad , \tag{1.1}$$

where $r(t)$ is the separation between a pair of fluid particles, $\langle \epsilon \rangle$ is the mean dissipation rate and t is the time. The constant g is known as Richardson's constant. Under K41, g is expected to be universal and independent of large scales at sufficiently high Reynolds number. Historically, observing Richardson scaling for forward particle pair dispersion has been a subject of much difficulty, as it requires a very wide range of scales, i.e., a very large Reynolds number, which is difficult to achieve in controlled experiments or numerical simulations (Sawford 2001). Nevertheless, significant progress has been made in understanding Richardson's scaling for forward statistics over the past decade (Sawford *et al.* 2008). However, Richardson scaling for backward pair statistics is still not well understood. Earlier studies of backward tracking (Sawford *et al.* 2005; Berg *et al.* 2006) have indicated that backward dispersion is similar to forward dispersion at both very short and very long time scales but stronger at intermediate times of travel (suggesting a larger backward Richardson constant provided the t^3 scaling still holds). But these studies were at relatively small Reynolds number to observe Richardson scaling. More recent studies at moderate Reynolds number (Eyink 2011; Benveniste & Drivas 2014; Bragg *et al.* 2016) have been able to identify some characteristics of Richardson scaling for backward statistics, but are still inconclusive. However, it is clear that access to data over a substantial range of Reynolds number is essential to identify any asymptotic behavior towards Richardson scaling for backward statistics. Hence another objective of the current work is to investigate more rigorously the applicability of Richardson's scaling to backward statistics of particle pairs and in the process also understand how and why backward dispersion is different from its forward counterpart.

Although the motion of fluid particles captures the physics of turbulent dispersion and mixing well, in reality most transported substances undergo Brownian motion relative to the fluid at a rate set by their molecular diffusivity, κ (Saffman 1960). In such a scenario, it becomes important to consider trajectories of 'molecules' which move under the combined action of turbulent velocity field and molecular diffusion. The relative importance of molecular diffusion with respect to turbulent transport can be quantified by the non- dimensional parameter Schmidt number $Sc = \nu/\kappa$. The value of Sc varies widely in practical applications, from $\mathcal{O}(10^{-2})$ in liquid metals, to $\mathcal{O}(1)$ in gas-phase mixing and combustion to $\mathcal{O}(10^3)$ for organic dyes. For the limit $Sc \to \infty$, one can recover the fluid particle behavior. For high

Reynolds numbers and/or weakly diffusive substances ($Sc \gg 1$), the turbulent transport as captured by fluid particles is thought to be the dominant process and serves as a good approximation. However, in situations where the Reynolds number and/or Schmidt number are small, or in vicinity of localized sources, the effects of molecular diffusion as modified by turbulence must be considered explicitly (Sawford & Hunt 1986; Borgas & Sawford 1996). Ultimately, it is the study of backward molecular trajectories that is directly connected to understanding turbulent mixing from a Lagrangian perspective (see review by Sawford & Pinton 2013).

While the connection between turbulent mixing and backward molecular trajectories has been known since the works of Batchelor (1952*a*) and Corrsin (1952), studies related to backward tracking (and even forward tracking for that matter) of molecular trajectories are even rarer in literature because of additional difficulties associated with wide range of Schmidt numbers in practical applications. Saffman (1960) applied the kinematic analysis to provide some theoretical results for small and large time limits of forward molecular statistics. Yeung & Borgas (1997) reported the first numerical results for single molecule statistics and later Borgas *et al.* (2004) provided some theoretical analysis for high Schmidt numbers. Theoretical and numerical results for backward trajectories of molecular pairs were first reported by Eyink (2011) and Benveniste & Drivas (2014) for the case of $Sc \lesssim 1$, focusing on identifying Richardson's scaling at intermediate times. However, these studies were very limited in scope and so far, to the best of our knowledge, there has not been any comprehensive study dealing with both forward and backward molecular statistics for the general case of any Schmidt number. Hence in this work, we also aim at understanding in details, the properties of the trajectories of molecules in both forward and backward reference frames, across a wide range of Reynolds numbers spanning both low and high Schmidt number regimes. The study of molecular trajectories is then extended to study the process of scalar mixing from a Lagrangian perspective.

Turbulent dispersion is often characterized in terms of the relative motion of pairs of fluid particles (or molecules) moving apart from one another (see, e,g. Sawford 2001; Salazar & Collins 2009). More general questions arise if we consider clusters of three and four particles (or triangles and tetrads respectively), whose size and shape are dependent on local stretching and deformation by turbulence at the small scales. In general, the backward statistics of an n-particle cluster are directly related to n^{th} order moments of a passive concentration field (Thomson 1990). Consequently, study of backward tracking of multi-particle clusters (of both fluid particles and molecules) provides the most general overview of turbulent mixing. Although results on the forward tracking of multi-particle clusters have been reported by several groups (Chertkov *et al.* 1999; Pumir *et al.* 2000; Biferale *et al.* 2005; Luthi *et al.* 2007; Xu *et al.* 2008; Hackl *et al.* 2011), backward statistics of four-particle clusters (tetrads) were only recently reported by Jucha *et al.* (2014), identifying differences between forward and backward results at small times. While the Reynolds number in their work was sufficiently high, the observation times were too short to observe any inertial range characteristics. The study of multi-particle clusters (in both forward and backward frames of reference) is also important from the perspective of stochastic modeling (Sawford & Pinton 2013). For example a Lagrangian model of high-order multi-point scalar correlations was presented by Frisch *et al.* (1999), whereas Chertkov *et al.* (1999) developed a Lagrangian model for velocity gradient tensor using the statistics of four-particle clusters (tetrads). While statistics of two particles are a convenient measure of linear dimensions of a cloud of material, statistics of more than two particles provide information about both size and shape of clouds of material. Application of universal scaling to statistics of size and shape of multi-particle clusters is fundamentally important for developing stochastic models. In earlier works of Luthi *et al.* (2007); Xu *et al.* (2008); Hackl *et al.* (2011), it has been established that forward statistics of triangles and tetrads do indeed exhibit inertial range similarity scaling. The statistics of shape in general are known to exhibit more robust scaling behavior than the statistics of size. In the current research, we make similar studies for backward statistics of multi-particle clusters as well.

In this work, we study turbulent dispersion and mixing using Direct Numerical Simulations (DNS), where the exact conservation equations are solved numerically by resolving all relevant length and time scales. Because of the need to resolve a wide range of scales, DNS is inherently computationally intensive (Moin & Mahesh 1998) and a major challenge for high performance computing (Yokokawa *et al.* 2002). In most practical applications, the transport and mixing processes, such as dispersion of pollutants in the atmosphere or mixing of temperature and salinity fields in oceans, involve complex turbulent flows at high Reynolds numbers, with a very wide range of length and time scales. They are typically influenced by turbulence interacting with various other phenomena such as chemistry, buoyancy, radiation, effects of terrains, Earth's rotation and other atmospheric or ocean dynamics (Iribarne & Cho 1980; Pickard & Emery 1990). While the computational power has been growing exponentially over the past few decades, such flow regimes are still beyond the realm of current DNS capabilities. However, if the Reynolds number is sufficiently high, the small scale and inertial range characteristics, are universal in such otherwise complex flows (K41 hypotheses). Also a major focus of the current work is to investigate the fundamental physics associated with dispersion and mixing phenomena, identifying the universal characteristics in all flows. As a result, in the current work, we study forced isotropic turbulence, which is ideal for enabling highest Reynolds numbers possible in DNS. It also allows us to investigate the fundamental physics in the universal equilibrium range (small scales and inertial range), which forms the basis (by providing closure data) for most stochastic models, which in turn are more readily used in practical applications.

The Lagrangian data can be obtained from DNS by tracking a large population of particles, with a degree of detail far surpassing that of experiments (Riley & Patterson 1974; Yeung & Pope 1989). In this work, we consider two scenarios to study dispersion and mixing phenomena. First, particles moving purely under the advective action of turbulence, i.e., fluid particles are considered, since they effectively capture the physics of turbulent transport. Second, particles moving under the combined action of turbulence and molecular diffusion, i.e., Brownian particles or molecules are considered, to additionally capture the physics of scalar mixing. In many practical applications such as cloud physics, multiphase combustion, etc., the effect of particle mass (or inertia) is also important (Shaw 2003; Balachandar & Eaton 2010). However in this work, we focus on fluid and Brownian particles only, which are adequate to describe most dispersion and mixing phenomena (Sawford & Pinton 2013).

While on one hand, achieving high Reynolds number is inherently costly in DNS, it also is a fundamental requirement to study inertial subrange characteristics such as Richardson scaling. In order to enable study of turbulence at high Reynolds numbers, one has to increase both the number of grid points and number of particles, which inevitably requires larger number of processors. We have had the privilege of having access to some of the largest supercomputers with theoretical peaks well exceeding 1 Petaflop (10^{15} floating point operations) per second. In particular, our access to the Blue Waters supercomputer at the National Center for Supercomputing Applications (NCSA) has enabled us to run one of the largest turbulence simulation with 8192^3 grid points and 300 million particles using 262144 processors (which is currently underway). Needless to say, at such a large scale, use of an efficient massively parallel algorithm is of utmost importance.

In DNS, Navier-Stokes equations are solved to obtain flow velocity at fixed grid points in the Eulerian reference frame, subject to appropriate initial and boundary conditions. Simultaneously, a large number of fluid particles are tracked in time to obtain the Lagrangian information. Since the velocity field is available at only fixed grid locations from the Eulerian part, to obtain the velocity at the particle positions, some sort of interpolation is necessary. As a result, in designing a suitable algorithm we need to consider challenges that are specific to the Eulerian and Lagrangian parts of the simulation, both individually and jointly. We use a distributed memory approach where both the Eulerian solution domain and the Lagrangian fluid particles are divided among multiple processors, such that each processor executes the same code on data in its own memory, a programming protocol commonly referred to as Single Program Multiple Data (SPMD). The processors exchange data and synchronize if needed, using a communication protocol such as the Message Passing Interface (MPI). On top of MPI, we employ Coarray Fortran (CAF), a partitioned global address space (PGAS) programming extension of Fortran, which often allows us to exploit the so-called locality of reference (Coarfa *et al.* 2005), which as discussed later, is particularly beneficial for particle tracking in DNS.

To further improve the efficiency and scalability of the code, we also use a shared memory protocol to distribute the work on each processor. In the last decade, while single processor clock rates have reached their limit due to energy considerations, computing power has been increasing exponentially in accordance with Moore's law (Moore 1965). This has been largely possible due to the emergence of multi-core and many-core architectures, the underlying idea of which is to connect a group of identical processors to a main shared memory. All supercomputers today use symmetric multi-processors (SMPs) with the NUMA (non-uniform memory access) architecture which typically constitutes a node (and is the building block of the supercomputer). To fully exploit such systems, we use a hybrid programming approach, which uses MPI or CAF to communicate across nodes, but uses OpenMP threads to share the memory within a node. Some supercomputers additionally have the so called accelerators on each node, such as Intel Many Integrated Core (MIC) architecture on Stampede at Texas Advanced Computing Center (TACC) or NVIDIA graphics processing units (GPUs) on Titan at Oak Ridge National Laboratory. In this work, we also explore the use of such accelerators to improve the performance of both the DNS code and the postprocessing of particle trajectories as obtained from DNS simulations (which as explained later, can become very computational intensive).

In summary, the study of dispersion of fluid particles and molecules, in a Lagrangian frame of reference, is crucial for our physical understanding of turbulent dispersion and mixing. In particular, the backward in time dispersion of pairs and clusters of particles and molecules is rather poorly understood. To this end we use state of the art computing resources to facilitate turbulence simulations at large Reynolds numbers. Hence, the current work has a strong computing aspect to it, which involves both optimizing current algorithms and developing new ones to keep up with the rapidly evolving nature of high performance computing in turbulence research. In the long term, this work will help in improving our understanding of turbulent dispersion and mixing, especially in major transport problems in environmental science. The new insights and detailed data obtained from the current work, will help in development of models of dispersion and mixing at a significantly higher level of physical realism than that available today. These improved models are applicable not only to atmospheric air-quality but also to accidental or terrorism-driven discharge of toxic material and mixing of scalar in practical engineering flows. (In most of these issues, the underlying paradigm is tracking backwards in time or space.)

1.2 Objectives and Outline

The general goals of the current work are as follows:

1. To develop efficient and scalable computational capabilities to perform large scale turbulence simulations. The computational aspect involves optimizing the current Eulerian part and also implementing new parallel algorithm for the Lagrangian part. A novel postprocessing approach has also been developed to obtain backward dispersion statistics at a wide range of Reynolds numbers.

2. To study turbulent dispersion especially from a backward tracking perspective for a wide range of Reynolds numbers. More precisely, to understand and quantify the differences between forward and backward tracking, specially at intermediate times (inertial range), where universal similarity holds.

3. To extend the knowledge for fluid particles to understand molecular dispersion in turbulence over a wide range of Schmidt numbers. This will help reconcile Eulerian and Lagrangian description of scalar mixing and provide further insights, more readily available from the Lagrangian viewpoint.

4. Further extend the work to the study of backward tracking of three and four-particle clusters (triangles and triads).

The rest of this thesis is organized as follows:

Chapter 2 gives an overview of governing equations, the numerical method and the details of parallel implementation with particular focus on the Eulerian part of the code.

Chapter 3 focuses on the computational details of particle tracking and how backward dispersion statistics are obtained via post-processing. We also discuss the scaling problems associated with current implementation and develop an alternate parallel implementation for particle tracking. The challenges associated with post-processing are also addressed along with strategies used to overcome them. Both the new approaches, i.e, for particle tracking and postprocessing, are found to scale very well to large Petascale problem sizes.

In Chapter 4, we present results for the backward dispersion of fluid particle pairs. The differences between forward and backward statistics are investigated with special emphasis on the inertial range characteristics and Richardson scaling. In general, backward dispersion is stronger than forward, especially at intermediate times, resulting in a larger backward Richardson constant. However, the forward results show a more robust Richardson scaling.

In Chapter 5, the work on fluid particles is extended to molecular trajectories. We analyze the forward and backward statistics of molecular trajectories taken singly and in pairs, over a wide range of Schmidt numbers. Statistics of molecular pairs are found to exhibit more robust inertial range scaling than that of fluid particle pairs. The statistics of molecular trajectories are then used to study turbulent mixing from a Lagrangian perspective, making comparisons with Eulerian results for Schmidt numbers of order unity. The well know scalar dissipation anomaly is also addressed in a Lagrangian context.

In Chapter 6, we analyze the backward statistics of triangles and tetrads. Some results on statistics of both size and shape of tetrads are reported. Both the forward and backward statistics of tetrad shape show more robust scaling than the statistics of tetrad size.

A summary of the current work is provided in Chapter 7. The scope of future work, such as possible extensions to study of clusters of molecules, backward tracking of inertial particles, etc. is also given.

Some derivations relevant to the material presented in Chapter 5 are given in the appendices.

CHAPTER II

GOVERNING EQUATIONS AND DIRECT NUMERICAL SIMULATIONS

In this chapter we describe the governing equations and the computational methodology used to perform the direct numerical simulations (DNS) on massively parallel supercomputers, focusing on the Eulerian part (the Lagrangian part and the corresponding challenges and improvements associated with it are discussed in the next Chapter). The Navier-Stokes equations are solved numerically using a pseudo-spectral method in space (Rogallo 1981) and second-order Runge-Kutta integration in time. In addition to study turbulent mixing, we consider a passive scalar driven by a uniform mean-gradient.

2.1 Velocity field

Assuming constant density and no mean velocity, the Navier-Stokes equations for the fluctuating velocity field $\mathbf{u}(\mathbf{x},t)$ can be written in the Cartesian tensor notation as

$$\begin{aligned} \frac{\partial u_i}{\partial t} + u_j \frac{\partial u_i}{\partial x_j} &= -\frac{1}{\rho}\frac{\partial p}{\partial x_i} + \nu \frac{\partial^2 u_i}{\partial x_j \partial x_j} \ , && (2.1) \\ \frac{\partial u_i}{\partial x_i} &= 0 \ , && (2.2) \end{aligned}$$

where, p is the fluctuating pressure, ρ is the density (assumed constant) and repeated indices imply summation as per tensor notation. The boundary conditions used are periodic and given as,

$$u_i(\mathbf{x} + nL_o\mathbf{e}_j, t) = u_i(\mathbf{x}, t) \qquad n = 1, 2, 3, \dots \ , \tag{2.3}$$

where L_0 is the domain length in each direction and $\mathbf{e}_j$ is a unit vector in the j^{th} direction. The use of periodic boundary condition enables the representation of the velocity field as a discrete Fourier series,

$$u_i(\mathbf{x}, t) = \sum_{\mathbf{k}} \hat{u}_i(\mathbf{k}, t) e^{\mathrm{i}\mathbf{k}\cdot\mathbf{x}} \ , \tag{2.4}$$

where $\mathbf{k}$ is the wavenumber vector, $\hat{u}_i$ is the Fourier coefficient (or Fourier mode) of u_i and $\mathrm{i} \equiv \sqrt{-1}$. The physical domain, which is a cube of side L_0, is divided into N grid points along each direction, such that their position is defined as as $(l_1\Delta, l_2\Delta, l_3\Delta)$, where l_1, l_2, l_3, are integers going from 0 to $N-1$ and $\Delta = L_0/N$ is the grid spacing in each direction. In wavenumber space there are N^3 discrete wavenumbers, (m_1k_0, m_2k_0, m_3k_0), where m_1, m_2, m_3, are integers going from $1-N/2$ to $N/2$ and $k_0 = 2\pi/L_0$ is the lowest non-zero wavenumber magnitude. Typically we use a domain size of $L_0 = 2\pi$, which results in convenient integer values for wavenumbers. Although in some physical problems where the large scales grow with time, e.g., rotating flows, strained or shear flows, low Schmidt number mixing, larger domain lengths such as 4π or 8π would be appropriate. Since the velocity field in the physical space is real-valued, the Fourier coefficients obey conjugate symmetry, i.e., $\hat{\mathbf{u}}(-\mathbf{k}, t) = \hat{\mathbf{u}}^*(\mathbf{k}, t)$, where the asterisk denotes a complex conjugate. As a result only half the Fourier modes need to be stored in memory. Depending on the requirement, we can use the same array to store either the velocity field in the Fourier space ($N^3/2$ complex values) or the physical space (N^3 real numbers).

The equations give by (2.1) and (2.2) can be transformed to Fourier space as

$$\begin{aligned} \Big(\frac{\partial}{\partial t} + \nu k^2\Big)\hat{u}_i(\mathbf{k}, t) &= -\Big(\delta_{ij} - \frac{k_i k_j}{k^2}\Big)\hat{G}_j(\mathbf{k}, t)\ , \qquad (2.5) \\ k_i\hat{u}_i &= 0\ , \qquad (2.6) \end{aligned}$$

where, δ_{ij} is the Kronecker delta function (equal to 1 for $i = j$ and 0 otherwise), $k = |\mathbf{k}|$ is the magnitude of the wavenumber vector and $\hat{G}_j(\mathbf{k}, t)$ is the Fourier transform of the nonlinear term in (2.1) given by the following convolution sum,

$$\hat{G}_j(\mathbf{k}, t) = \mathrm{i}k_m \sum_{\mathbf{k}'} \hat{u}_j(\mathbf{k}', t)\hat{u}_m(\mathbf{k} - \mathbf{k}', t)\ . \qquad (2.7)$$

While the left-hand side of (2.5) involves $\hat{u_i}$ at only $\mathbf{k}$, the right-hand side involves $\hat{u_i}$ at $\mathbf{k}'$ and $\mathbf{k}''$, such that $\mathbf{k}' + \mathbf{k}'' = \mathbf{k}$. Thus in wavenumber space, the convection term is non-linear and non-local, involving the interaction of wavenumber triads, $\mathbf{k}$, $\mathbf{k}'$ and $\mathbf{k}''$, which form a closed triangle. Thus the partial differential equations given by (2.1) and (2.2) are transformed into a set of ordinary differential equations, which can now be integrated numerically to obtain the velocity field at different times. The computation of the $\hat{\mathbf{G}}(\mathbf{k},t)$ and time integration are the main aspects of the numerical algorithm.

A direct calculation of $\hat{\mathbf{G}}(\mathbf{k},t)$ is prohibitively expensive as it involves calculating the convolution sum which requires N^6 operations. Instead a pseudo-spectral approach (Rogallo 1981) is used, such that the velocity field is transformed into physical space, where the nonlinear terms are computed and then transformed back to wavenumber space. The non-linear term $\hat{G}_j(\mathbf{k},t)$ in (2.5) is computed as

$$\hat{G}_j(\mathbf{k},t) = -\mathrm{i}k_m \, \mathcal{F}_k\{u_j(\mathbf{x},t)u_m(\mathbf{x},t)\} \, , \tag{2.8}$$

where, $\mathcal{F}_k\{\cdot\}$ denotes a Fourier transform from physical to wavenumber space. Essentially, the pseudo-spectral approach requires two sets of transforms, one for velocity from wavenumber to physical space and one for the non-linear terms from physical to wavenumber space. These transforms are computed using the Fast Fourier Transfer (FFT) algorithm (Cooley & Tukey 1965) and requires order $N^3 \log_2 N$ operations. However, the pseudo-spectral treatment of non-linear terms also results in aliasing errors, which are controlled by a combination of phase shifts and truncation (Rogallo 1981). As a result of truncation, the magnitude of highest resolvable wavenumber is lowered to $k_{max} = \sqrt{2}Nk_0/3$ (Canuto *et al.* 1987).

The time integration is performed using an explicit second-order Runge-Kutta method. If the right-hand side of (2.5) is denoted by $\hat{c}_i$, then at time step t_n, we can write

$$\frac{d(F\hat{u}_i(\mathbf{k},t_n))}{dt} = F\hat{c}_i(\mathbf{k},t_n) \, , \tag{2.9}$$

where, $F(t) = \exp\left(\int_{t_n}^{t} \nu k^2 dt\right)$ is the integrating factor with $F(t_n) = 1$. To advance from time t_n to $t_{n+1} = t_n + \Delta t$ (where Δt is the time step), we first calculate the predictor step estimate as

$$F(t_{n+1})\hat{u}_i^p = \hat{u}_i(\mathbf{k},t_n) + \hat{c}_i(\mathbf{k},t_n)\Delta t \tag{2.10}$$

and then the corrector step result as

$$F(t_{n+1})\hat{u}_i(\mathbf{k},t_{n+1}) = \hat{u}_i(\mathbf{k},t_n) + \frac{\Delta t}{2}[\hat{c}_i(\mathbf{k},t) + F(t_{n+1})\hat{c}_i^p] \, , \tag{2.11}$$

where $\hat{c}_i^p$ is the convective term computed using $\hat{u}_i^p$ (velocity at the predictor step). The value of Δt is calculated using the Courant-Friedrichs-Lewy (CFL) condition

$$\Delta t = C \; \frac{\Delta}{(|u_1| + |u_2| + |u_3|)_{max}} \; , \tag{2.12}$$

where, C is the CFL number and (u_1, u_2, u_3) are the Cartesian components of velocity at a grid point and the maxima is taken over the entire domain. While for finite-difference schemes, numerical stability considerations typically require $C \leq 1$, for spectral methods stability analysis is not so well established (Peyret & Taylor 1983). However, it is common to follow the same condition (Eswaran & Pope 1988). Typically the value of C is about 0.6 in our simulations.

Due to the spectral nature of the numerical scheme, it is very common to measure the grid resolution using the non-dimensional parameter, $k_{max}\eta$, where $\eta = \left(\nu^3/\langle\epsilon\rangle\;\right)^{1/4}$ is the Kolmogorov length scale (a measure of the smallest length scales in the flow field). Using the definition of k_{max}, one can write

$$(k_{max}\eta)\frac{\Delta}{\eta} = \frac{2\sqrt{2}\pi}{3} \; . \tag{2.13}$$

Typically in DNS simulations, $k_{max}\eta$ between 1.0 and 2.0 is used (Yeung & Pope 1989; Kaneda *et al.* 2003; Ishihara *et al.* 2009), with $k_{max}\eta \approx 1.4$ being the most common which corresponds to $\Delta/\eta \sim 2$. At the same time, the domain size must be several times larger than the largest length scales (usually measured in terms of the longitudinal integral length scale L_1). The ratio L_0/L_1 is about 5–6 in our simulations, which is enough to ensure that the flow field is not strongly influenced by domain size.

To maintain a statistically stationary state, the large scales in the range $k_0 \leq k \leq k_F$ are forced using a combination of six independent Uhlenbeck-Ornstein random processes (Eswaran & Pope 1988), where k_F is typically chosen to be around 2. The underlying assumption is that the small scales are independent of the large scales. This is increasingly valid as the Reynolds number increases (and hence the range of scales increases), as suggested by the K41 hypotheses and is well supported by data in the literature (Sreenivasan 1998). The resulting velocity fields are statistically stationary to a good approximation. Recently, Donzis & Yeung (2010) have developed a new forcing scheme which freezes the energy in the range $k_0 \leq k \leq k_F$, at values suggested by long-time averages derived from previous simulations which used the stochastic forcing of Eswaran & Pope (1988). This further allows us to minimize the temporal oscillations of the kinetic energy and dissipation rate, leading to improved stationary characteristics. The length of each simulation is typically extended to several large eddy turnover times $T_E \sim L/u'$ (where u' is the r.m.s of the velocity fluctuations), since long-time averages are consistent with ensemble averages of the original K41 theory due to ergodicity (Frisch 1995; Galanti & Tsinober 2004).

Using the grid resolution (given by N^3) and the number of time steps (given by $T_E/\Delta t$), one can estimate the total cost a simulation. By classical scaling estimates the number of grid points required to resolve all scales varies as $N^3 \sim (L/\eta)^3 \sim R_\lambda^{9/2}$, where R_λ is the Taylor-scale Reynolds number. If as a first order approximation, the denominator in the right-hand side of (2.12) is assumed to be proportional to u', then a fixed CFL number would imply $T_E/\Delta t \sim L/\Delta \sim L/\eta$ (since $\Delta \sim \eta$). Hence the number of time steps scales as $R_\lambda^{3/2}$, giving the total cost proportional to R_λ^6. This rapid increase in computational resources with increasing Reynolds number makes DNS very challenging.

2.2 Passive scalars

In addition to the Navier-Stokes equations, we also solve for the scalar fluctuations $\phi(\mathbf{x},t)$, driven by an uniform mean gradient $\nabla\Phi$ (Yeung 1996; Overholt & Pope 1996), governed by the equation

$$\frac{\partial\phi}{\partial t} + u_i\frac{\partial\phi}{\partial x_i} = -u_i\frac{\partial\Phi}{\partial x_i} + \kappa\frac{\partial^2\phi}{\partial x_i\partial x_i}\ , \tag{2.14}$$

The mean scalar gradient acts as a source term and hence no forcing is necessary. To ensure homogeneity, the mean gradient must be constant. For an isotropic velocity field, the orientation of the gradient vector does not affect the statistics of the scalar field and it is sufficient to align with any of the coordinate axes. Hence, we can choose $\nabla\Phi = (G, 0, 0)$ where G is a constant and represents the mean gradient magnitude. However, to ensure better sampling for each scalar, we ensemble over three different realizations, each with a mean-gradient aligned separately with the three coordinate axes. Periodic boundary conditions are also used for the scalar field, whereas the initial scalar field is set to zero everywhere:

$$\begin{aligned} \phi(\mathbf{x}+nL_o\mathbf{e}_k,t) &= \phi(\mathbf{x},t) \qquad n=1,2,3,\dots\ , && (2.15)\\ \phi(\mathbf{x},0) &= 0\ . && (2.16) \end{aligned}$$

This allows the scalar field to be also represented by a discrete Fourier series. As a result, (2.14) can be transformed to the wavenumber space resulting in

$$\Big(\frac{\partial}{\partial t}+\kappa k^2\Big)\hat{\phi}(\mathbf{k},t) = -\mathrm{i}k_i\ \mathcal{F}_k\{u_i(\mathbf{x},t)\phi(\mathbf{x},t)\} - G\hat{u}_1(\mathbf{k},t)\ . \qquad (2.17)$$

For passive scalars, we can again treat the non-linear term using Rogallo's (1981) pseudo-spectral approach. Essentially the number of variables to solve now becomes $3+N_c$, where N_c is the number of scalars.

The simulation parameters, such as grid resolution (Δ), time step (Δt), domain size (L_0), typically depends on the choice of Schmidt number. While for $Sc \lesssim 1$ no special considerations are required, for $Sc \gg 1$ the smallest length scale in the scalar field is smaller than Kolmogorov length scale, hence requiring finer grid resolution, which also leads to a smaller time step from the CFL condition (Donzis & Yeung 2010). On the other hand, for $Sc \ll 1$, while the smallest scale is larger than Kolmogorov length scale, the largest scales in scalar field are larger than in velocity field. This requires a larger domain, while maintaining the small scale resolution. Also the fast molecular diffusion results in very small time scales ($\Delta t \sim \Delta^2/\kappa$), resulting in a much stricter CFL criterion (Yeung & Sreenivasan 2013, 2014). Due to these constraints, Eulerian simulations of high and low Schmidt numbers are inherently expensive. However, as we explain later, these constraints are absent in the Lagrangian framework. Consequently, we investigate the high and low Schmidt number regimes using the Lagrangian perspective, and restrict our Eulerian simulations to $Sc \lesssim 1$, which is enough to validate the Lagrangian results when necessary.

2.3 Parallel implementation

It is evident from previous sections that DNS of high Reynolds number turbulence requires the use of most powerful supercomputers available to the research community [1]. We have

---

[1] *www.top500.org*

access to the computing resources at many national supercomputing centers, some of which are Blue Waters at the National Center for Supercomputing Applications (NCSA), Stampede at Texas Advanced Computing Center (TACC), Titan at Oak Ridge National Laboratory (ORNL), Edison at National Energy Research Scientific Computing Center (NERSC), Kraken (now decommissioned) at National Institute of Computational Sciences (NICS). Each of these supercomputers have a theoretical peak performance in the Petaflop range. A summary of the supercomputers used in this work, along with their system specifications is given in table 2.1.

To best utilize the supercomputing resources, we use a massively parallel implementation of Rogallo's (1981) pseudo-spectral algorithm, in which the most time-consuming task is the computation of the 3D FFT. The solution domain is divided among P processors (also commonly referred to as MPI tasks) using a two-dimensional (2D) domain decomposition (Donzis *et al.* 2008), such that pencils of size $N \times (N/P_{row}) \times (N/P_{col})$ are available to each MPI task, where P_{row} and P_{col} stands for the number of MPI tasks along the rows and columns such that $P_{row} \times P_{col} = P$. A schematic of the mapping is shown in figure 2.1.

To perform the 3D FFT, we use a transpose-based approach (described in Pekurovsky 2012), as opposed to a distributed FFT (Dubey & Tessera 2001). Distributed FFT relies on a parallel implementation of the 1D-FFT with each MPI task communicating the necessary data with the other tasks. On the other hand, transpose-based FFT relies on a sequential version of 1D-FFT that performs the transform on one dimension at a time, transposing the data when needed and is considered to be faster than the distributed FFT approach (Foster & Worley 1997; Dubey & Tessera 2001). Since a given task holds complete lines of data only along a single direction, two global data transposes are required to perform the 3D FFT. If we start with the pencils aligned in say the x-direction, the first step is to take the 1D FFT along x-direction, which is a local task on each task. Then a global transpose is carried out to align the pencils in say the z-direction, followed by a 1D FFT along the z-axis. Finally, the data is again globally transposed to align the pencils in y-direction, followed by the last 1D FFT. A schematic of this procedure is show in figure 2.2. These global transposes are typically accomplished by using the `MPI_ALLTOALL` intrinsic, one in each of the two orthogonal sub-communicators formed from P_{row} and P_{col} MPI tasks respectively. For example, in figure 2.1, tasks $P0$, $P4$, $P8$ and $P12$ belong to the row sub-communicator, whereas $P0$, $P1$, $P2$ and $P3$ belong to the column sub-communicator. Such a strategy enables the communication process to be confined in smaller local sub-communicators instead of the entire `MPI_COMM_WORLD` (the communicator for all P tasks). Furthermore, the data required to be sent to other MPI tasks is typically non-contiguous in memory. As a result, the ALLTOALL exchange is usually preceded and followed by some sort of 'packing' and 'unpacking' respectively. This ensures that the data for the local 1D FFT within each pencil is of unit stride.

The local 1D FFT is performed by each MPI task using the FFTW library (Frigo & Johnson 2005). For N data points, the complexity of the 1D FFT is order $N \log_2 N$ and hence for the entire grid the total cost is order $N^3 \log_2 N$. The use of FFTW library and providing data with unit stride, results in highly optimized FFT calculations on each MPI task and scales near perfectly with both problem size and the number of MPI tasks. As a result, the main bottleneck is the communication required to perform the ALLTOALLs, which is known to degrade with increasing problem size and number of MPI tasks (Kumar *et al.* 2008; Pekurovsky 2012) and thus is a major challenge at Petascale level. Typically the performance of ALLTOALLs is influence by a number of factors. For an ALLTOALL in a communicator, each MPI task needs to send a block of data to every other task. As a result, the total number of messages increase quadratically with the number of tasks in the communicator, which can result in serious network congestion at large problem sizes (Chan *et al.* 2008). The performance also depends on other factors like the type of the interconnect used in the parallel system (hence network latency and bisection bandwidth), how the MPI tasks are mapped to the physical node (topology of the processors), and interference from other jobs running on the system. We address these issues one by one.

One strategy employed to reduce the network congestion is to choose P_{row} such that all the MPI tasks in the row communicator lie on a physical node. This results in the first transpose being performed entirely on the node without using the network. Essentially, the

2D pencil decomposition is reduced to a pseudo 1D "slab-on-node" decomposition, while off-node communication for one of the transposes is eliminated. The contention and overhead from `MPI_ALLTOALL` can be further reduced by instead using a partitioned global address space (PGAS) programming model such as Coarray Fortran (CAF) on Cray machines such as Blue Waters at NCSA (Fiedler *et al.* 2013). Compared to MPI, communication calls in CAF can have smaller headers (due to one-sidedness) and therefore can carry more data per packet for slightly higher bandwidth. In addition, latencies for short messages in CAF, can be significantly lower than in MPI (Fiedler *et al.* 2013). For these reasons, the use of CAF is beneficial even in particle tracking (as discussed in the next chapter). The network congestion and interference from other jobs, can be further reduced by using a topology aware scheduler to place jobs on topologically adjacent nodes on the network (Enos *et al.* 2014). These considerations, implemented with the help of consultants at NCSA, has greatly helped in improving the performance on large Cray machines (which typically use the Gemini network in a 3D torus configuration).

More advanced strategies based on the truncation used to control the aliasing errors have also been used in past. Since the numerical scheme results in all Fourier modes above k_{max} being truncated, the message size for the ALLTOALLs can be reduced by not communicating these modes and just trivially setting them to be zero (Pekurovsky 2012). This strategy is particularly useful on non-Cray machines where ALLTOALLs are not so sensitive to the network (such as Stampede at TACC, which uses a fat-tree network). The code is also designed to use OpenMP to reduce the number of MPI tasks while maintaining the same core count, which can help alleviate both memory and network latency issues (Tsuji & Sato 2009).

Another consideration is the use of accelerators in what is commonly referred to as heterogeneous computing. Along with the central processing units (CPUs), the nodes on many modern supercomputers are equipped with accelerators, e.g. Intel MIC on Stampede, GPUs on Titan. As of now, the top two supercomputers on the *www.top500.org* list use accelerators/heterogeneous computing. The underlying idea behind using accelerators is to supplement a few CPUs which are highly optimized for sequential processing, with hundreds to thousands of much smaller and efficient cores, designed for handling parallel workloads. The accelerators greatly outpace the CPUs in arithmetic throughput and memory bandwidth providing excellent speedups at a very reasonable power cost. For the 3D FFTs, we can offload the 1D FFTs and the packing/unpacking portions of the code to the accelerators, whereas the communication still happens through the CPUs. We have already implemented this on Titan using the OpenACC standard for GPU programming and the speed up obtained from the GPUs has reduced computational cost to the point where it is almost negligible. However, the communication cost from the ALLTOALLs remains unchanged. Since at Petascale and bigger problem sizes, the 3D FFTs are almost entirely dominated by communication, the use of GPUs (or accelerators in general) is not very beneficial to overall performance (Czechowski *et al.* 2012). Nevertheless, we still have managed to port our codes to run on these heterogeneous machines.

To summarize, we use a 2D processor grid which decomposes the N^3 grid points into pencils of data. Then a transpose based algorithm is used to perform the 3D FFT, in which communication is the main bottleneck. A number of strategies are employed with active help from consultants at supercomputing centers to improve the efficiency and scaling of communication costs. The most notable is the use of CAF on Blue Waters, which greatly improves the communication performance and allows the code to scale well up to $\mathcal{O}(10^5 - 10^6)$ processors. In general, considerable effort has been spent in optimizing the transposes to the point that the Eulerian code now performs very efficiently. Hence, in the current work our main focus is the particle tracking aspect of the DNS (as discussed in next chapter).

Table 2.1: List of Petascale supercomputers used in current work

Supercomputer	Blue Waters	Stampede	Titan	Edison	Kraken[1]
Location	NCSA	TACC	ORNL	NERSC	NICS
System type	Cray XE6/XK7	Intel Xeon-Phi	Cray XK7	Cray XC30	Cray XT5
Nodes	22640/4228	6400	18688	5576	9408
Network	3D Torus	Fat-tree	3D Torus	Dragonfly	3D Torus
Peak Perf.	13.34 PF	9.60 PF	27.11 PF	2.57 PF	1.17 PF

[1] now decommissioned

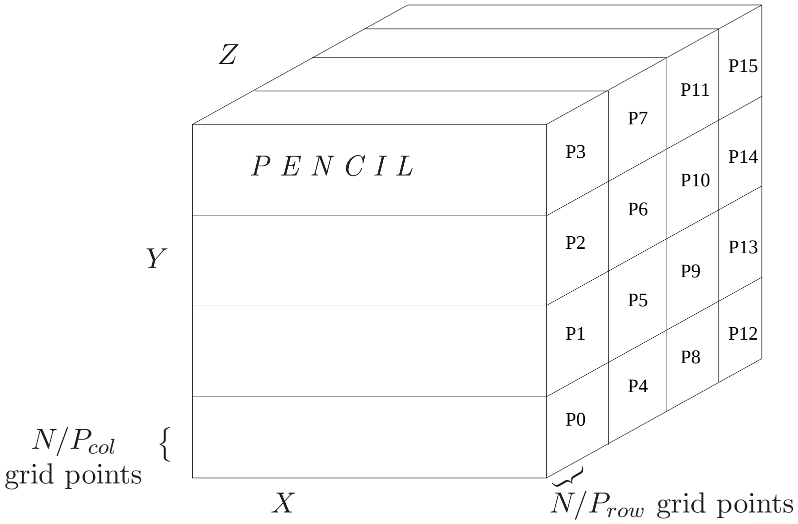

Figure 2.1: Mapping the N^3 domain into a 2D computational grid with $P = P_{row} \times P_{col}$ processors. Here $P_{row} = P_{col} = 4$.

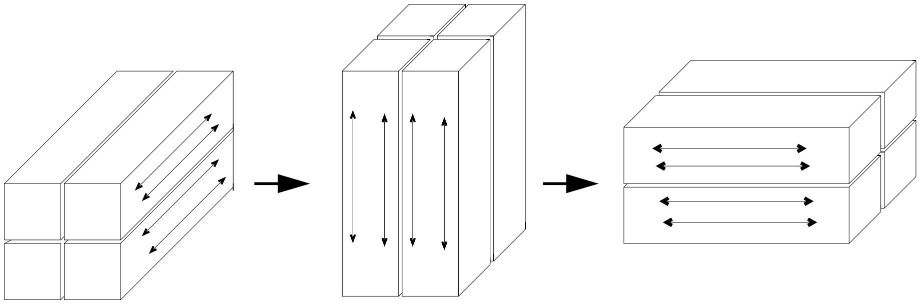

Figure 2.2: 1D FFT in each direction followed by a transpose for a 2D computational grid. Two global transposes are needed to complete a 3D FFT in this case. Here $P_{row} = P_{col} = 2$.

CHAPTER III

PARTICLE TRACKING ALGORITHM AND POSTPROCESSING

3.1 Introduction

As discussed in the previous chapter, in the Eulerian part of the DNS code, we compute the 3D velocity field at N^3 grid points. In the Lagrangian part, a large number of fluid particles are initialized at $t = 0$ and tracked forward in time along with the velocity field. The motion of these fluid particles is governed by a simple ordinary differential equation:

$$\frac{d\mathbf{x}^+(t)}{dt} = \mathbf{u}^+(t) \ , \tag{3.1}$$

where, $\mathbf{x}^+$ and $\mathbf{u}^+$ denote the particle position and velocity respectively, and $\mathbf{u}^+$ is simply the Eulerian velocity taken at the instantaneous particle position

$$\mathbf{u}^+ = \mathbf{u}(\mathbf{x}^+, t) \ . \tag{3.2}$$

Since the Eulerian velocity $\mathbf{u}$ is available only at fixed N^3 grid points and the particle positions in general can be anywhere, to obtain the Lagrangian velocity $\mathbf{u}^+$, we need to interpolate between the grid points. We use cubic-spline interpolation, which is fourth-order accurate and twice- differentiable, making them suitable for interpolating other quantities like velocity gradients or for subsequently obtaining the acceleration by differentiating the interpolated velocity in time (Yeung & Pope 1988). The following formula is used to obtain the particle velocity

$$u^+ = \sum_{k=1}^{4}\sum_{j=1}^{4}\sum_{i=1}^{4} b_i(x^+)c_j(y^+)d_k(z^+)e_{ijk}(\mathbf{x}) \tag{3.3}$$

where b_i, c_j, d_k are the 1-D basis functions that are determined by the particle position co-ordinates ($\mathbf{x}^+ = (x^+, y^+, z^+)$) and e_{ijk} are the 3-D spline coefficients that are computed from the Eulerian velocity field $\mathbf{u}(\mathbf{x})$. The interpolation requires 4 grid points in each direction. Hence a total of 4^3 or 64 points are required for each particle. Also as a result, a total of $(N + 3)^3$ spline coefficients are required for the entire grid. The algebraic details of the method and the expressions for basis functions and spline coefficients are available in Yeung & Pope (1988).

Once the velocity at the particle position is obtained, the position of the particle is simply integrated in time using second-order Runge-Kutta method using the time step as obtained from the Eulerian part of the DNS code. The position after the predictor step is given as

$$\mathbf{x}^* = \mathbf{x}^+(t_n) + \Delta t \; \mathbf{u}(\mathbf{x}^+(t_n), t_n) \; , \tag{3.4}$$

and after the corrector step, we get

$$\mathbf{x}^*(t_{n+1}) = \mathbf{x}^+(t_n) + \frac{\Delta t}{2} \left[\mathbf{u}(\mathbf{x}^*, t_n) + \mathbf{u}(\mathbf{x}^+(t_n), t_n) \right] \; . \tag{3.5}$$

As it can be seen, the time integration of particles is rather simple. Consequently, the most time consuming task in particle tracking is to obtain the particle velocity as interpolated from the 64 neighboring grid points.

3.2 Parallel implementation

Consider a total of N_p particles being tracked. Since N_p is typically very large (many millions), the particle positions and velocities need to be distributed among the MPI tasks. A key consideration in particle tracking is that, as the particles wander around under the action of turbulence, the position of particles and hence the required interpolation stencil of 4^3 points, keeps changing with time. As a result, the efficient parallel implementation of this interpolation for the wandering particles is not straightforward. One approach is to keep each MPI task responsible for the same set of particles which were initiated on that MPI task and receive the required information for interpolation from other tasks. We call this the 'global' approach as it requires a global exchange of information for interpolation. Another approach is to let each particle at a given time step be tracked by the MPI task which holds the sub-domain in which the particle is instantaneously located. This implies that each MPI task is responsible for a dynamically evolving instead of a fixed sub-population of particles. We call this the 'local' approach, as the information for interpolation is almost always available locally on the MPI task. In previous works, we have used the global approach and for small to moderate problem sizes it performs reasonably well. However, for large problem sizes such as 8192^3 on $262,144$ processors, the global approach scales very poorly and hence in this work we develop and implement a local approach. In the following section, we discuss the global approach along with the merits and shortcomings associated with it. Then the local approach is described in detail.

3.2.1 Global approach

In the global approach, the particles are initially (at time $t = 0$) divided equally among all MPI tasks. On every task, each particle is assigned a random initial position (using the Fortran intrinsic `RANDOM_NUMBER` with a different random seed on each task to ensure statistical independence) within the entire domain, i.e., the coordinates in each direction are between 0 and L_0. Now for the entire DNS run, each MPI task is always responsible for the same set of particles, to which it was initially assigned, and the interpolation is carried out using the following operations:

First, the 3D spline coefficients (e_{ijk}) are computed from the Eulerian velocity field. This requires solving a set of tridiagonal system of equations in each direction (Yeung & Pope 1988). The calculation of the spline coefficients shares some similarities to that of 3D FFTs, as it requires the complete data in each direction to compute the individual components in that direction. Since there are $(N+3)^3$ spline coefficients and $N+3$ is not divisible by P (total number of MPI tasks), the ALLTOALL protocol is replaced by ALLTOALLV to perform the transposes. The calculation of spline coefficients in this manner is a direct result of the interpolation scheme being fourth-order accurate. This task is required irrespective of whether the global or local approach is used.

Second, we calculate the 1D basis functions (b_i, c_j, d_k). The basis functions are simple algebraic functions of the particle position (which is already known to the MPI task). However, the summation in (3.3) now requires communication, since, as the particles wander around, the majority of them will require access to spline coefficients held by another MPI task. To do so, the 1D basis functions are gathered into a global array, such that each MPI task now has the information for all particles. This is performed using the `MPI_ALLGATHER` protocol. To avoid any memory issues due to the size of this extra global array, particles can be processed in smaller batches.

Third, the summation is now carried out using the information computed and communicated as described above. Each MPI task now has the information about 1D basis functions for all particles, but only the local spline coefficients. As a result, each MPI task can calculate a partial sum for each particle. These partial sums are finally added up using an `MPI_REDUCE` and the result are returned to their corresponding MPI tasks using an `MPI_SCATTER`. We were also able to implement a CAF version of REDUCE+SCATTER, where a collective reduce was executed using a binary-tree algorithm (Buaria & Yeung 2014) and was found to perform better than the MPI counterpart on Cray machines.

The advantage of the global approach lies in its simple implementation. Since each task has to keep track of its own N_p/P particles, the work distribution is exactly the same on all MPI tasks. However, this approach requires lot of global communication which does not scale efficiently to large number of processors. Table 3.1 shows the timings for the particle tracking part of the code, using the global approach. The cases selected are in accordance with weak scaling arguments for the Eulerian part, but the number of particles is held constant. This also represents the weak scaling for the calculation of spline coefficients, since they also depend on the number of grid points. However for the interpolation portion it represents the strong scaling argument since the number of particles are held constant while the number of processors is increased. As it can be seen, the communication performance (specially for ALLGATHER) greatly deteriorates with increasing number of processors for the same number of particles. We use a hybrid MPI/OpenMP approach to alleviate some of the network latency issues. However, adding more threads leads to increased overhead from OpenMP, which overrides any improvement obtained from reducing the latency. The best timings are typically obtained for when 2 threads are used (as reported in table 3.1).

Table 3.2 shows the same set of timings with four times the particles as shown in table 3.1. The calculation of spline coefficients takes almost the same time as before, since it is independent of the number of particles. The time taken in other operations, especially ALLGATHER, increases with the number of particles (though the factor is less than 4, except for the computation part) and at the largest problem size the performance is extremely poor. Another factor leading to this poor performance is interference from other jobs running on the system. While the ALLTOALLs are also affected by network traffic to some extent, the sheer volume of data being communicated in an ALLGATHER (which rapidly increases with both the number of particles and processors) makes it more susceptible to network traffic and congestion. Thus at the largest problem sizes, a new approach, avoiding such expensive collective communication calls is of utmost importance.

3.2.2 Local approach

In the local approach, the main idea to keep the particles ‘local’ to the MPI tasks, i.e., a scheme whereby at every time step each particle will lie in a sub-domain where all information required for interpolation will be available locally on an MPI task. In such a scenario, the expensive collective communication calls such as ALLGATHER and REDUCE+SCATTER are automatically eliminated. However, we still need to communicate the spline coefficients required for interpolation, for particles very close to domain boundaries. Also if a particle crosses into a different sub-domain kept by a neighboring MPI task, then all of its information is transferred to this new ‘host’ MPI task. Thus we need to explicitly keep track of every particle by assigning an index to it. The underlying concept of the local approach is similar to the spatial decomposition particle tracking done in molecular dynamics (Plimpton 1995; Phillips *et al.* 2005) and was also recently used by Ireland. *et al.* (2013) for fluid and inertial particles in homogeneous turbulence. The main procedures for interpolation can be summarized as follows:

First, we compute the spline coefficients, using the Eulerian velocity field just like the global approach. This operation is unchanged.

Second, the basis functions can also be directly from the particle positions just as before. Next, taking advantage of the fact that the particle is in the same sub-domain, i.e., the required spline coefficients are also on the same MPI task, we can directly proceed to the interpolation. For particles near the boundaries, communication is required to access the required spline coefficients. However, unlike the global approach, this communication occurs only between MPI tasks holding adjacent sub-domains, instead of across the entire global communicator.

Third, since the approach requires that all particles be local, an additional operation is required after the interpolation and time advancement. At every time step, we need to check the new position of every particle and move them to their new MPI tasks if required. However, based on the CFL criterion, the particle cannot move more than one grid spacing at every step. As a result, a particle can only move to an immediately neighboring MPI task. Thus in this operation, a exchange of particles is performed using `MPI_SEND`s and `MPI_RECV`s.

While the advantage of this approach is very evident, i.e., the communication pattern is always localized between neighboring MPI tasks, which can result in excellent scaling properties (discussed later in § 3.2.3), it also has a few drawbacks. Since the number of particles on each MPI task is not the same, in principle this can lead to load imbalance. However, in homogeneous flows, such as the one considered in this work, the spatial distribution of particles is more or less uniform. As a result, on average, the number of particles leaving a MPI task, is of the same order as the number of particles entering. Furthermore, the amount of time spent on interpolation with this new scheme, is such a small fraction of the total time (also discussed in § 3.2.3), that the small degree of imbalance can be ignored. However, in future if this code is to be extend to study of say inertial particles (particles with mass), which are known to cluster inhomogeneously even in homogeneous flows, we will have to consider adding some sort of dynamic load balancing. Another drawback of this approach is in I/O. Since the particles are freely changing the task they belong to, writing out the particle positions and velocities requires additional consideration (discussed in later section).

An important consideration in this approach is the manner in which the communication is performed for the above mentioned second operation, i.e., communication of spline coefficients for particles near the domain boundaries. A common method to exchange such information is to allow each MPI task to hold several layers of 'ghost points' (Pletcher *et al.* 2012). After the spline coefficients are computed, a simple exchange using SENDs and

RECVs can populate these ghost layers and then even for the particles near the boundary, the interpolation becomes local. Recently, Ireland. *et al.* (2013) used such an approach for particle tracking in DNS of homogeneous turbulence of up to 2048^3 grid points. In the current algorithm, since 4 points are required in each direction for the interpolation, a ghost layer extending to 3 extra points in each direction is sufficient. However, using ghost layers has an inherent drawback, especially at large problem sizes. In the 2D domain decomposition, the size of each pencil (in terms of grid points) is $N \times (N/P_{row}) \times (N/P_{col})$ and the typical practice is to keep P_{row} equal to the number of cores in a node to obtain the best ALLTOALL performance for the Eulerian part of the code (and even the ALLTOALLV part of the Lagrangian code, when the spline coefficients are calculated). For example, on Blue Waters, each node has 32 cores and the largest problem size of 8192^3 grid points is typically run on 8192 nodes. Thus for this case, $P_{row} = 32$ and $P_{col} = 8192$, giving pencils of dimensions $8192 \times 256 \times 1$. In such a scenario, using a ghost layer of 3 points in each direction is not feasible, as the ghost layer itself would be more than six times (since 3 points are required on both sides of the pencil) of the total pencil size, resulting in a huge memory penalty. Furthermore, not all the values in the ghost layer would be useful, since the number of points near the boundaries would on average be smaller than the number of spline coefficients required for interpolation (typically N^3 is much larger than N_p). Thus the strategy utilizing ghost layers is not a viable one, specially at the Petascale problem sizes.

A possible strategy is to keep the spline coefficients in the remote memory and transfer them individually for every particle whenever required. However, the information required for each particle is different on every MPI task and each task at any given time, is responsible for thousands of particles. In such a scenario, the use of one-sided communication is particularly beneficial since it greatly reduces the synchronization required between the communicating tasks. The underlying idea is to start calculating the sum in (3.3) and then fetch the required spline coefficients using one-sided communication, for the particles near the sub-domain boundaries. The communication is still restricted in a local zone between the neighbors, but the amount of synchronization has been greatly reduced. Also in general, any processor geometry (such as 32 × 8192 for the 8192^3 grid) can be considered. This one sided communication can be performed using the `MPI_GET` call provided by the MPI 3.0 standard or CAF on Cray machines such as Blue Waters (NCSA). The use of CAF in this regard is faster, since the message sizes are very small and CAF greatly exploits the memory locality due to the inherent localized nature of communication. A global coarray for the spline coefficients is be formed and used for the interpolation, by accessing the remote memory using the coarray dimension. The use of `MPI_GET` also achieves the desired result, however because of larger overhead and synchronization costs, it is not as good as using CAF.

3.2.3 Performance

The main benefit of the local approach is the local nature of the communication between neighboring MPI tasks. Since the processor grid is 2D, a given MPI task has 8 immediate neighbors (since there are 4 faces and 4 edges shared between sub-domains on each task). This is true for tasks even on the boundaries of the domain due to periodic boundary conditions. For example in figure 2.1, the neighbors of $P5$ are $P0$, $P1$, $P2$, $P6$, $P10$, $P9$, $P8$ and $P4$, whereas the neighbors of $P0$ are $P12$, $P13$, $P1$, $P5$, $P4$, $P7$, $P3$ and $P15$. In general we can scale up to any number of processors and the communication pattern always will remain local. As a result, the communication costs associated with interpolation are very small. Table 3.3 shows the particle tracking timings using the local approach. The same cases as reported earlier for global approach (in table 3.1) are chosen. The expensive collective communication calls are replaced by two local communication calls. The first corresponds to communication of spline coefficients (for particles near the boundaries) from neighboring tasks for interpolation and the second corresponds to migration of particles in case they move out of the sub-domain boundaries. As it can be seen, the timings for the local approach are significantly better. The inherent local nature of communication allows for almost complete avoidance of any other network traffic, allowing for very good scaling of the communication costs. The timings for computations are also significantly less as the summation is calculated only for the local population of particles (unlike the global approach where a partial sum is formed for all the particles). Table 3.4 shows the timings for four times as many particles in table 3.3, similar to table 3.2 for the global approach. While the timings increase proportionally with the number of particles, the overall cost is still much less compared to the global approach. Finally in table 3.5, we present the timings at the largest problem size we have run, for different numbers of particles. Except for the cost of calculating the spline coefficients, all other costs are proportional to the number of particles. However, the total cost for particle tracking is substantially less. In fact, this dramatic improvement in performance has allowed us to run up to 300 million particles in the 8192^3 DNS run. If we compare the timings for 64M particles between the global and local approach, we find that the local approach performs over 10X faster (and given the trend, order 40X for the case of 256M particles).

While the performance for the local approach is very good, there are still a few points to consider. An important point is the effect of processor grid on particle tracking. In the local approach, communication occurs only when particles are near the boundary (or when they move out of the sub-domain boundary). Since the turbulence is homogeneous, we can assume that the particles are distributed more or less uniformly in space. As a result, the likelihood of a particle being near a boundary depends on (1) how many total particles are being tracked and (2) the size of the sub-domain, i.e., the value $N/P_{row} \times N/P_{col}$ (we can ignore the third direction, since entire data along that direction is always present on each task). For a fixed value of P $(= P_{row} \times P_{col})$, more particles will be near the boundary if the sum $P_{row} + P_{col}$ is higher, since the sum is a measure of the perimeter of the sub-domain (larger perimeter would imply a large boundary for the same area given by $P_{row} \times P_{col}$). Thus the optimal performance, in theory, is expected for $P_{row} = P_{col} = \sqrt{P}$, which gives the smallest perimeter for a give value of P. However, such a domain decomposition gives sub-optimal performance for the Eulerian part (which performs best for $P_{row} \ll P_{col}$ as discussed before in § 2.3). As a result, the optimal processor grid required for the Eulerian and the Lagrangian parts directly conflict with each other. Since the Eulerian part takes more time due to the nature of 3D FFTs, the processor grid is chosen to get the best Eulerian performance. Another important point to consider is the load imbalance across all MPI tasks in the local approach. Since the particles move around between tasks, some MPI tasks might have a significantly larger number of particles than others. However since the overall cost for interpolation in the local approach is so less (less than 5% of the total time per step, at the largest problem size of 8192^3 considered in this work), we can safely ignore the need for working on load balancing currently.

3.2.4 I/O considerations

An important task in particle tracking is writing out the data for particle positions and velocities. For postprocessing (as discussed in next section), the entire time history of particles is required at multiple of a sampling time interval, which is a fraction of Kolmogorov time scale (on average thousands of time steps are written out at the largest Reynolds numbers). Also many Lagrangian statistics require numerical differentiation or integration with respect to time (more details in Chapter 5) and thus require a small output step for accuracy. Since the I/O is performed so frequently for particle tracking, it is obviously important for it to be as efficient as possible. Given the different nature of global and local approaches, both require separate considerations for efficient I/O.

In the global approach, particles always belong to the MPI task they are initiated on. As a result, the I/O for global approach is simple. At every output step, we choose P_s MPI tasks which are always responsible for writing out the data, such that P_s is a factor of P and $1 < P_s < P$. These P_s tasks are uniformly scattered in the entire communicator, for example, tasks 0, P/P_s, $2P/P_s$, ... ,$(P_s - 1)P/P_s$. These tasks collect the data from succeeding $P/P_s - 1$ tasks (or P/P_s tasks including itself) and write out the data in a serial fashion into P_s output files simultaneously. Based on the number of particles (N_p), the value of P_s is chosen such that N_pP_s/P is a constant for every DNS run (essentially each task writes out the same amount of data). Furthermore this value is determined for any supercomputer to get the best overall I/O bandwidth from a simple parametric study.

For the local approach, particles constantly move around between MPI tasks. Thus the above mentioned approach cannot be used directly. To keep track of particles, each particle is assigned an unique integer index, which always remains the same regardless of where particles go. One approach is to send the information for every particle, to the MPI task it was initiated on (using this integer index) and then write out the data using the same I/O method employed in the global approach. Essentially, a parallel sorting is required at every output step, where the particles are sorted in the same manner as they were initiated in and then the same I/O method is used to write out the data. However doing this parallel sorting on $\mathcal{O}(10^5-10^6)$ MPI tasks is very expensive. As a result, the sorting is now performed using a postprocessing approach. First the unsorted particle position and velocities, along with the unique indices are simply written out using a strategy similar to that used in the global approach. Then a 'sorting' code is run as a post-processor on this raw data using a much smaller number of MPI tasks. This allows us to run the DNS code efficiently on $\mathcal{O}(10^5-10^6)$ MPI tasks. Since the number of particles can also be very large, we have further employed parallel I/O in the DNS code to write out the unsorted data. The strategy is still the same, where P_s blocks of MPI tasks are chosen, such that each P/P_s group of tasks collectively write out their data in parallel. For convenience, P_s is chosen to be equal to P_{col}, such that P_{row} group of tasks write out one file each. This way the parallel I/O is restricted within the node (the communication as a result is very fast and scalable), since P_{row} is typically chosen to be equal to the number of processors on a node.

3.3 Postprocessing and Backward tracking

As mentioned earlier, a direct way of tracking particles backward in time is to store the Eulerian velocity fields (as integrated forward in time from say $t = 0$ to T) at every time step. Particles are introduced in the domain at $t = T$ and integrated backwards in time to $t = 0$ using (3.1). However as discussed earlier, this approach is prohibitively expensive at large Reynolds numbers due to the storage requirements which grows similarly to the computational cost (R_λ^6).

To avoid the severe storage constraints noted above, we have developed a new algorithm based on postprocessing of saved forward trajectories to obtain both forward and backward statistics. A large population of particles is tracked forward in time from $t = 0$ to T along with the Eulerian velocity field and the positions and velocities of particles are written out at reasonably small time intervals (normally a fraction of Kolmogorov time scale). Then these forward trajectories are inverted using the transformation $t' = T - t$, where t' corresponds to the backward time. This inversion can be applied since the Eulerian flow is statistically stationary (Buaria *et al.* 2015). While this approach has similarities with techniques used by experimentalists (Berg *et al.* 2006; Jucha *et al.* 2014), the number of particles and pairs we consider in this work are much larger. Single particle statistics like velocity autocorrelation, mean-square displacement, etc. (Yeung & Pope 1989) are easily obtained for both forward and backward reference frames. In fact, because of stationarity both forward and backward single particle statistics would be identical (Sawford *et al.* 2005). However, obtaining two particle statistics is a non-trivial task.

The typical approach to obtain two particle statistics in the forward case, is to introduce pairs of exact initial separation at $t = 0$ and track them forward in time (Yeung & Borgas 2004). Doing the same for backward case would require the expensive data storage method, as we cannot control the final separations of the particles (at $t = T$, which also is the initial separation for backward frame at $t' = 0$) in the current approach. Instead particle pairs are now formed by choosing all the unique combinations of two single particles. This results in a smooth variation of initial separations over a continuous probability distribution and statistics are formed by collecting samples of the initial separation distance into bins of a desired width. As a result, obtaining both forward and backward statistics is a postprocessing task. Similarly triangles and tetrads can also be formed by choosing three and four particles respectively. The details of this postprocessing algorithm are discussed next.

3.3.1 Pairs

In principle, for a population of N_p particles we can form a maximum of $N_p(N_p - 1)/2$ distinct pairs. However for a nominal value of $N_p = 10^6$ (as we will see later, the value of N_p chosen can be much higher than that), the total number of pairs is $O(10^{12})$. Since we need to process the data at possibly over a thousand time steps, the data analysis also requires massively parallel processing. It is also important to note that within each population and at any given time instant there may be relatively few pairs which are close together, but many more which are relatively far apart. Consequently it may be difficult to obtain sufficient samples of pairs with small initial separation (r_0) while for large initial separation it is not necessary to count all the samples. Our goal is thus to count as many pairs as possible and necessary, for pairs that are close together at $t = 0$ or $t = T$, while keeping the overall cost manageable using a systematic approach that also provides a means of assessing the degree of sampling uncertainty.

To explain our counting algorithm we consider analyzing a population of N_p particles using M distinct parallel processes (or MPI tasks). The particles are divided into M independent sub-populations, each of size N_p/M and held by a distinct MPI task. We also sub-divide each N_p/M sub-population into two halves, of $N_p/(2M)$ particles each. The algorithm then goes through the following steps. First, on each MPI task, $(N_p/2M)^2$ pairs are formed by selecting, for each pair, a particle from the first half and a particle from the second half of the same sub-population, giving $N_p^2/(4M)$ pairs upon summing over M MPI tasks. To obtain more pairs, we move the second half of each sub-population, in pipe-lining fashion, from one MPI task to the next, and then form another $N_p^2/(4M)$ pairs in the same manner. If this procedure is repeated a maximum of M times we obtain $N_p^2/4$ pairs, regardless of the value of M. Second, we can form new pairs by swapping the first half of one sub-population with the second half of each of the other $(M - 1)$ sub-populations. Proceeding systematically in the same manner as above produces another $(N_p^2/4M)(M - 1)$ pairs. Finally, we can also form pairs within each half of each sub-population, which gives another $(N_p/2M)(N_p/2M - 1)M$ pairs. The sum of the three subtotals above is the same as the theoretical maximum of $N_p(N_p - 1)/2$. Yet, by avoiding forming pairs directly across different sub-populations residing on different MPI tasks the communication cost for this calculation is inherently low. The systematic nature of the approach, further allows us to parallelize the work on each MPI task using OpenMP threads and exploit modern SIMD (single instruction, multiple data) architectures by fully vectorizing the time step loop (which is kept to be the innermost for this reason).

In post-processing of particle pairs, our practice is to keep the number of particles on an MPI task, i.e., N_p/M fixed. Then depending on how many particles are being processed we set the total number of MPI tasks accordingly. The underlying idea is have sufficient particles to fully utilize OpenMP within a MPI task, but also not have too many particles such that memory becomes an issue. As noted earlier, the basic procedure involved in post-processing is to form pairs on MPI tasks and then cycle a sub-population of particles. Then this process is repeated to go through all the pairs. Since N_p/M is constant, the time for each basic procedure is also same across different runs. In Table 3.6, the timings for such a procedure are given. It can be seen that the code scales almost perfectly up to 8 OpenMP threads on Stampede (TACC). On going from 8 to 16 threads, the scalability is not perfect due to the penalty in memory access across a NUMA node (each node on Stampede has two NUMA nodes with 8-cores on each). Also the time spent in communication is trivially small compared to that spent in computations. As a result, the code is almost entirely computation bound and performs consistently at the reported flop rate of about 6 GF/s per thread, which is about 30% of the peak flop rate [1].

Another important parameter in post-processing is the number of time steps. Due to the nature of the algorithm forming the pairs, it would be most efficient to compute the statistics for all time steps together. As a result, the time step loop is made to be the innermost and resulting in very efficient vectorization. Table 3.7 shows the dependence on number of time steps on the performance of the code. As one can observe, the efficiency of the code improves with increasing number of time steps until it saturates. This is because increasing the number of time steps helps to utilize more vector units until a point is reached when all vector units are saturated. The communication time also increases with the number of time steps, but still is trivially small. For very large time steps, sustained performance can still be obtained by using simple techniques like loop/cache blocking. Thus this algorithm allows us to form all the possible particle pairs in a very systematic way, such that we can very efficiently parallelize all the work using hybrid MPI/OpenMP programming.

In backward tracking, we begin with full knowledge of the fluid particle velocities and positions at the output time steps $\{t = 0, h, 2h, ...T - h, T\}$. As mentioned earlier, we can define the backward time as $t' = T - t$, and thus associate initial conditions for the

---

[1] *https://www.tacc.utexas.edu/stampede*

backward problem (at $t' = 0$) with fluid particle properties at $t = T$ from a forward numerical simulation, without any further numerical integration. However a careful consideration of the nature of periodic boundary conditions is necessary. In the forward DNS, at $t = 0$, the position coordinates of all fluid particles are initialized as uniformly distributed random variables scaled such that all particles lie within a "primary" domain of size $(2\pi)^3$. Subsequently, as time evolves, because of the unbounded nature of homogeneous turbulence, an increasingly large fraction of the particles will be found in periodic images of the primary domain. The velocities of particles lying outside the primary domain remain well-defined, being the same as if the particles were inside the domain, with each coordinate shifted by an integral multiple of the length of the domain on each side. Thus, for example, a particle at position $(2k_1\pi + x_1, 2k_2\pi + x_2, 2k_3\pi + x_3)$, where the k_i are integers and $0 \leq x_i \leq 2\pi$, experiences exactly the same velocity as a particle at position (x_1, x_2, x_3), which is in the primary domain. This consideration allows us to formulate a backward tracking problem with all particles starting (at $t' = 0$) inside the primary domain: essentially, at $t = T$ we bring all particles back into the primary domain by adding or subtracting a multiple of 2π in all three coordinate directions. The position coordinates of each particle at all earlier forward times are also shifted in the same way, while velocities are not affected. As a consequence, in backward dispersion, as we travel back to earlier times (at increasing t'), an increasingly large fraction of the particles will be found in periodic images of the periodic domain, in a manner analogous to forward dispersion at large time t.

In previous forward-tracking studies (Yeung & Borgas 2004; Sawford *et al.* 2008) only particle pairs with several prescribed values of initial separation (r_0) were considered. In our present formulation the initial separation is random. The likelihood of samples in different ranges of r_0 is characterized by its probability density function (PDF), $f(r_0)$ (throughout this paper we use $f(\cdot)$ as a generic symbol for PDFs), and most of the results presented in this paper are statistics averaged over samples of particle pairs whose r_0 fall into a series of designated intervals. Figure 3.1 shows the PDF of r_0 normalized by either the length of the domain (L_0) or the Kolmogorov length scale (η) (with all PDFs normalized such that the area under the curve, if plotted on linear scales, is unity). On the left of this figure $f(r_0/L_0)$ is independent of Reynolds number except that a larger particle count used in the higher Reynolds number simulation provides more samples at scale sizes much smaller than L_0. For a uniform distribution of particles in three dimensions, the cumulative distribution of pair separations is a power law with an exponent equal to the correlation dimension (Grassberger & Procaccia 1983), which in this case is just the spatial dimension, three. Thus for $r_0 \ll L_0$ the cumulative distribution function scales as $(r_0/L_0)^3$, such that $f(r_0/L_0) \propto (r_0/L_0)^2$, which explains the quadratic growth seen to hold well up to $r_0 \approx L_0/2$ (the radius of the largest sphere that can be wholly contained in the primary solution domain). For r_0 exceeding L_0 the PDF is seen to drop quickly towards 0 for r_0 at its upper bound of $\sqrt{3}L_0$ (equal to the length of the diagonal in the cubic domain). We are interested mostly in initial separations within the dissipation and inertial sub-ranges which correspond to $r_0 \ll L_0$. If we consider (in the right of Fig. 3.1) the PDF of r_0/η then the PDFs at different Reynolds numbers differ significantly. Sampling for small r_0/η becomes more difficult at higher Reynolds number as η becomes smaller (while L_0 is fixed). In our data, for $R_\lambda = 140$ the PDF of r_0/η appears to be reasonably well-sampled for r_0/η down to about 1/4. In the $R_\lambda = 1000$ simulation accuracy at such a small r_0 would require many more samples than we have used. As a result, for our higher Reynolds number datasets we mainly present results for r_0/η from 1 upwards.

It should be noted that, provided periodic boundary conditions are properly accounted for, the second law of thermodynamics and incompressibility ensure that an initially uniform distribution of fluid particles remains so, and that therefore the PDFs of forward and backward r_0 are the same. In our data we have observed this is true — the forward and backward PDFs differ only slightly due to sampling noise for r_0 at its smallest values.

3.3.2 Triangles and tetrads

The general strategy for forming triangle and tetrads is similar to that of forming pairs. We can now divide the population on each MPI task into four groups of $N_p/4M$ each. For triangles, we can pick one particle from three groups at a time, whereas for tetrads we can pick one particle from each group. In theory, for N_p particles one can form a total of

$N_p(N_p-1)(N_p-2)/6$ unique triangles and $N_p(N_p-1)(N_p-2)(N_p-3)/24$ unique tetrads. However, counting all the possible triangles or tetrads is clearly out of question, since for $\mathcal{O}(10^6)$ particles we are looking at $\mathcal{O}(10^{18})$ triangles and $\mathcal{O}(10^{24})$ tetrads (which is almost impossible even by Petascale standards). Furthermore, not every triangle and tetrad formed this way is of interest. As a result, we only consider *equilateral triangles* and *regular tetrads* (a tetrad with all sides equal) which have received considerable attention in forward tracking studies (Chertkov *et al.* 1999; Pumir *et al.* 2000; Xu *et al.* 2008; Hackl *et al.* 2011).

Since the separation distances between particles are distributed randomly (as highlighted in previous section and also figure 3.1), we cannot obtain perfect equilateral triangles or regular tetrads. Instead we use a binning strategy, whereby a sample is identified when all its sides fall within the same bin (note a triangle with all three sides equal is always equilateral and a tetrad with all six sides equal is always regular). The resulting triangles and tetrads can now be sampled in a similar fashion as pairs, by treating them as an ensemble of three and six pairs (for each side) respectively. The variable r_0 now represents the length of each side for a triangle or tetrad and a sample is found when all the sides fall in the same bin around a given r_0. This strategy allows us obtain results from a more modest number of samples, which greatly reduces the required computational cost. As we saw earlier for pairs, while samples for reasonably large r_0 are readily available, samples for small r_0 are much rarer. For the triangles and tetrads, samples of small r_0 occur even rarely as three and six sides respectively need to simultaneously satisfy the same sampling condition. In order to achieve good sampling at small r_0, we would have to potentially scan through all the possible samples (just as in the case of pairs). However such a task for triangle and especially tetrads is extremely difficult. To counter this, we have come up with a different approach as discussed next.

As mentioned earlier for pairs, for a cubic domain of length L_0, the largest possible distance between two particles is $\sqrt{3}L_0$. Now if we divide the entire domain into sub-cubes of length L_0/F, where F is some integer factor greater than unity, then the largest distance available becomes $\sqrt{3}L_0/F$. Since N_p particles are scattered in the entire domain, after sorting spatially we will have N_p/F^3 particles in each sub-cube on average. The exact numbers will be slightly less or more, but since the overall distribution is homogeneous, we can approximately take it to be this for every sub-cube. Now if triangles or tetrads formed are restricted to each sub-cube, then the total number of samples to scan through scales as N_p^3/F^9 and N_p^4/F^{12} respectively. By appropriately choosing the value of F, we can dramatically reduce the number of samples we have to scan through to find the equilateral triangles and regular tetrads. The samples obtained are also restricted to a maximum size set by the size of the sub-cube. This strategy greatly reduces the computational cost of studying triangles and tetrads. However, for the smallest r_0, it is still impossible to obtain decent sampling, since the samples are non-existent in the first place. In general for a given, r_0, the number of samples for pairs will be much larger than the number of samples for triangles, which in turn would be much larger than the number of samples for tetrads. For a given value of N_p, the total number of samples are restricted and thus sampling at smallest r_0 gets progressively worse in going from pairs to triangles to tetrads. As a result the smallest well sampled r_0/η for triangles or tetrads is somewhat higher than smallest well sampled r_0/η for pairs and also depends on the Reynolds number. For $R_\lambda = 140$, good sampling for $r_0/\eta \geq 1$ is obtained, whereas for $R_\lambda = 1000$, good sampling is available for $r_0/\eta \geq 8$ only. (discussed more in Chapter 6).

3.4 Summary

The key task in particle tracking is the interpolation of fluid velocity at particle location from the neighboring grid points. We have presented two approaches for this purpose, namely the global and the local approach. In the global approach, the particles are always located on the MPI tasks they are initialized on, while the information required for interpolation is globally communicated. In the local approach, the particles freely change MPI tasks as they are integrated forward in time, such that the required information for interpolation is always locally available. While the global approach has been used previously for smaller to moderate problem sizes, it scales poorly at Petascale problem sizes. For this reason, the local approach has been developed and implemented in the DNS code. For all problem sizes, the local approach is found to scale significantly better.

Based on the trajectories of particles saved in DNS, we have developed and implemented a new postprocessing algorithm to obtain statistics of particle pairs. A hybrid MPI/OpenMP approach is used, in which particles are distributed across a large number of processors and two-particle statistics are calculated by systematically forming pairs from unique combinations of single particles. The code scales almost perfectly with both the number of MPI tasks and OpenMP threads. Extensions to triangles and tetrads are also discussed.

Table 3.1: Particle tracking timings on Blue Waters (NCSA) for the global approach for 16M particles. The problem size and number of processors correspond to weak scaling argument for the Eulerian part.

Grid points	2048^3	4096^3	8192^3
CPU cores	4096	32768	262144
Proc. Grid	16x128	16x1024	32x4096
No. of threads	2	2	2
Spline coefficients	1.507	3.329	5.121
Allgather	0.912	5.072	11.82
Computations	0.288	0.261	0.364
Reduce+Scatter	0.516	1.438	2.062
Total time	3.278	14.11	19.81

Table 3.2: Particle tracking timings on Blue Waters (NCSA) for the global approach for 64M particles. The problem size and number of processors correspond to weak scaling argument for the Eulerian part.

Grid points	2048^3	4096^3	8192^3
CPU cores	4096	32768	262144
Proc. Grid	16x128	16x1024	32x4096
No. of threads	2	2	2
Spline coefficients	1.493	3.290	5.006
Allgather	3.052	7.034	43.58
Computations	1.134	1.048	1.464
Reduce+Scatter	2.052	4.404	6.032
Total time	7.804	16.42	55.27

Table 3.3: Particle tracking timings on Blue Waters (NCSA) for the local approach for 16M particles (similar to table 3.1)

.

Grid points	2048^3	4096^3	8192^3
CPU cores	4096	32768	262144
Proc. Grid	32x128	32x1024	32x8192
No. of threads	1	1	1
Spline coefficients	1.419	2.295	4.905
Comm. interpolation	0.601	0.378	0.140
Computations	0.025	0.003	0.001
Update particles	0.001	0.004	0.032
Total time	2.064	2.751	5.120

Table 3.4: Particle tracking timings on Blue Waters (NCSA) for the local approach for 64M particles (similar to table 3.2)

.

Grid points	2048^3	4096^3	8192^3
CPU cores	4096	32768	262144
Proc. Grid	32x128	32x1024	32x8192
No. of threads	1	1	1
Spline coefficients	1.422	2.352	4.917
Comm. interpolation	1.150	1.130	0.293
Computations	0.110	0.014	0.002
Update particles	0.003	0.005	0.071
Total time	3.295	3.519	5.273

Table 3.5: Particle tracking timings on Blue Waters (NCSA) for the local approach at 8192^3 using $262,144$ CPU cores (using 32×8192 domain decomposition)

No. of particles	16M	64M	256M
Spline coefficients	4.905	4.917	4.862
Comm. interpolation	0.140	0.293	1.060
Computations	0.001	0.002	0.008
Update particles	0.032	0.071	0.201
Total time	5.120	5.273	6.066

Table 3.6: Timings on Stampede (TACC) with 200 time steps and 16384 particles on each MPI task

OpenMP threads	1	2	4	8	16
Computations (secs)	100.37	50.58	24.44	12.25	7.41
Communication (secs)	0.047	0.042	0.038	0.043	0.035
Flop Rate (in GF/s/thread)	5.56	5.68	5.88	5.89	4.85

Table 3.7: Timings on Stampede (TACC) with 16384 particles on each MPI task, using 8 OpenMP threads

Time steps	10	50	100	200	400
Computations (secs)	1.346	3.368	6.204	12.25	23.620
Communication (secs)	0.001	0.009	0.021	0.043	0.088
Flop Rate (in GF/s/thread)	2.67	5.33	5.79	5.89	6.09

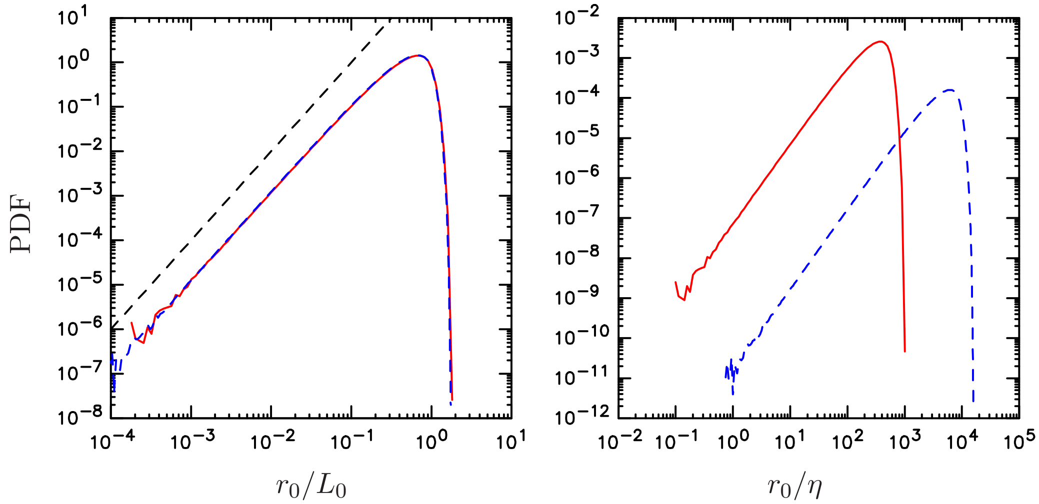

Figure 3.1: Probability density function (PDF) of initial separation normalized by length of domain (left) and by Kolmogorov scale (right), at Reynolds numbers 140 (solid lines, in red) and 1000 (dashed lines, in blue), with number of particles as given in Table 5.1. In the left frame a dashed line of slope 2 in black shows quadratic variation up to $r_0 \approx L_0/2$.

CHAPTER IV

RELATIVE DISPERSION STATISTICS OF FLUID PARTICLES

4.1 Introduction

Turbulent relative dispersion is usually understood as the spreading of a pair of particles relative to each other, under the influence of chaotic motions in a turbulent flow. The concept can be applied to fluid particles, which exactly follow the fluid motion, molecules which additionally undergo Brownian motion and to 'real' or inertial particles whose trajectories differ from those of fluid particles because of effects or inertia or buoyancy. In this chapter, we investigate the trajectories of fluid particle pairs, whereas the study of molecular pairs is the focus of next chapter. As discussed earlier in § 1.1, for the relative dispersion between a pair of fluid particles there is much interest in the classical Richardson scaling (Monin & Yaglom 1975; Sawford 2001) which has been postulated to hold under inertial sub-range conditions with respect to both length scales and time scales. In general, because the range of time scales increases with Reynolds number less rapidly than the range of length scales, Kolmogorov similarity for Lagrangian statistics is relatively difficult to observe without ambiguity (Sawford & Yeung 2011). For forward in time studies, numerical simulations at relatively high Reynolds number have allowed robust estimates of the Richardson constant (Sawford *et al.* 2008), at least in isotropic turbulence. However, backward dispersion is still a major challenge. Using the new numerical breakthroughs described in Chapter 3, our first objective is to understand the fundamental characteristics of backward dispersion over a range of Reynolds numbers.

Earlier studies of backward tracking (Sawford *et al.* 2005; Berg *et al.* 2006) have indicated that backward dispersion is similar to forward dispersion at both very short and very long time scales but stronger at intermediate times of travel. Naturally, we are interested in how this difference varies with Reynolds number, and whether clear inertial sub-range behavior similar to Richardson scaling can be identified for backward as well as forward statistics. It is clear that access to data over a substantial range of Reynolds numbers beyond those necessary to observe inertial sub-range scaling in Eulerian statistics (Yeung & Zhou 1997) is essential. Our results given later in this chapter also indicate that a higher Reynolds number is needed to observe clear Richardson scaling in backward dispersion compared to the forward case. A more recent study (Jucha *et al.* 2014) has shown that an asymmetry between forward and backward dispersion starts developing from $t = 0^+$ (where 0^+ represents an infinitesimal positive increment). This asymmetry can be obtained by using a simple Taylor series expansion and is found to grow as t^3 in time. We investigate this asymmetry in more details to understand, if possible, any relation it has with the Richardson scaling regime (which also grows as t^3 in time). We also analyze the behavior of higher order moments and the so-called distance neighbor function in Richardson's theory.

4.2 Simulation parameters and Database

In order to ensure sufficient samples of particle pairs close together at either the beginning or the end of the simulation, it is necessary to track a much larger population of fluid particles than in studies of one-particle statistics (Yeung *et al.* 2006b) or of two-particle statistics with only several discrete values of the initial separation (Sawford *et al.* 2008). As a result the computational cost as well as data requirements are dominated by the particle tracking A combination of distributed (message passing) and shared-memory (multithreading) parallel processing that takes advantage of the multi-cored nature of current supercomputing platforms has been found to be effective (details discussed in Chapter 3).

For clarity we define here various scales used to characterize the flow. The Kolmogorov length $\eta = \left(\nu^3/\langle\epsilon\rangle\right)^{1/4}$, velocity $\upsilon_\eta = \left(\nu\langle\epsilon\rangle\right)^{1/4}$ and time $t_\eta = \left(\nu/\langle\epsilon\rangle\right)^{1/2}$ scales, where $\langle\epsilon\rangle$ is the mean rate of dissipation of turbulence kinetic energy and ν is the kinematic viscosity, are representative of the scales on which dissipation of energy is effective (the overbar denotes quantities that are averaged over the Eulerian fields in both space and time, since the flow considered is stationary and homogeneous). We can also define length $L = \sigma_u^3/\langle\epsilon\rangle$, velocity σ_u and time $T_E = \sigma_u^2/\langle\epsilon\rangle$ scales representative of the energetic eddies, where σ_u is the standard deviation of a component of the turbulent velocity. Note that L

is related empirically (Sreenivasan 1998) to the integral length scale L_1 for the longitudinal Eulerian velocity correlation function. Our recent simulations (Yeung *et al.* 2012) give $L_1/L \approx 0.46$, with little variation for $R_\lambda \geq 140$ (although this ratio may be flow-dependent). The advantage of using L rather than L_1 is that then the energy containing scales and the Kolmogorov scales are connected very simply via the turbulence Reynolds number $Re = \sigma_u L/\nu$. With these definitions the Taylor scale Reynolds number, which following common practice we use to characterize the flow, is given by $R_\lambda = (15Re)^{1/2}$ for isotropic turbulence.

Table 4.1 shows several basic parameters of the simulations used. In all cases the solution domain cubic with side $L_0 = 2\pi$, and the grid spacing approximately twice the Kolmogorov length scale η. Although the value of the spatially averaged dissipation rate varies somewhat in time, since the forcing scheme used (Donzis & Yeung 2010) tends to limit such variations both η and t_η can be taken as constant throughout each simulation. Increases in Reynolds number are achieved by reducing the viscosity with corresponding refinement of grid spacing to maintain the small-scale resolution, while the forcing parameters that control the large scales are unchanged. For $R_\lambda \leq 650$ the values for the ratio of the Lagrangian integral time scale to the Kolmogorov time scale T_L/t_η were calculated by integrating over the Lagrangian velocity auto-correlation and are in good agreement with the large-Reynolds number limit $2R_\lambda/(15^{1/2}\tilde{C}_0)$, with the proportionality constant $\tilde{C}_0 = 6.5$ obtained from earlier estimates (Sawford *et al.* 2008). For $R_\lambda = 1000$, where the simulation time period T is not sufficiently long for T_L to be obtained directly, the time scale ratio was calculated from this large-Reynolds number limit. The output time interval (h) should be small compared to t_η, especially in the analysis of pairwise relative velocities. The particle count N_p is chosen to be an integer multiple of the number of CPU cores used to perform the simulations. The values of P shown in the table range from 4M to 32M, where "M" is a common shorthand for $2^{20} = 1,048,576$. Typically we have increased P in proportion to N in order to better sample a wider range of times (except for the $R_\lambda = 1000$ simulation, where the computational cost would have been too great). The number of time intervals is proportional to T_L/t_η, which varies like R_λ. Thus the storage requirement scales as NR_λ. Incidentally, from Table 4.1

we can infer that R_λ itself scales as $N^{2/3}$, which is consistent with classical scaling for the range of length scales (L_1/η) present in the flow as well.

4.3 Statistics of Forwards and Backward Dispersion

We denote the instantaneous position vectors of two particles forming a pair by $\mathbf{x}^{(1)}(t)$ and $\mathbf{x}^{(2)}(t)$. For forward dispersion the separation vector at time t is

$$\mathbf{r}(t) = \mathbf{x}^{(2)}(t) - \mathbf{x}^{(1)}(t) \tag{4.1}$$

whereas for backward dispersion we consider

$$\mathbf{r}(t') = \mathbf{x}^{(2)}(t') - \mathbf{x}^{(1)}(t') \tag{4.2}$$

with t' defined to be $T-t$ as noted earlier. Note that for simplicity we have dropped the "+" superscript notation for Lagrangian quantities, and rely on the context and the arguments to distinguish between Lagrangian and Eulerian quantities.

Because the turbulence is stationary, any statistic evaluated at time t' is equivalent to that evaluated at time $-t$. Thus comparisons between forward and backward dispersion will usually be made via the properties of $\mathbf{r}(t)$ and $\mathbf{r}(t')$, with t and t' taking the same values. For convenience, we may also use the same notation for both forward and backward quantities when the context is clear. In isotropic turbulence a basic quantity is the separation distance, i.e. magnitude of the separation vector, given the initial separation $r_0 = |\mathbf{r}(0)|$ in either forward or backward frames. As noted in Sec. II our sampling procedure gives statistics averaged over particle pairs whose values of r_0/η fall into designated bins. We choose bins such that the upper bound is four times the lower bound, and in order to resolve the dependence on r_0 more precisely we use overlapping bins with $2^{i-3} \le r_0/\eta < 2^{i-1}$ for $i = 0, 1, 2, 3, ...$ onwards. In this work, the notation $\langle\cdot\rangle$ is used to represent these bin-wise averages, and each bin is identified by the geometric mean of its upper and lower bounds i.e., $\tilde{r}_0/\eta = 2^{i-2}$ for $i = 0, 1, 2, 3, ...$ onwards. This binning strategy is a trade-off between ensuring an adequate number of samples in each bin, resolving the dependence on $\tilde{r}_0$, and ensuring that results for each $\tilde{r}_0$ are distinct. Numerical results including the relative dispersion $\langle r^2(t)\rangle$ and mean-squared relative displacement $\langle|\mathbf{r}(t) - \mathbf{r}(0)|^2\rangle$ (which measures the change of separation over time) are presented as functions of $\tilde{r}_0$. The mean-squared relative displacement has the advantage of being more sensitive to the fundamental flow physics, since it is less dominated by the initial separation at early times. Results given below include second- and higher-order moments, as well as the evolution of the PDF of $r(t)$ in comparison with Richardson's theory (Batchelor 1952*a*; Monin & Yaglom 1975) on the so-called distance-neighbor function at intermediate times.

4.3.1 Second Moments and Richardson scaling

It is well known (Batchelor 1950) that, in classical theory, the process of relative dispersion evolves through three distinct regimes in time, known as ballistic, inertial and diffusive ranges respectively. Traditionally, for a fixed initial separation r_0 the extent of the ballistic range has been quantified for inertial sub-range initial separations by the Batchelor time scale $t_0 = r_0^{2/3}/\langle\epsilon\rangle^{1/3}$. In the present context, for each bin identified by a given $\tilde{r_0}$, this is generalized to $t_0 = \langle r_0^{2/3}\rangle/\langle\epsilon\rangle^{1/3}$ which measures memory of the initial separation for pairs in the bin centered on r_0 in the inertial sub-range. For the mean-squared relative displacement defined above, these asymptotic behaviors can be summarized by writing

$$\langle|\mathbf{r}(t)-\mathbf{r}(0)|^2\rangle = \begin{cases} \langle D_{LL}(r_0) + 2D_{NN}(r_0)\rangle t^2 & \text{if} \quad t \ll \max(t_\eta, t_0) \\ g\langle\epsilon\rangle t^3 & \text{if} \quad \max(t_\eta, t_0) \ll t \ll T_L \\ 12\sigma_u^2 T_L t & \text{if} \quad t \gg T_L \ , \end{cases} \tag{4.3}$$

where $D_{LL}(\cdot)$ and $D_{NN}(\cdot)$ are Eulerian longitudinal and transverse structure functions, and g is known as Richardson's constant. For bins in the quadratic range of $f(r_0)$, that is, for $\tilde{r}_0 \lesssim L_0/2$ (as noted in Sec. II), it is easily shown that $\langle r_0^{2/3}\rangle = 1.31\tilde{r}_0^{2/3}$. If $\tilde{r}_0$ is in the inertial sub-range and intermittency corrections are neglected the multiplicative factor in the first part of (4.3) can also be replaced by $(11C_2/3)\langle\epsilon\rangle^{2/3}\langle r_0^{2/3}\rangle$ where C_2, the Kolmogorov constant in $D_{LL}(\cdot)$, is close to 2.13 if the Reynolds number is sufficiently high (Sreenivasan 1995; Yeung & Zhou 1997). Both the ballistic and diffusive regimes are kinematic in nature, since their attainment (or otherwise) is determined, respectively, by how small a time step is used in collecting the data and how long the numerical simulation is in physical time units, with no requirement for high Reynolds number. In contrast, dispersion characteristics at intermediate (inertial) times are dependent on the range of physical time scales present, and hence on the Reynolds number of the flow. The form of the condition in the second line of (4.3) also allows for the fact that particle pairs beginning in bins with $\tilde{r}_0 \ll \eta$ can still reach the inertial sub-range and Richardson scaling behavior at sufficiently large times and sufficiently large Reynolds numbers.

Figure 4.1 shows data on the mean-squared relative displacement, normalized by Kolmogorov variables, at the lowest and highest Reynolds numbers in this work. At early times $\langle|\mathbf{r}(t) - \mathbf{r}(0)|^2\rangle$ increases quadratically with slope 2 on log-log plots as expected for the ballistic regime. In this regime particle-pair statistics are determined by the Eulerian properties, which are (with the proviso of statistical stationarity) the same for forward and backward dispersion, as observed. Lines for the largest values of $\tilde{r}_0$ are very close to each other since the Eulerian structure functions approach constant values at large r. At later times, especially for $t \gg T_L$ we observe that the dependence on $\tilde{r}_0$ also becomes weak, and all the curves shown ultimately converge towards a diffusive regime where the growth of mean-squared separation is linear. This approach towards the diffusive limit is clearest for the R_λ 140 simulation which was relatively long ($T \approx 10\ T_L$) but less so for the R_λ 1000 simulation which was carried out only for $T \approx 2.5\ T_L$. A closer examination does show that backward dispersion approaches slope unity faster than forward dispersion.

At intermediate times, when most pairs are at some intermediate distance apart beyond the viscous sub-range, turbulent dispersion is expected to be strongly influenced by inertial effects, which appear in the Navier-Stokes equations as nonlinear terms that, through the transfer of energy from large to small scales, imply non-reversibility in time. Significant differences between forward and backward dispersion are thus expected (Sawford *et al.* 2005; Berg *et al.* 2006). These differences also imply that the Richardson constant g will have different values in the forward and backward reference frames.

To focus on the inertial sub-range behavior, in figure 4.2 we show plots for the compensated mean-square relative displacement $\left\langle(\mathbf{r}(t) - \mathbf{r}_0)^2\right\rangle / \left(\langle\epsilon\rangle t^3\right)$ as a function of time scaled by the Batchelor time scale t/t_0 for a range of initial separations and Reynolds numbers. We see that for each value of $\tilde{r}_0/\eta$ there is a collapse with increasing Reynolds number over a range of times, and that the extent of this range increases with increasing Reynolds number. The upper end of this similarity scaling range is truncated by the transition to diffusive behavior. We also see that, with increasing $\tilde{r}_0/\eta$, the diffusive transition occurs at smaller values of t/t_0 (as the Batchelor time scale t_0 increases). As noted by Sawford *et al.* (2008), for $\eta \ll \tilde{r}_0 \ll L$, in this scaling the mean-square relative displacement collapses to a universal curve, independent of both $\tilde{r}_0$ and Reynolds number, in both the ballistic and Richardson regimes and is truncated only by the diffusive regime. In figure 4.2 this is seen to occur as $\tilde{r}_0/\eta \to 16$ and is essentially complete for $\tilde{r}_0/\eta \geq 32$ (not shown). For $t/t_0 \gg 1$ this universal curve flattens out as it approaches, with increasing Reynolds number, a constant plateau corresponding to Richardson scaling.

For smaller values of $\tilde{r}_0/\eta$ the dispersion is retarded at early times due to the viscous effects in the dissipation sub-range, and falls substantially below data at larger initial separations. However with increasing time particle separations increase on average, leaving the influence of dissipation scale eddies and becoming increasingly influenced by inertial sub-range eddies. As a result the compensated mean-square relative displacement approaches the Richardson plateau from below, again increasingly so with increasing Reynolds number.

Recently (Bitane *et al.* 2012, 2013) introduced a new time scale, which we denote here by $t_B = S_2(\tilde{r}_0)/(2\langle\epsilon\rangle)$, where $S_2(\tilde{r}_0) = \langle D_{LL}(r_0) + 2D_{NN}(r_0)\rangle$, which collapses both the leading order quadratic term in the ballistic range and the Richardson range for all values of the initial separation. For the compensated mean-square relative displacement in this new scaling, shown in the insets to figure 4.2, the curves are simply shifted horizontally so that they collapse at small times. This produces a clearer approach to the Richardson regime at large times for the smaller values of $\tilde{r}_0/\eta$, and hence a more extended plateau region. However, regardless of the use of t_0 or t_B as the normalizing time scale, the picture that emerges is one where the compensated relative dispersion approaches the Richardson plateau from above for $\tilde{r}_0/\eta \gg 1$ and from below for $\tilde{r}_0/\eta \lesssim 1$. Indeed, in the forward case shown in the left panel of figure 4.2 we see that for $\tilde{r}_0/\eta = 4$, which is large enough for viscous effects to vanish at relatively early times, and small enough for t_0 to be much smaller than T_L, there is a plateau at a height approximately 0.55.

In the backward case shown in the right panel, there is a clear indication that the Richardson plateau is somewhat higher than in the forward case, consistent with the greater growth rate at intermediate times in figure 4.1. As a result of this increased growth rate, the initial conditions are forgotten more quickly so the backward case trends towards the plateau at earlier times than in the forward case. On the other hand, this faster growth also means backward relative dispersion approaches the diffusive regime more quickly, thus truncating the Richardson plateau somewhat prematurely at large times. This is seen most clearly for $\tilde{r}_0/\eta = 4$ at $R_\lambda = 1000$, where again there is a plateau, but starting and ending earlier than for the forward case. The trends with Reynolds number and initial separation are the same as for the forward case and consistent with a larger backward Richardson constant, $g_b \approx 1.5$.

A more precise way to search for the presence of, and to quantify, a Richardson scaling range is (Sawford *et al.* 2008; Hackl *et al.* 2011) to plot the so-called cubed-local-slope (CLS)

$$\frac{1}{\langle \epsilon \rangle} \left(\frac{d}{dt} \left[\langle r^2 \rangle^{1/3} \right] \right)^3 \tag{4.4}$$

versus Batchelor-scaled times (t/t_0). If a well-defined Richardson scaling range exists then a plot of the CLS should show a plateau with height equal to the Richardson constant over a range of separations $\tilde{r}_0$ and a range of times $t_0 \ll t \ll T_L$.

We show in figure 4.3 data for three Reynolds numbers and four values of $\tilde{r}_0/\eta$. In general data from the R_λ 650 simulation are closer to that from R_λ 1000 than that from R_λ 390, which is a plausible sign that an asymptotic state does exist at sufficiently high Reynolds number, even if that is not yet fully reached in this work. For the forward case the curves all converge with increasing Reynolds number onto the dashed line at height 0.55. The composite plateau at this height over all values of $\tilde{r}_0$ extends for about a decade, suggesting a robust scaling with Richardson constant about 0.55, which differs only marginally from the value 0.56 suggested in an earlier paper (Sawford *et al.* 2008). The scaling shown here is in fact likely to be more reliable, in part since it is observed over a wider time span at larger t/t_0 than before, and in part because the improved forcing used in the present simulations gives better stationarity in the turbulence (Donzis & Yeung 2010).

In the backward case, only for $r_0/\eta = 8$ is there a short plateau, but in all cases it is clear that the height of the peaks converges, and they become broader, with increasing Reynolds number. It is useful to note that for $\tilde{r}_0/\eta = 2$ and 4 (red and green lines) the peak value is still increasing with Reynolds number, while for $\tilde{r}_0/\eta = 8$ (blue line) it seems to have converged and for $\tilde{r}_0/\eta = 16$, it is even decreasing slightly by $R_\lambda = 1000$. It seems likely that at Reynolds numbers even higher than the present data the peak value of the red and green lines will increase further towards a plateau, while the black line will broaden and approach a plateau, below its peak value. This suggests the asymptotic value of the backward Richardson constant is close to the reference height of 1.5 drawn in the figure.

The extent of any plateau in plots like that in figure 4.3 is limited by the transition to diffusive behavior at large times $t \gg T_L$ and by the interference of the ballistic range at small times $t \ll t_0$. The latter effect can be reduced by studying relative dispersion in an inertial frame moving with the initial relative velocity between a pair of particles. We define the "differential separation" vector (Borgas & Sawford 1991; Yeung 1994)

$$\hat{\mathbf{r}}(t) = \mathbf{r}(t) - \mathbf{r}(0) - \mathbf{u}^{(r)}(0)t \ . \tag{4.5}$$

At small times the mean-square of $\hat{\mathbf{r}}(t)$ rises as t^4, and the statistics of $\hat{\mathbf{r}}(t)$ are determined by the Eulerian acceleration structure function evaluated at a spatial separation $\mathbf{r}(0)$ (Sawford *et al.* 2008). At times $t \gg t_0$ the statistics of $\hat{\mathbf{r}}(t)$ are expected to be close to those of $\mathbf{r}(t)$ as the effects of initial conditions gradually vanish. Accordingly, at times $t \gg t_0$ if Richardson scaling is well attained in $\langle r^2(t)\rangle$ at times $t \gg t_0$, the same behavior is also expected in $\langle \hat{r}^2(t)\rangle$ even though these quantities scale differently at small times. This expectation is tested in figure 4.4, which shows cubed-local-slope results obtained from the mean-square of the vector $\hat{\mathbf{r}}$, presented in a manner similar to figure 4.3. In general the CLS of $\hat{r}^2(t)$ begins at large values since $\langle \hat{r}^2(t)\rangle$ initially rises as t^4. Thus it would appear that we have replaced one potential source of interference (the ballistic range contribution to $\left\langle r^2 \right\rangle$) with another (the rapid early growth of $\langle \hat{r}^2(t)\rangle$). However we see that for $\tilde{r}_0/\eta = 4$ (green lines), the effect of the t^4 growth drops off quickly enough to permit an extended plateau, especially for the forward case, but also to a lesser extent for the backward case. The heights of these plateaus are consistent with those deduced from figure 4.3, and behavior at later times is also very similar as well. Thus the results in figures 4.3 and 4.4 are complementary and taken together provide strong support for the conclusion that forward and backward Richardson constants are close to $g_f = 0.55$ and $g_b = 1.5$ respectively.

The value of g_f deduced above is essentially the same as those found in other experimental and numerical work (Berg *et al.* 2006; Sawford *et al.* 2008; Bitane *et al.* 2012, 2013). Our estimate of $g_b = 1.5$ appears to be comparable to but slightly higher than estimates of 1.15 reported by both Berg *et al.* (2006) using particle-tracking velocimetry in experiments, and Bragg *et al.* (2016) using direct numerical simulations, as well as 1.35 by Eyink (2011) using DNS results on stochastic tracers with zero initial separation but finite molecular diffusivity. However, because of challenges in observing a well-defined backward Richardson scaling range, some modest variation in the value of g_b obtained from different datasets analyzed differently is not surprising.

4.3.2 Higher-order moments and non-Gaussianity of the separation

In the preceding subsection we only presented data from second-order moments, which in the case of pollutant plumes give a measure of the spread of the contaminant material in space. However, the occurrence of separation distances which are much larger than the average and contribute strongly to higher-order moments is also important. With increasing order the moments of the separation are increasingly dominated by the dissipation sub-range dynamics of the small scales. In figure 4.5 we show the normalized moments

$$M_n(t) = \langle r^n(t) \rangle / \langle r^2(t) \rangle^{n/2} \tag{4.6}$$

for orders $n = 3, 4$ for both forward and backward separation at $R_\lambda = 1000$. The small time limits (which persist for longer times if $\tilde{r}_0$ is larger) are determined by the distribution of initial separations shown in figure 3.1, while the large time limits correspond to independent Gaussian motions for the two particles in the diffusive regime. We see that for the smallest initial separation $\tilde{r}_0/\eta = 1$ shown there, both moments rise rapidly over a time less than 10 t_η to a peak and then decay only slowly towards the diffusive limit. This dissipation sub-range growth is so strong, that it influences the moments for larger initial separations where fewer, but still some, pairs are subject to dissipation sub-range dynamics. Thus, even at the highest Reynolds number for which we have data, these higher moments are dominated by dissipation sub-range dynamics over most times almost out to the diffusive regime. As a consequence, we are unable to observe any evidence of a Richardson scaling range, which for higher moments would be of the form

$$\langle r^n(t)\rangle = \langle\epsilon\rangle^{n/2} t^{3n/2} \qquad (t_0 \ll t \ll T_L) \ , \tag{4.7}$$

perhaps with intermittency corrections for $n \neq 2$, since in that case (4.7) is not linear in the dissipation rate.

The rapid growth in the moments of the separation is exponential in the limit $r_0/\eta \to 0$, where the separation vector behaves as an infinitesimal fluid element. The evolution of the separation is then governed by the simple equation (Batchelor 1952*b*; Berg *et al.* 2006; Borgas *et al.* 2004)

$$dr = rsdt \qquad (r \ll \eta) \tag{4.8}$$

where $s(t) = e_i s_{ij} e_j$ is the strain rate measured along the separation vector, $e_i = r_i/r$ is the unit vector in the direction of $\mathbf{r}(t)$, and the strain rates are evaluated along the trajectory of one of the pair of particles (which remain sufficiently close together for the local velocity gradients to be almost constant). The solution for $r^p(t)$ is

$$r^p = r_0^p \exp\left[p \int_0^t s(t')dt'\right] \qquad (r \ll \eta) \ , \tag{4.9}$$

Borgas *et al.* (2004) argued that at large time ($t \gg t_\eta$) $s(t)$ is in uncorrelated in time, so that, by the central limit theorem, $\int_0^t s(t')dt'$ would be a Gaussian random variable with mean $\overline{s}t$ and variance $\beta\sigma_s^2 t_\eta t$, where β is a constant of order unity. In fact this theory neglects extreme events and so the log-normal approximation for the statistics of r that follows from the central limit theorem is not exact (Falkovich *et al.* 2001). Nevertheless, it is interesting to see what this model predicts for the present DNS data.

For small times $t \lesssim t_\eta$, the correlation in $s(t)$ cannot be ignored. However if we suppose that $s(t) \approx s(0)$ up to a time αt_η where $\alpha = O(1)$, we can analyze the integral in (4.9) by splitting it into two parts, as $0 \to \alpha t_\eta$ and $\alpha t_\eta \to t$. This allows us to apply the central limit theorem analysis of Borgas *et al.* (2004), with the result

$$\langle r^p \rangle = b_p \langle r_0^p \rangle \exp\left[p\overline{s}\left(t - \alpha t_\eta\right) + \frac{p^2}{2}\beta\sigma_s^2 t_\eta \left(t - \alpha t_\eta\right)\right] \qquad \left(\langle r^p \rangle \ll \eta^p ; t \gg t_\eta\right) \tag{4.10}$$

where $b_p = \langle \exp\left(\alpha p s(0) t_\eta\right)\rangle$, and we recall that the average is taken over all pairs with initial separations in the bin centered on $\tilde{r}_0/\eta$. Thus for $t \gg t_\eta$ the effect of the small-time correlation in the strain rate can be approximated by a time offset in the exponential growth (Batchelor 1952*b*). That is, the correlation simply delays the onset of the exponential growth, which can be investigated numerically. Note that the dependence of the coefficient b_p on the order p means that the PDF is no longer exactly log-normal, and that the intercept of the exponential term at $t = 0$ varies with the order p.

Equation (4.10) can be analyzed further by noting that it needs to satisfy a requirement from incompressibility, namely (Zeldovich *et al.* 1984; Falkovich *et al.* 2001) $\left\langle r^{-3}\right\rangle$ be invariant for $\tilde{r}_0/\eta \to 0$ and $t \to \infty$. This requires that the argument of the exponential term in (4.10) must vanish for $p = -3$, giving the constraint

$$\beta\sigma_s^2 t_\eta = \frac{2}{3}\overline{s} \; . \tag{4.11}$$

Consequently (4.10) depends only on the Lagrangian time average of the strain-rate, $\overline{s}$

$$\langle r^p \rangle = b_p \langle r_0^p \rangle \exp\left[p\overline{s}\left(3 + p\right)\left(t - \alpha t_\eta\right)/3\right] \qquad \left(\langle r^p \rangle \ll \eta^p \; ; \; t \gg t_\eta\right) . \tag{4.12}$$

The non-dimensional moments can be written as

$$\frac{\langle r^p \rangle}{\langle r^2 \rangle^{p/2}} = c_p \frac{b_p}{b_2^{p/2}} \exp[\zeta_p (t/t_\eta - \alpha)] \qquad \left(\langle r^p \rangle \ll \eta^p \; ; \; t \gg t_\eta\right) , \tag{4.13}$$

where $\zeta_p = (p^2 - 2p)\overline{s}t_\eta/3$. The result is the same as for a log-normal PDF except for the prefactor $c_p b_p / b_2^{p/2}$, where $c_p = \langle r_0^p \rangle / \left\langle r_0^2 \right\rangle^{p/2}$, which is independent of $\tilde{r}_0$ for $\tilde{r}_0/\eta \to 0$. We emphasize that this result applies in the limit $\tilde{r}_0/\eta \to 0$ and we see that in this limit the exponential growth rate for the non-dimensional moments is independent of $\tilde{r}_0$.

Figure 4.6 shows the data from figure 4.5, re-plotted on linear-log axes, so an exponential growth appears as a straight line. Results at smaller values of $\tilde{r}_0/\eta$ are subject to increasing sampling noise and so are not plotted here, but we find that within sampling noise the results at $\tilde{r}_0/\eta = 1/2$ are essentially the same as those at $\tilde{r}_0/\eta = 1$ confirming that the moments converge as $\tilde{r}_0/\eta \to 0$, in accord with the theory. The exponential growth is truncated when particle separations move out of the dissipation sub-range and become increasingly influenced by inertial sub-range dynamics, but this truncation is delayed for increasingly longer times as $\tilde{r}_0/\eta \to 0$.

We have made estimates of the coefficients ζ_p by fitting the lagged exponential range for $r_0/\eta = 1$ empirically as shown by the straight lines in figure 4.6. The results are summarized in Table 4.2 for $R_\lambda = 390, 650$ and 1000. Although these are crude estimates, there is broad consistency in the results. The ratio of the exponents for the fourth order and the third order moments is close to the value 8/3 predicted by (4.13), suggesting that the central limit theorem is a reasonable approximation for moments of this order. In general the exponents increase with Reynolds number, although the backward exponents for $R_\lambda = 390$ seem anomalously high, as can be seen also from the ratio of the backward to forward exponents. For $R_\lambda = 650$ and 1000 this ratio, which is just the ratio of $\overline{s}$ for the backward case to that for the forward case since the factors in p cancel, is approximately 1.5. Since $\overline{s}$ is equal to the largest Lyapunov exponent λ_1 for the forward case (Falkovich *et al.* 2001) and the magnitude of the negative Lyapunov exponent $|\lambda_3|$ for the backward case (Berg *et al.* 2006), this ratio implies that the Lyapunov exponents are in the proportions $\lambda_1 : \lambda_2 : \lambda_3 = 1 : 0.5 : -1.5$, where as a result of incompressibility $\lambda_1 + \lambda_2 + \lambda_3 = 0$. The 50% difference between the backward and forward exponents is somewhat larger than other estimates (Berg *et al.* 2006) of about 20%.

4.3.3 Probability density function of the separation

More complete information beyond the moments of the separation distance is available in the separation PDF, i.e the PDF of $r(t)$ which evolves in time and is dependent on the initial separation. Because of our interest in scale similarity, we use the PDF of r/σ_r where $\sigma_r^2(t)$ is the time-dependent mean-squared separation. At small times the form of this PDF, denoted by $f(r/\sigma_r)$, is constrained by the manner in which particle pairs are initially positioned and sampled. In our case, $f(r/\sigma_r)$ is computed as a function of the initial separation $\tilde{r}_0$ in each bin. Based on figure 3.1, for bins with $\tilde{r_0} \leq \frac{1}{2}L_0$ the separation PDF at time $t = 0$ has the form $f(r) = Ar^2$ (where A is a constant) if r lies between $\frac{1}{2}\tilde{r_0}$ and $2\tilde{r_0}$ but $f(r) = 0$ otherwise. This is readily cast into the non-dimensional form $f(r/\sigma_{r_0})$ using the relation $\sigma_{r_0} = \langle r_0^2 \rangle^{1/2} = 1.5607\tilde{r_0}$ where as before $\langle\cdot\rangle$ denotes averaging in a bin. Accordingly, since $0.5/1.5607 \approx 0.32$ and $2/1.5607 \approx 1.28$ we can write

$$f(r/\sigma_{r_0}) = \begin{cases} 0 & r/\sigma_{r_0} \leq 0.32 \\ A(r/\sigma_{r_0})^2 & 0.32 \leq r/\sigma_{r_0} \leq 1.28 \ . \\ 0 & 1.28 \leq r/\sigma_{r_0} \end{cases} \tag{4.14}$$

On the other hand, in the large-time (diffusive) limit as the particles ultimately move independently of each other, $r(t)$ is expected to behave as the magnitude of a vector those three components are independent and identically-distributed Gaussian random variables. The PDF in the diffusive-limit can be written as

$$f(r/\sigma_r) = 3\sqrt{\frac{6}{\pi}}\left(\frac{r}{\sigma_r}\right)^2 \exp\left[-\frac{3}{2}\left(\frac{r}{\sigma_r}\right)^2\right] \ . \tag{4.15}$$

This limiting form of the PDF is only mildly non-Gaussian, with skewness factor 0.491 and flatness factor 3.099. Because of long-term memory effects in particle displacements the approach to this limit takes many Lagrangian integral time scales (Yeung 1994).

Another important limiting form of the separation PDF often investigated (Ott & Mann 2000; Ishihara & Kaneda 2002; Borgas & Yeung 2004; Sawford *et al.* 2013) is a result from Richardson's theory (Richardson 1926), in which the separation PDF satisfies a diffusion equation with scale dependent diffusivity $k(r) = k_0\langle\epsilon\rangle^{1/3}r^{4/3}$ (where k_0 is a non-dimensional coefficient) for separations in the inertial sub-range. This PDF can be written as

$$f(r/\sigma_r) = \alpha\left(\frac{r}{\sigma_r}\right)^2 \exp\left[-\beta\left(\frac{r}{\sigma_r}\right)^{2/3}\right] \ , \tag{4.16}$$

where the coefficients (Sawford *et al.* 2013)

$$\alpha = \left(\frac{1144}{81}\right)^{3/2}\left(\frac{2187}{560\sqrt{\pi}}\right) \ ; \quad \beta = \frac{9}{4}\left(\frac{1144}{81}\right)^{1/3} \tag{4.17}$$

ensure that the normalization condition $\int_0^\infty f(r/\sigma_r)\ d(r/\sigma_r) \equiv 1$ is satisfied and that (because σ_r^2 is the mean-square) $\int_0^\infty (r/\sigma_r)^2 f(r/\sigma_r)\ d(r/\sigma_r) \equiv 1$.

Richardson (1926) also defined the “distance neighbor function” (DNF)

$$q(r/\sigma_r) \equiv f(r/\sigma_r)/(r/\sigma_r)^2 \tag{4.18}$$

which compensates for the r^2 term in each of these PDFs and so takes a simpler form which is convenient for comparisons. Note in particular, that the DNF at $t = 0$ is simply a “top-hat” function which, from (4.14) is constant over the range $0.32 \leq r_0/\sigma_{r_0} \leq 1.28$. We also note that Richardson's constant (and the constant k_0 in Richardson's diffusivity) is involved only in the predicted scaling for σ_r^2 (hence σ_r), but not in the shape of the PDF of r/σ_r.

Figure 4.7 shows the time development of the distance-neighbor function at $R_\lambda = 1000$ and initial separations $\tilde{r}_0 = 4, 8, 16$ which provide conditions closest to that for Richardson's scaling to apply. The time instants are chosen to be in successive factors of 2, ranging from less than t_η to greater than 2 T_L. At the earliest time shown forward and backward DNFs agree closely, with the initial top-hat over the range $0.32 \leq r_0/\sigma_{r_0} \leq 1.28$ spreading to both smaller and larger values, particularly the latter. Subsequently, the DNFs spread towards the Richardson form at both small and large separations. Indeed, in the forward case for $\tilde{r}_0 = 4$ and the backward case for $\tilde{r}_0 = 4$ and 8 the DNFs spread beyond the Richardson form. Finally, at large times the DNFs obtained relax back towards, but, because of the finite time span of the simulations, do not reach the diffusive form.

In general, it can be seen that the tails of the backward DNF (as well as the PDF) extend wider than those in the forward cases. However for both forward and backward dispersion the PDFs show only transient agreement with the Richardson form, notably at $t/t_0 = 2.65$ and 5.31 for $\tilde{r}_0 = 8$ in the forward case, and at $t/t_0 = 1.67$ and 3.34 for $\tilde{r}_0 = 16$ in the backward case. These times are generally somewhat smaller, and the initial separations somewhat larger, than those for which the mean square displacement (according to figures 3 and 4) tends to show Richardson scaling. Consequently, in our view it is not clear whether the agreement with the Richardson form is significant or merely coincidental. It is possible that neither forward nor backward dispersion at intermediate scales behaves as a diffusion stochastic process as assumed by Richardson (1926). Indeed, a recent model (Bourgoin

2015) successfully treats relative dispersion as a cascade of scale-dependent ballistic motions rather than as a scale-dependent diffusion process.

4.4 Asymmetry in time

We have seen in the previous section that backward relative dispersion in both the dissipation sub-range and the Richardson range is faster than forward dispersion. In this Section we examine briefly the underlying mechanisms for this, with a focus on the small-time behavior which is more amenable to theoretical analysis. We also consider properties of the relative velocity, which governs the evolution of dispersion with time.

Recent work in the literature (Jucha *et al.* 2014) has shown that a more direct asymmetry occurs at small times, where the leading-order term in a Taylor series expansion in time has a change in sign going from forward to backward dispersion. In particular, if $\mathbf{u}^{(r)}(t) = \mathbf{u}^{(2)}(t) - \mathbf{u}^{(1)}(t)$ denotes the relative velocity of particles 2 and 1, and $\mathbf{a}^{(r)}(t) = \mathbf{a}^{(2)}(t) - \mathbf{a}^{(1)}(t)$ is the relative acceleration then the mean square relative velocity at small time can be written as

$$\langle \mathbf{u}^{(r)}(t) \cdot \mathbf{u}^{(r)}(t) \rangle = \langle \mathbf{u}^{(r)}(0) \cdot \mathbf{u}^{(r)}(0) \rangle + 2 \left\langle \mathbf{u}^{(r)}(0) \cdot \mathbf{a}^{(r)}(0) \right\rangle t + O(t^2) \ . \tag{4.19}$$

This relation implies that the two-point, one-time covariance between velocity and acceleration $\langle \mathbf{u}^{(r)}(0) \cdot \mathbf{a}^{(r)}(0) \rangle$ is of special significance.

Since we save particle velocities at time intervals much smaller than t_η, we are able to obtain the Lagrangian acceleration by a simple central difference of the Lagrangian velocity time series of each particle, and hence to obtain the term $\langle \mathbf{u}^{(r)}(0) \cdot \mathbf{a}^{(r)}(0) \rangle$. As before, we sample this quantity separately for pairs with their distances within a factor of 2 of a nominal $\tilde{r}_0$. However, since we calculate the acceleration as the velocity derivative for fluid particles, we need to account for the effect of the large-scale forcing. Using the Navier-Stokes equations at two points $\mathbf{x}(0)$ and $\mathbf{x}(0) + \mathbf{r}_0$, it can be shown readily that

$$\langle \mathbf{u}^{(r)}(0) \cdot \mathbf{a}^{(r)}(0) \rangle = -2\langle \epsilon \rangle - 2\nu \frac{\partial^2 \langle u_i' u_i \rangle}{\partial r_{0j} \partial r_{0j}} + \left\langle (f_i' - f_i)(u_i' - u_i) \right\rangle \ , \tag{4.20}$$

where $u_i = u_i(\mathbf{x}(0))$, $u_i' = u_i(\mathbf{x}(0) + \mathbf{r}(0))$ and $\mathbf{f}$ and $\mathbf{f'}$ represent the large-scale forcing at the points $\mathbf{x}(0)$ and $\mathbf{x}(0) + \mathbf{r}(0)$ respectively. For incompressible isotropic turbulence we can re-express the R.H.S in terms of the derivatives of the Eulerian longitudinal and transverse structure functions, in the form

$$\left\langle \mathbf{u}^{(r)}(0) \cdot \mathbf{a}^{(r)}(0) \right\rangle = -2\langle \epsilon \rangle + \nu \left\langle \frac{\partial^2 \left(D_{LL}(r_0) + 2D_{NN}(r_0) \right)}{\partial r_{0_j} \partial r_{0_j}} \right\rangle + \langle (f_i' - f_i)(u_i' - u_i) \rangle \ . \tag{4.21}$$

At small scales, where forcing is not present, by substituting Kolmogorov similarity forms for the structure functions in the dissipation range we can show that in the limit $\tilde{r}_0/\eta \to 0$ the Laplacian term becomes equal to $2\langle \epsilon \rangle$, so that the velocity-acceleration covariance also approaches zero, as required.

Figure 4.8 shows our results for the (relative) velocity-acceleration covariance at R_λ from 140 to 1000, in log-linear (left) and log-log scales (right). Because this covariance is a single-time statistic we have performed ensemble averaging over Lagrangian data at several well-separated time instants. At $\tilde{r}_0/\eta \ll 1$ the covariance becomes vanishingly small, as expected from the arguments above. With increasing separation, the Laplacian term in (4.21) becomes smaller, varying like $\left\langle (r_0/\eta)^{-4/3} \right\rangle \langle \epsilon \rangle$ for $\eta \ll \tilde{r}_0 \ll L$ and eventually vanishing for $\tilde{r}_0 \gg L$, and so at sufficiently large separation becomes negligible compared with $-2\langle \epsilon \rangle$. As a result the covariance is expected to approach $-2\langle \epsilon \rangle$ (Ott & Mann 2000; Xu *et al.* 2008; Pumir *et al.* 2001; Jucha *et al.* 2014) with increasing separation. This covariance is also equivalent to the initial time derivative of the mean-squared relative velocity, which has been confirmed in laboratory data (Xu *et al.* 2008) to be negative for all r_0. On the other hand, at large r_0 (of order L) the correlation between the forcing and the velocity is significant. Since the forcing causes the turbulence to be stationary, at large scales the relative velocity-acceleration covariance must vanish. This effect is clearly seen in figure 4.8, where the covariance peaks near $-2\langle \epsilon \rangle$ and then decreases with increasing separation. This fall-off occurs at smaller values of r_0/η as the Reynolds number increases. For comparison we have included Eulerian results for the normalized relative acceleration covariance at $R_\lambda = 140$ and 390. In Eulerian terms the acceleration is calculated as the sum of the pressure gradient and viscous terms, but without the forcing. Consequently there is no large scale fall-off and the covariance remains at $-2\langle \epsilon \rangle$ for $r_0/\eta > 100$, largely independent of Reynolds number.

Incidentally, the apparent collapse between data at different Reynolds numbers up to 10 η in figure 4.8 indicates small-scale universality. This behavior can be analyzed by expanding the Eulerian structure functions in (4.21) in a Taylor-series and keeping the next higher order beyond the usual quadratic contribution: namely

$$D_{LL}(r_0) = \left\langle \left(\frac{\partial u}{\partial x}\right)^2 \right\rangle {r_0}^2 - \frac{1}{12} \left\langle \left(\frac{\partial^2 u}{\partial x^2}\right)^2 \right\rangle {r_0}^4 + \dots \ . \tag{4.22}$$

Substitution of this and a similar result for $D_{NN}(r_0)$ into (4.21) gives

$$-\langle \mathbf{u}^{(r)}(0) \cdot \mathbf{a}^{(r)}(0) \rangle = \frac{\nu}{12} \left[\nu^2 \langle (\partial_{\|}^2 u)^2 + 2(\partial_{\perp}^2 u)^2 \rangle \right] \frac{\partial^2 r_0^4}{\partial r_{0j} \partial r_{0j}} \ . \tag{4.23}$$

where $\partial_{\|}^2 u$ and $\partial_{\perp}^2 u$ denote second derivatives taken in directions parallel and perpendicular to the velocity component concerned. Performing the required differentiations using the formula $\partial r / \partial r_j = r_j / r$ and normalizing using the Kolmogorov variables produces the result

$$\frac{-\langle \mathbf{u}^{(r)}(0) \cdot \mathbf{a}^{(r)}(0) \rangle}{2\langle \epsilon \rangle} = \frac{5}{6} \left[\frac{\nu^2 \langle (\partial_{\|}^2 u)^2 + 2(\partial_{\perp}^2 u)^2 \rangle}{\langle \epsilon \rangle^{3/2} \nu^{-1/2}} \right] \frac{\langle r_0^2 \rangle}{\eta^2} \ , \tag{4.24}$$

The bracketed term in (4.24), which we denote here as Λ, is an an Eulerian quantity related to the viscous contribution to the acceleration. Consider a coordinate component of the viscous acceleration, as

$$A_\alpha = \nu \nabla^2 u_\alpha = B_{\alpha\alpha} + B_{\alpha\beta} + B_{\alpha\gamma} \ , \tag{4.25}$$

where, e.g.. $B_{\alpha\beta} \equiv \nu \partial^2 u_\alpha / \partial x_\beta^2$ with α, β, γ being distinct subscripts (not summed). A simple squaring of both sides followed by use of isotropy gives

$$\langle A_\alpha^2 \rangle = \langle (B_{\alpha\alpha})^2 \rangle + 2\langle (B_{\alpha\beta})^2 \rangle + 4\langle B_{\alpha\alpha} B_{\alpha\beta} \rangle + 2\langle B_{\alpha\beta} B_{\alpha\gamma} \rangle \ , \tag{4.26}$$

Here the R.H.S contains four groups of terms. The sum of the first two gives the numerator in Λ. All of these terms can be written as integrals in Fourier space, e.g.

$$\langle (B_{\alpha\alpha})^2 \rangle = \nu^2 \iiint k_\alpha^4 \Phi_{\alpha\alpha}(\mathbf{k}) \, d\mathbf{k} \ , \tag{4.27}$$

where $\Phi_{ij}(\mathbf{k})$ is the energy spectrum tensor at the wavenumber vector $\mathbf{k}$. In incompressible isotropic turbulence the integral above can be evaluated by using the standard form

$$\Phi_{ij}(\mathbf{k}) = \frac{E(k)}{4\pi k^2} \left(\delta_{ij} - \frac{k_i k_j}{k^2} \right) \tag{4.28}$$

and a transformation to spherical coordinates in wavenumber space. The net result is that all terms in (4.27) are proportional to the integral $\int_0^\infty k^4 E(k)\ dk$: in particular

$$\langle (B_{\alpha\alpha})^2 \rangle = \frac{2}{35}\nu^2 \int_0^\infty k^4 E(k)\ dk\ ;\ \langle (B_{\alpha\beta})^2 \rangle = \frac{6}{35}\nu^2 \int_0^\infty k^4 E(k)\ dk\ . \tag{4.29}$$

Using these results and dividing by the denominator in Λ leads to

$$\Lambda = \frac{7}{2}\left(\frac{1}{15}\right)^{3/2} S_\epsilon = 0.06025\ S_\epsilon\ , \tag{4.30}$$

where $S_\epsilon = (4/35)(15\nu/\langle\epsilon\rangle)^{3/2}\int_0^\infty \nu k^4 E(k)\ dk$ is the dissipation skewness (Kerr 1985), which for locally isotropic turbulence at relatively high Reynolds number is close to the negative of the skewness of longitudinal velocity gradients (Batchelor 1953). Numerical values of Λ obtained from the DNS data are 0.031 and 0.034 at R_λ 140 and 390 respectively, which are consistent with values of S_ϵ reported previously (Yeung *et al.* 2006a). In the right frame of figure 4.8 excellent agreement with a slope 2 power law corresponding to these (close) values of Λ is indeed observed.

For relative dispersion the importance of the relative velocity-acceleration covariance examined above is that it appears in the Taylor series expansion for the mean square separation as the coefficient in a t^3 correction (Jucha *et al.* 2014; Ouellette *et al.* 2006) to the leading order ballistic term in (4.3). This correction term changes sign in the backward case, and so becomes the leading order term in the difference between backward and forward relative displacements, which can be written as

$$\left\langle |\mathbf{r}(-t) - \mathbf{r}_0|^2 \right\rangle - \left\langle |\mathbf{r}(t) - \mathbf{r}_0|^2 \right\rangle = -2\left\langle \mathbf{u}^{(r)}(0)\mathbf{a}^{(r)}(0) \right\rangle t^3 + O(t^5)\ . \tag{4.31}$$

We see from figure 4.8 that for $\eta \ll \tilde{r}_0 \ll L$ at large Reynolds number the term on the right simplifies to $-4\langle\epsilon\rangle t^3$. However, in subtracting between forward and backward relative displacement it is important to ensure that we are sampling the same "initial" conditions whether going forward or backward. This can be achieved by choosing an intermediate reference time, say $t = T/2$ in an original simulation spanning the period 0 to T, and then tracking the particle pairs both forward and backward for a shorter time interval ($T/2$).

Figure 4.9 shows the compensated difference between forward and backward dispersion,

$$\psi(t) = \left(\left\langle |\mathbf{r}(-t) - \mathbf{r}_0|^2 \right\rangle - \left\langle |\mathbf{r}(t) - \mathbf{r}_0|^2 \right\rangle \right) / \left(-\frac{1}{2}\left\langle \mathbf{u}^{(r)}(0)\mathbf{a}^{(r)}(0) \right\rangle t^3 \right)\ , \tag{4.32}$$

plotted as a function of t/t_0 over a range of initial separations for $R_\lambda = 140$ and 1000 in the left and center panels respectively, and for a range of Reynolds numbers for $\tilde{r}_0/\eta = 4$ and 8 in the right panel. The first two panels are similar in content to figure 1 of Jucha *et al.* (2014) but shows results at small to intermediate $\tilde{r}_0$ as well as (on the right) data at higher Reynolds number than other known data sources. At very early times especially for larger $\tilde{r}_0$ and higher Reynolds number there is a significant degree of numerical noise, which has been traced to the subtraction between extremely close numbers needed to extract t^3 behavior in both terms on the left of (4.31). To reduce this noise in the case of $R_\lambda = 1000$ we have averaged over three overlapping segments of reduced length $T/4$ instead of $T/2$ in the other cases. Nevertheless it is clear that (4.31) is well satisfied for both Reynolds numbers, with $\psi(t)$ showing a plateau at height 4.0 at early times for all values of $\tilde{r}_0/\eta$.

In the right panel of figure 4.9 the curves for $R_\lambda = 390, 650$ and 1000 converge for $t/t_0 \approx 10$ and approach a plateau at a height of about 1.9 as indicated by the dotted reference line. This corresponds to the Richardson regime with a plateau at height $(g_b - g_f)/(-\frac{1}{2}\left\langle \mathbf{u}^{(r)}(0)\mathbf{a}^{(r)}(0)\right\rangle/\langle\epsilon\rangle)$. Noting from figure 4.8 that $-\frac{1}{2}\left\langle \mathbf{u}^{(r)}(0)\mathbf{a}^{(r)}(0)\right\rangle/\langle\epsilon\rangle \approx 0.47$ for $\tilde{r}_0/\eta = 4$, this corresponds to $g_b - g_f \approx 0.9$, which is close to that implied by the estimates for $g_f = 0.55$ and $g_b = 1.5$ in Sec. 4.3.1. However, unlike figure 4.2, in figure 4.9 we do not see a tendency for curves with $\tilde{r}_0/\eta = 8$ to collapse to the same plateau because the normalizing factor $-\frac{1}{2}\left\langle \mathbf{u}^{(r)}(0)\mathbf{a}^{(r)}(0)\right\rangle$ is a strong function of $\tilde{r}_0/\eta$ at these separations.

The analysis of asymmetry between forward and backward dispersion at early times can also be extended to higher order moments. We first note that, to leading order, squaring the Taylor-series result $\mathbf{r}(t) - \mathbf{r}(0) = \mathbf{u}^{(r}(0)t + \frac{1}{2}\mathbf{a}^{(r)}t^2 + ...$ gives

$$(\Delta r)^2 = u_0^2 t^2 + u_0 A_0^{\|} t^3 + ... \,, \tag{4.33}$$

where we have introduced the shorthands $\Delta r = |\mathbf{r}(t) - \mathbf{r}(0)|$, $u_0 = |\mathbf{u}^{(r)}(0)|$, and $A_0^{\|} = \mathbf{u}^{(r)}(0) \cdot \mathbf{a}^{(r)}(0)/u_0$. Raising this expression to the power 1/2 gives

$$\Delta r = u_0 t + \frac{1}{2} A_0^{\|} t^2 + ... \,, \tag{4.34}$$

and hence, at any order p

$$\langle(\Delta r)^p\rangle = \langle u_0^p\rangle t^p + \frac{p}{2}\langle u_0^{p-1} A_0^{\|}\rangle t^{p+1} + ... \,. \tag{4.35}$$

Further use of power-series expansions eventually allows us to write the non-dimensional moments as

$$\frac{\langle(\Delta r)^p\rangle}{\langle(\Delta r)^2\rangle^{p/2}} = \frac{\langle u_0^p\rangle}{\langle u_0^2\rangle^{p/2}}\left[1+\frac{p}{2}\left(\frac{\langle u_0^{p-1}A_0^{\|}\rangle}{\langle u_0^p\rangle}-\frac{\langle u_0 A_0^{\|}\rangle}{\langle u_0^2\rangle}\right)t+....\right]\ . \tag{4.36}$$

Figure 4.10 shows data on the fourth-order non-dimensional moments of both forward and backward relative separation at $R_\lambda = 140$ and 1000. At small times the quantity on the ordinate is equivalent to the flatness factor of a velocity increment at scale size $\tilde{r}_0$, or of a velocity gradient if $\tilde{r}_0 \leq \eta$. As a result, because of intermittency in space, the normalized moments generally increase with the Reynolds number. According to (4.36) the correction to the leading order ballistic term is linear in time and so again changes sign in the backward case. This is clearly seen in the figure, where the trend away from the initial value is negative in the forward case (solid lines) but positive in the backward case (dashed lines). The asymmetry is not perfect however, presumably because the faster rate of separation in the backward case causes higher order corrections to affect the backward moment sooner.

The early-time asymmetry features studied here arise simply from the analytical nature of the dispersion statistics at small times. The existence of a non-trivial t^3 term in (4.31), through a non-zero correlation between the relative acceleration and velocity, depends on the non-linearity of the Navier-Stokes equations governing the Eulerian velocity field which determines the initial conditions. On the other hand, while the t^3 scaling in the Richardson range is not amenable to an analytical treatment it is also subject to the non-linear inertial sub-range dynamics. We believe however that there is no causal connection between the behavior of the relative displacement difference in (4.31) and that in the Richardson range, but rather that both are simply consequences of the non-linearity. For example, the early-time t^3 behavior is a transient response to the initial conditions which persists only for a time of order t_0 for inertial sub-range initial separations and for a time t_η for dissipation sub-range initial separations. Furthermore, although in the limit $r_0/\eta \to 0$ the acceleration-velocity covariance vanishes (see figure 4.8) so the early time t^3 regime also vanishes, at sufficiently large Reynolds number and sufficiently large time the Richardson t^3 range still exists (see figure 4.2). In fact, the limit $r_0 \to 0$ is singular for fluid particles since particles with $r_0 = 0$ never separate. Molecular diffusion regularizes this singular behavior. Indeed, for molecules which move under the joint action of the fluid velocity and a random Brownian motion (Pope 1998), we can set $r_0 = 0$, so the covariance and the early time t^3 regime both vanish completely. Despite this, the relative dispersion of pairs of molecules shows asymmetrical Richardson range scaling with different values for the backward and forward Richardson constants (Eyink 2011). Thus, the existence of Richardson scaling, and the asymmetry between the backward and forward versions, does not require a corresponding early time t^3 regime. In the cascading ballistic model of Bourgoin (2015) the early time t^3 regime is not necessary for the existence of a Richardson regime, but is necessary to ensure asymmetry between the backward and forward versions. This is probably because the cascade process continually resets the initial conditions.

4.5 Summary

In the study of turbulent mixing the trajectories of fluid particle pairs tracked backward in time are of great importance, but the type of data required is generally difficult to obtain and infrequently reported. In this work we have used direct numerical simulations of stationary isotropic turbulence to study both forward and backward dispersion, using an algorithm designed to sample efficiently the backward trajectories of a large number of fluid particles whose position and velocity have been saved from a forward simulation. Backward tracking is accomplished by post-processing of saved trajectories instead of performing an artificial backward simulation using Eulerian velocity fields saved at thousands of time steps which would lead to prohibitive storage requirements. We have developed a massively parallel implementation that has allowed us to obtain well-sampled forward and backward relative dispersion statistics at Taylor-scale Reynolds numbers 140 to 1000 over a range of initial separations ranging from Kolmogorov to energy-containing scales. Statistics are presented as functions of forward or backward initial separation, which are sorted into a number of bins centered around power-of-two multiples of the Kolmogorov scale. The number of particles tracked in each simulation is up to about 32 million and the total number of particle pairs counted is of the order 10^{12}.

A major focus of our work has been demonstration and quantification of Richardson t^3 scaling for the mean-squared separation in both forward and backward dispersion. This task has been carried out using data over a range of Reynolds numbers and initial separations, and a range of techniques, including plots compensated by inertial sub-range scaling, and so-called cubed-local-slope plots for both the relative dispersion and the mean-squared differential separation. In general backward dispersion is stronger than forward, especially at intermediate times, with faster dispersion also leading to an earlier approach to diffusive conditions. Richardson scaling for backward dispersion appears to require higher Reynolds number than for forward dispersion. Nevertheless, the Reynolds numbers in our simulations are sufficiently high for us to demonstrate the scaling in both cases, with forward and backward Richardson constants $g_f = 0.55$ and $g_b = 1.5$. The forward constant is consistent with, and the backward constant, a little larger than, previous estimates.

In contrast to quantities at the second moment level, Richardson scaling was not observed for higher order moments of the separation, because with increasing order the moments are increasingly influenced by dissipation sub-range effects, which persist almost to the large-time diffusive regime even for initial separations within the inertial sub-range. Our analysis of the separation PDF and the so-called distance-neighbor function showed only transitory agreement with the well-known Richardson prediction.

The strong exponential growth of the separation on dissipation sub-range scales was analyzed in terms of a central limit theory approximation which yields a log-normal distribution for the separations. A correction to this theory, which allows for early-time correlations in the strain-rate, explains the observed delay in the onset of exponential growth. The resulting predictions for the ratio of the growth rates of the third- and fourth-order moments are reasonably consistent with the theory. The backward growth rates, corresponding to the ratio of the magnitude of the smallest to largest Lyapunov exponents, are about 50% greater than the forward growth rates, somewhat higher than other estimates.

The asymmetry between backward and forward relative displacement in the ballistic small-time limit was analyzed theoretically and confirmed numerically. We showed that the key quantity in the Taylor series expansion for the mean square relative displacement, namely the covariance between the relative acceleration and the relative velocity, is non-zero and equal to $-2\langle\epsilon\rangle$ in the inertial sub-range at large Reynolds numbers. A rigorous analysis is also made of the small-scale universality of an Eulerian quantity that plays a central role. As a result of the behavior of the relative velocity-acceleration covariance, the difference in the backward and forward mean-square relative displacement has a t^3 dependence. Higher order moments of the relative displacement show a similar time asymmetry. We conclude however, that these asymmetries, and particularly the t^3 growth of this difference, are not simply connected to the t^3 growth in the Richardson regime and the asymmetry manifested there by the difference in the backward and forward Richardson constants.

The backward tracking approach developed and implemented in this work can be generalized readily to the case of pairs of molecules that undergo Brownian motion relative to the fluid (subject of next chapter), and to triangles and tetrads of fluid particles (subject of Chapter 6) which may become severely distorted fine-scaled turbulence at high Reynolds number. Improved understanding and accurate quantification of high Reynolds number behavior are expected to be of favorable impact in applications such as the dispersion of droplets in cloud physics (Chang *et al.* 2015).

Table 4.1: Parameters of the simulations performed: the Taylor-scale Reynolds number (R_λ) , number of grid points (N^3), the mean dissipation rate ($\langle\epsilon\rangle$), the kinematic viscosity (ν), the ratio of Lagrangian integral time scale (T_L) to Kolmogorov time scale (t_η), output time interval (h) in Kolmogorov scales, time span of simulation (T) in integral time scales, and the number of particles (N_p) tracked.

R_λ	140	240	390	650	1000
N^3	256^3	512^3	1024^3	2048^3	4096^3
$\langle\epsilon\rangle$	1.32	1.30	1.33	1.28	1.44
ν	2.8×10^{-3}	1.1×10^{-3}	4.370×10^{-4}	1.732×10^{-4}	6.873×10^{-5}
T_L/t_η	13.5	23.0	36.1	54.0	79.4
h/t_η	0.174	0.172	0.177	0.172	0.174
T/T_L	10.3	9.55	4.76	4.78	2.59
N_p	4,194,304	4,194,304	8,388,608	33,554,432	33,554,432

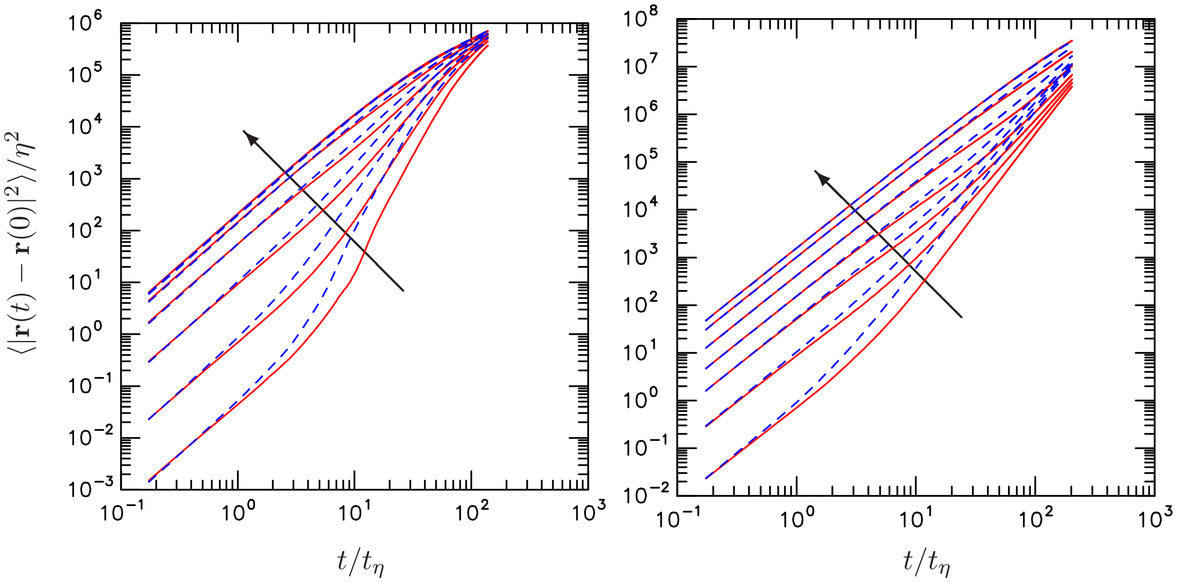

Figure 4.1: Mean-squared relative displacement as a function of forward time (solid lines, in red) and backward time (dashed lines, in blue) at R_λ 140 (left) and 1000 (right), scaled by Kolmogorov variables, for different initial separations. Arrows indicate direction of increasing $\tilde{r}_0$, in logarithmically-spaced intervals, $\tilde{r}_0/\eta = 1/4$, 1, 4, 16, 64, 256, 1024 for R_λ 140; $\tilde{r}_0/\eta = 1$, 4, 16, 64, 256, 1024, 4096 for R_λ 1000. (Results at $\tilde{r}_0/\eta = 1/4$ for R_λ 1000 are not shown since they are not well sampled.)

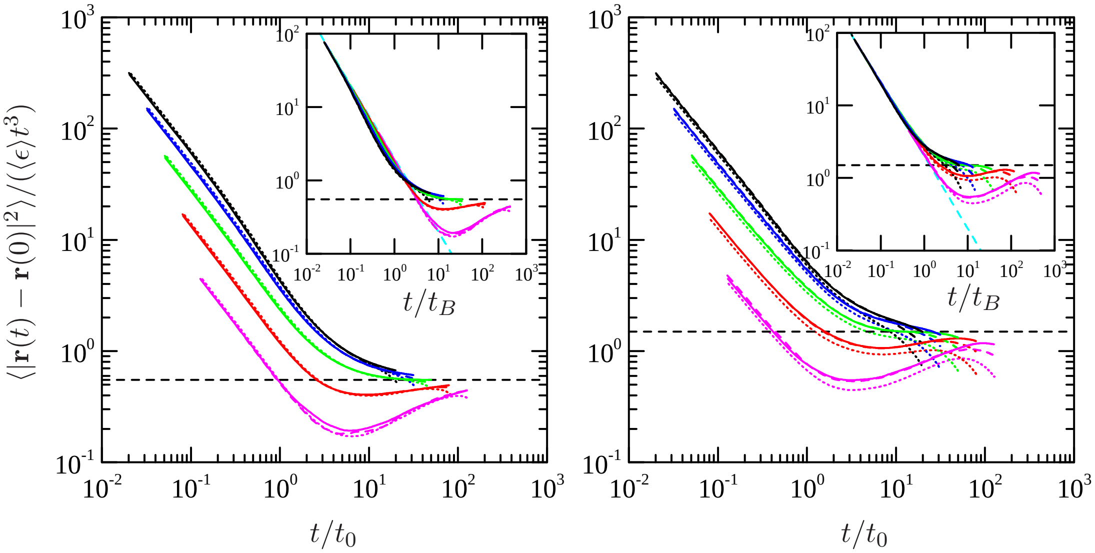

Figure 4.2: Compensated mean-square relative displacement in inertial sub-range scaling for a range of initial separations centered on $\tilde{r}_0/\eta = 1, 2, 4, 8, 16$ (increasing upwards, in magenta, red, green, blue, black) and Reynolds numbers $R_\lambda = 390, 650, 1000$ (dotted, dashed and solid lines respectively). Left panel shows forward dispersion; right panel shows backward dispersion. Horizontal dashed lines are at heights corresponding to estimates of forward and backward Richardson constants (0.55 and 1.5 respectively). Insets show the plots with time scaled by the Bitane time scale $t_B = S_2(\tilde{r}_0)/(2\langle\epsilon\rangle)$. The sloping cyan dashed line represents the quadratic ballistic term.

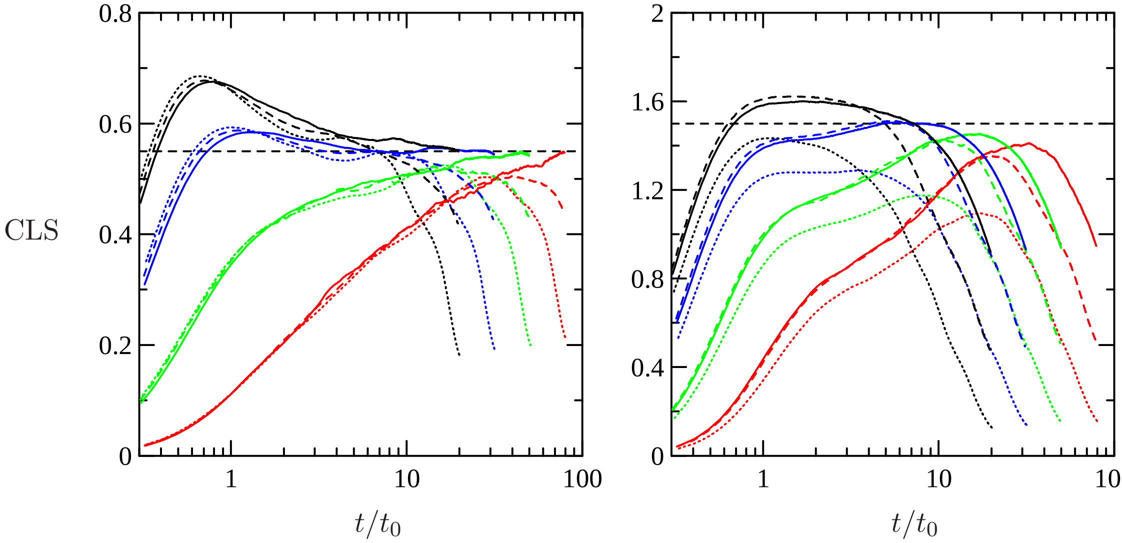

Figure 4.3: Forward (left) and backward (right) cubed-local slopes (defined by (5.36)) of mean-squared separation at different Reynolds numbers and initial separations. The data shown are at R_λ 390 (dotted lines), 650 (dashed lines) and 1000 (solid lines). Initial separations are (from bottom to top at small times) $\tilde{r}_0/\eta = 2$ (red), 4 (green), 8 (blue), 16 (black). Horizontal dotted lines drawn for reference are at the heights 0.55 (forward) and 1.5 (backward).

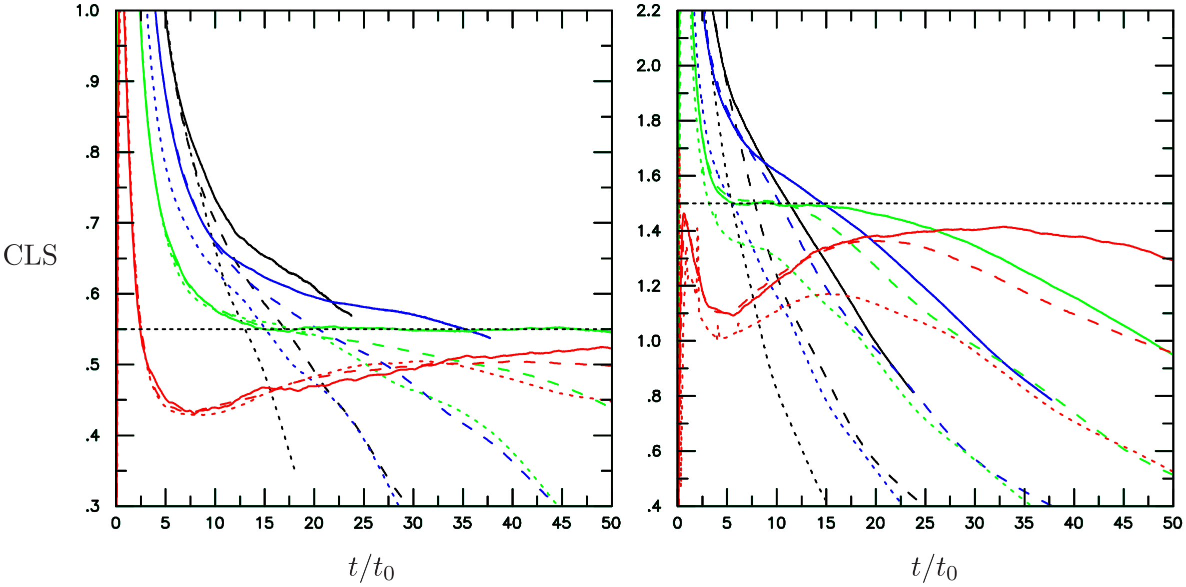

Figure 4.4: Cubed-local slopes obtained from the mean-squared differential separation, under the same conditions and labeled in the same manner as in figure 4.3. A linear scale on the time axis is used for better clarity in this figure.

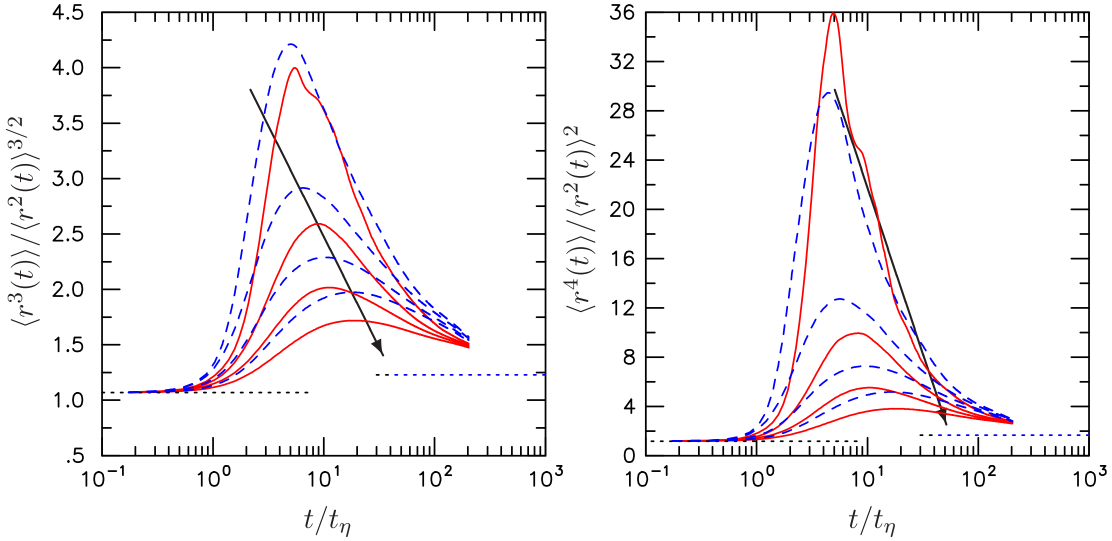

Figure 4.5: Normalized third order (left) and fourth-order (right) moments of forward (solid lines, in red) and backward (dashed lines, in blue) separation distance for initial separations $\tilde{r}_0/\eta = 1, 2, 4, 8$ (increasing in the direction of the arrows), at $R_\lambda = 1000$. Horizontal dotted lines indicate values at ballistic and diffusive limits: 1.0687 and 1.2284 respectively for third order, and 1.1741 and 1.6666 respectively for fourth order.

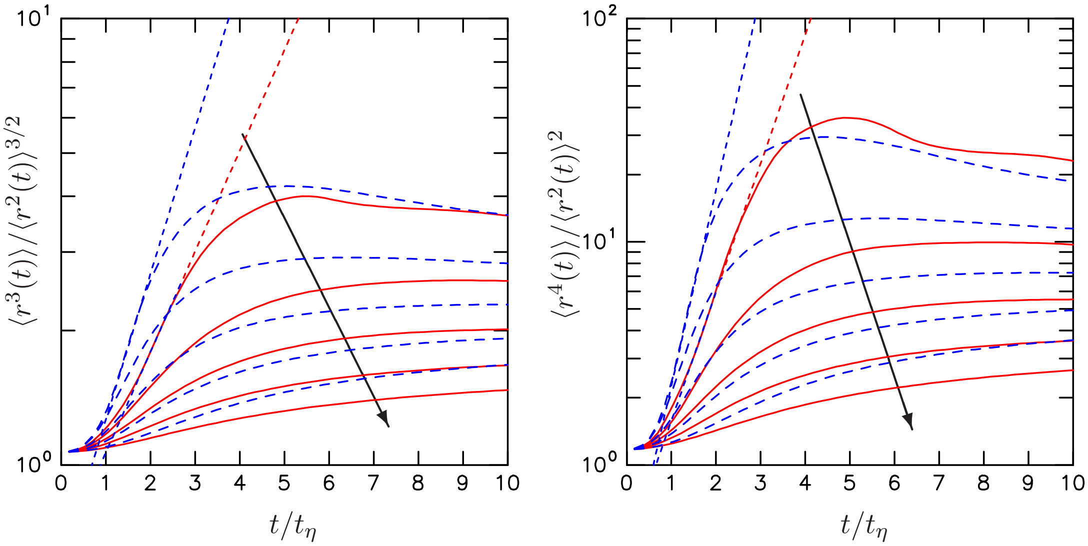

Figure 4.6: Linear-log plot to reveal exponential growth in third (left) and fourth (right) order moments of forward (solid red lines) and backward (broken blue lines) separation for $R_\lambda = 1000$; $\tilde{r}_0/\eta = 1, 2, 4, 8, 16$ (increasing in the direction of the arrows). The straight dotted lines (red for forward, blue for backward) are empirical fits to the exponential growth region.

Table 4.2: Exponential growth coefficients (in (4.13)) estimated from non-dimensional moments of the separation for $r_0/\eta = 1$ and for a range of Reynolds numbers. In the last two columns additional superscripts are used to distinguish between forward and backward values.

	Forward			Backward			Backward-to-Forward Ratios	
R_λ	ζ_3	ζ_4	ζ_4/ζ_3	ζ_3	ζ_4	ζ_4/ζ_3	ζ_3^b/ζ_3^f	ζ_4^b/ζ_4^f
390	0.127	0.368	2.89	0.244	0.703	2.88	1.92	1.91
650	0.139	0.395	2.85	0.229	0.576	2.52	1.65	1.46
1000	0.225	0.577	2.57	0.327	0.877	2.68	1.52	1.45

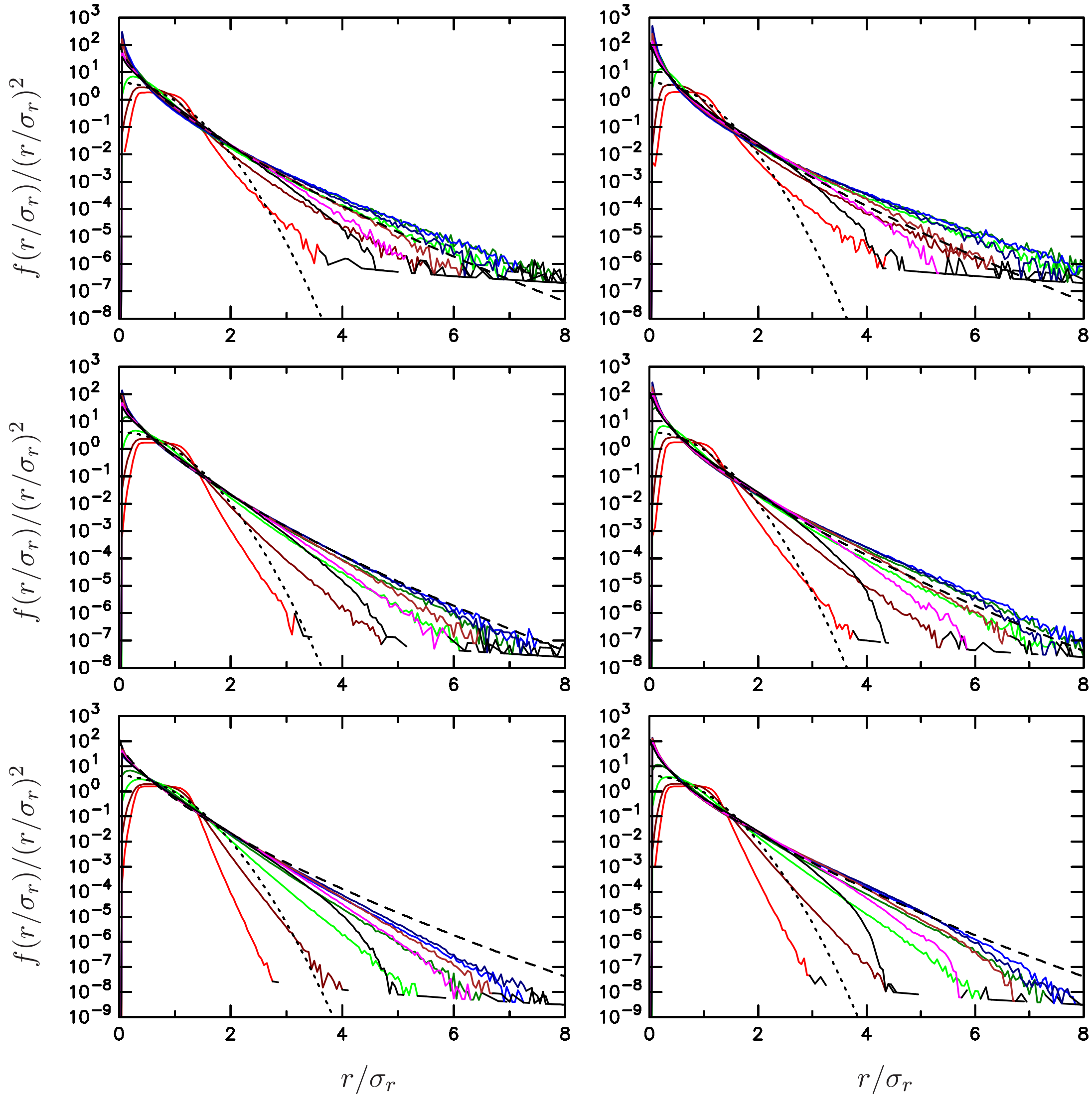

Figure 4.7: Richardson's distance-neighbor function for $\tilde{r}_0/\eta = 4$, 8 and 16 (top, middle and bottom panels respectively) at various times for forward (left panels) and backward (right panels) relative dispersion for $R_\lambda = 1000$. The colors sequence red, dark red, green, dark green, blue, dark blue, brown, magenta, black corresponds to t/t_0 values 0.264, 0.527, 1.05, 2.11, 4.22, 8.44, 16.9, 33.7, 61.6 ($\tilde{r}_0/\eta = 4$); 0.166, 0.332, 0.664, 1.33, 2.65, 5.31, 10.6, 21.2, 38.8 ($\tilde{r}_0/\eta = 8$); 0.105, 0.209, 0.418, 0.836,1.67, 3.34, 6.69, 13.8, 24.4 ($\tilde{r}_0/\eta = 16$). Dashed and dotted lines in black represent Richardson and diffusive limits respectively.

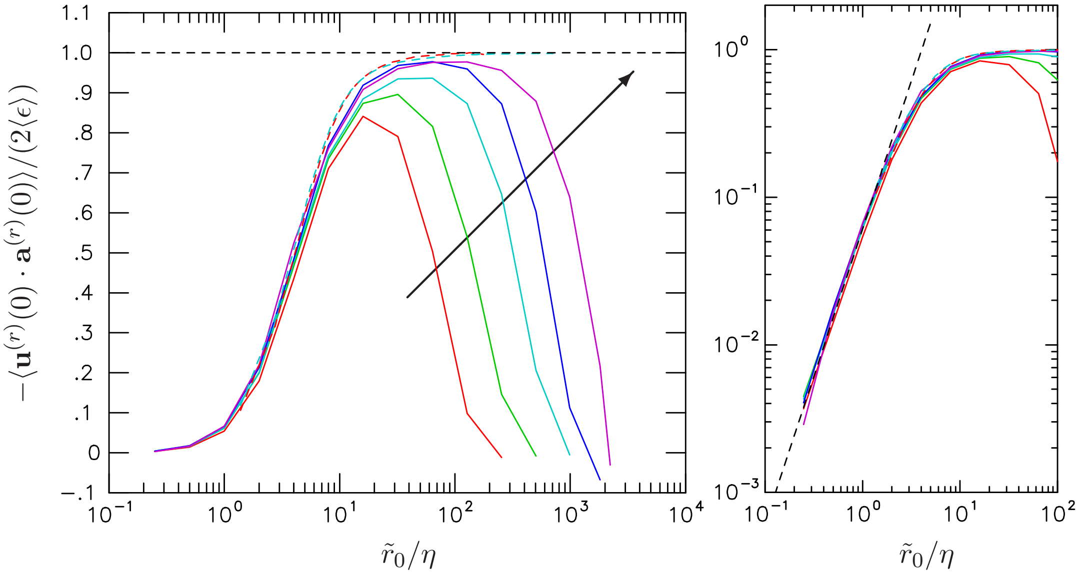

Figure 4.8: Normalized covariance between the two-point relative velocity and relative acceleration at time $t = 0$ at $R_\lambda = 140$, 240, 390, 650, 1000 (increasing in the direction of the arrow). Dashed curves in red and cyan (almost coincident but with the latter extending further) represent Eulerian results at $R_\lambda = 140$ and 390. The frame on the right shows the same data on log-log scales, compared with a slope 2 power law (dashed line) deduced from an analysis of higher-order terms.

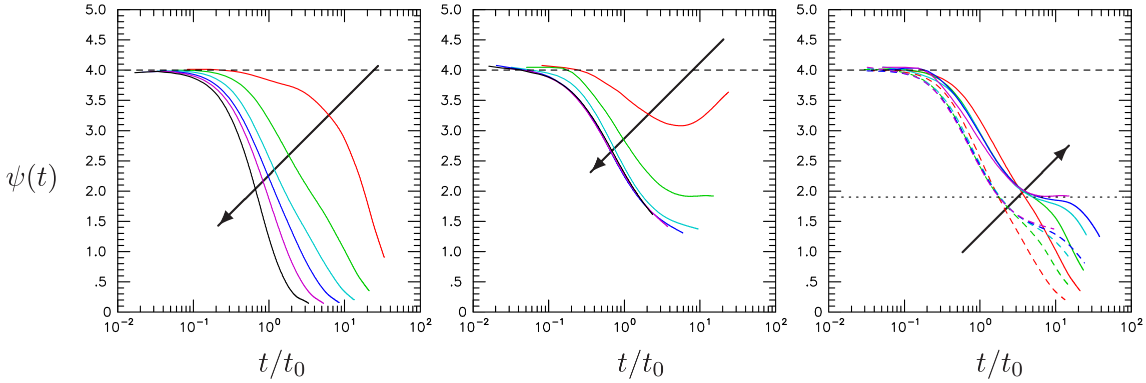

Figure 4.9: Compensated difference $\psi(t)$ between backward and forward relative displacement for $R_\lambda = 140$ (left panel) and 1000 (center panel), for $\tilde{r}_0/\eta = 2, 4, 8, 16, 32, 64$ (increasing in the direction of the arrow). The right panel shows $\psi(t)$ for $\tilde{r}_0/\eta = 4$ (solid lines) and $\tilde{r}_0/\eta = 8$ (dashed lines) for the 5 Reynolds numbers of this work (increasing from 140 to 1000 in the direction of the arrow) The horizontal dotted line is at a height 1.9.

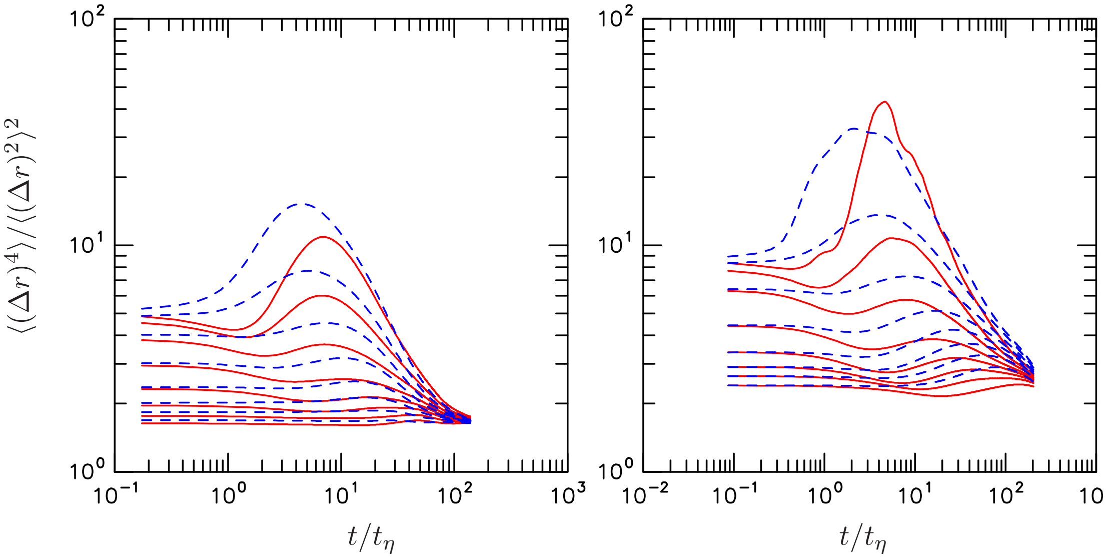

Figure 4.10: Normalized fourth-order moments for the relative displacement as a function of normalized time t/t_η, for $R_\lambda = 140$ (left panel) and 1000 (right panel), $\tilde{r}_0/\eta = 1$, 2, 4, 8, 16, 32, 64, 128 (increasing from top to bottom); showing both forward dispersion (solid lines, in red) and backward dispersion (dashed lines, in blue).

CHAPTER V

LAGRANGIAN STUDY OF TURBULENT MIXING: DISPERSION OF MOLECULAR TRAJECTORIES

5.1 Introduction

Although the motion of fluid particle captures the physics of turbulent dispersion well, in reality most transported substances undergo Brownian motion relative to the fluid at a rate set by their molecular diffusivity. Suppose if we consider two fluid particles at the same spatial location (hence zero relative velocity), they will never move apart and hence result in no mixing. Thus for mixing at small scales, we need to consider the motion of 'molecules' with a finite molecular diffusivity. If the scales of turbulent motions are much larger than the molecular time scales, the motion of molecules can be modeled by the stochastic differential equation (Pope 1998)

$$d\mathbf{x}^m(t) = \mathbf{u}\left(\mathbf{x}^m(t), t\right) dt + \sqrt{2\kappa}\, d\mathbf{W}(t) \quad , \tag{5.1}$$

where $\mathbf{x}^m(t)$ is the molecular position at time t, $\mathbf{u}(\mathbf{x}^m(t), t)$ is the instantaneous Eulerian velocity evaluated at $\mathbf{x}^m(t)$, and $\mathbf{W}(t)$ is a standardized three-dimensional (3D) isotropic Wiener process (Gardiner 1983). Although direct measurements are clearly difficult (more than for fluid particles), (5.1) provides a starting point for theoretical and numerical analyses. In particular, in direct numerical simulations (DNS) molecules can be tracked forwards in time as for fluid particles, with the Wiener process contribution implemented by drawing Gaussian random numbers at every time step. If a passive contaminant is released from a localized source, the subsequent displacement of molecules away from the source has a direct impact on the extent of spatial spreading achieved over a period of time. However, mixing also inherently involves how small parcels of contaminant material previously far apart and of different properties may be brought closely together. A close connection to the Eulerian framework is in fact made by studying backward trajectories, especially for pairs close together at a chosen time of reference (Thomson 1990; Sawford *et al.* 2005; Srinivasan

& Papavassiliou 2012) — efficient mixing would be indicated if there is a strong likelihood for such pairs to have come from locations far apart.

In this chapter we have two primary objectives. The first is to quantify and understand the properties of the trajectories of molecules taken singly and in pairs, in both forward and backward reference frames. Both high- and low-diffusivity regimes are considered, with the Schmidt number varied from 0.001 to 1000. We examine ballistic and diffusive behaviors at small and large times respectively, including comparisons with theoretical results given by Saffman (1960) where applicable. Because Brownian motion is not differentiable, a molecule does not have a well-defined velocity. However as Saffman (1960) showed, an integral time scale based on the fluid velocity along the molecular trajectories can be used to infer a turbulent diffusivity. In addition we are interested in any behavior at intermediate times that may resemble classical Richardson scaling (where mean-squared separation grows as t^3) for fluid particle pairs. Results are compared with those for fluid particle pairs (obtained in Chapter 4) and theoretical predictions for molecular pairs (Eyink 2011; Benveniste & Drivas 2014).

Our second objective is to establish and demonstrate, explicitly, a direct connection between molecular dispersion and passive scalar mixing at the same Schmidt number and Reynolds number. It is well known that the Schmidt number in applications can vary widely, and there are fundamental differences between weakly diffusive ($Sc \gg 1$) (Batchelor 1959) and highly diffusive ($Sc \ll 1$) (Batchelor *et al.* 1959) regimes. Both of these asymptotic regimes introduce difficulties for Eulerian investigations (Donzis *et al.* 2010; Yeung & Sreenivasan 2014). However, regardless of the value of Sc, in the Lagrangian framework, the covariance between scalar fluctuations separated by a distance r in space at a given time (t) is determined by the displacement statistics of two molecules that are at a distance r apart at time t (Durbin 1980; Borgas *et al.* 2004). For incompressible flow, either backwards or forwards formulations of these statistics can be used, but the backwards formulation is computationally more efficient and mathematically more tractable (Sawford *et al.* 2005). In the limit $r \to 0$ we recover the single-point scalar variance ($\langle \phi^2 \rangle$). A very appealing scenario for verifying this Eulerian-Lagrangian correspondence is the case of passive scalar fluctuations driven by a uniform mean gradient, which has received much attention in the Eulerian framework (Overholt & Pope 1996; Yeung *et al.* 2002; Watanabe & Gotoh 2006) especially for $Sc \lesssim 1$. In this case, there is a particularly simple connection between the backwards relative dispersion of a pair of particles and the scalar dissipation rate. This allows us to use backwards molecular trajectories to obtain precise information on processes contributing to net increase (i.e. production) or decrease (i.e. dissipation) of passive scalar fluctuations.

The postprocessing algorithm as discussed in § 3.3 is easily extended to molecules. As in § 5.4, we have obtained results at Taylor-scale Reynolds number from 140 to 1000. However, because molecular diffusion effects do become less pronounced at higher Reynolds number, we put a greater emphasis on results over a wide range of Schmidt numbers at moderate Reynolds numbers. Results at early times agree well with the exact theoretical results of Saffman (1960). At intermediate times evidence for Richardson scaling is stronger for molecules of $Sc \sim \mathcal{O}(1)$ than for fluid particles, but absent for molecules of $Sc \ll 1$ which are dominated by molecular diffusion. With sufficient care in the numerical procedures we find that our Lagrangian estimates of production and dissipation of scalar fluctuations, which are applicable at any Schmidt number, agree well with Eulerian results.

We first begin with a summary of the theoretical background underlying this work, with a focus on asymptotic limiting behaviors (including some results from Saffman (1960)) for statistics of molecules taken singly and in pairs. Their role in a Lagrangian description of turbulent mixing and its connection to the corresponding Eulerian formulation is also discussed. Several key aspects of the DNS numerical approach specific to molecules are noted. Then the results on one- and two-molecule statistics are presented, followed by the Lagrangian results for turbulent mixing based on molecular trajectories, which are shown to be in good agreement with Eulerian results on passive scalars driven by a uniform mean gradient.

5.2 Theory

In this section we present the theoretical background for our numerical results in this work, including the statistics of the displacement of single molecules (§5.2.1), the separation between pairs of molecules at specified initial separations in both forward and backward reference frames (§5.2.2), and the connection between Lagrangian and Eulerian results for passive scalar mixing (§5.2.3). For stationary turbulence we expect theoretical results derived by Saffman (1960) for one-molecule statistics to hold equally well for both forward and backward dispersion. However for pairs, it is important to make the distinction. It is well known that backward relative dispersion at intermediate times is stronger than forward (Sawford *et al.* 2005; Berg *et al.* 2006). There has been, in fact, considerable recent interest in backward dispersion of fluid particles (Jucha *et al.* 2014; Buaria *et al.* 2015) as well as theoretical work on molecular trajectories (Eyink 2011; Benveniste & Drivas 2014). However current knowledge of molecular path statistics especially in their Schmidt number dependence and connection to Eulerian passive scalar statistics is still limited.

5.2.1 Dispersion of single molecules

Saffman (1960) showed that the mean-square displacement of a single molecule consists of a diffusive Brownian motion contribution and a turbulence term based on the 'substance-autocorrelation' function (ρ_m), which is the fluid velocity autocorrelation along molecular trajectories. A tensor-form result assuming isotropy is

$$\langle Y_i^m Y_i^m \rangle(t) = \langle u_i u_i \rangle \int_0^t \int_0^t \rho_m(t', t'')\ dt'\ dt'' + 6\kappa t \quad , \tag{5.2}$$

where $Y_i^m(t) = x_i^m(t) - x_i^m(0)$ is the molecular displacement (we use superscript m to denote single-molecule quantities in contrast to $+$ for fluid particles.) If the turbulence is stationary and isotropic with r.m.s component velocity σ_u, then ρ_m is a function of time lag ($\tau = |t' - t''|$) alone and (5.2) becomes

$$\langle Y_i^m Y_i^m \rangle(t) = 6\sigma_u^2 \int_0^t (t-\tau)\rho_m(\tau) d\tau + 6\kappa t \ , \tag{5.3}$$

which can be compared with

$$\langle Y_i^+ Y_i^+ \rangle(t) = 6\sigma_u^2 \int_0^t (t-\tau)\rho_L(\tau) d\tau \ , \tag{5.4}$$

for fluid particles where $\rho_L(\tau)$ is the Lagrangian velocity autocorrelation. A term that represents interaction between molecular diffusion and turbulence can be defined as

$$\Delta(t) = \langle Y_i^m Y_i^m \rangle(t) - 6\kappa t - \langle Y_i^+ Y_i^+ \rangle(t) \ . \tag{5.5}$$

We address both small- and large-time limits. At small τ, Saffman used a Taylor series expansion to write the substance autocorrelation in the form

$$\rho_m(\tau) = \rho_L(\tau) - \frac{1}{3}\frac{\kappa\langle\omega_i\omega_i\rangle}{\sigma_u^2}|\tau| + \mathcal{O}(\tau^2) \ , \qquad \text{for } \ |\tau|/t_\eta \ll \min(1, Sc) \ , \tag{5.6}$$

where $\langle\omega_i\omega_i\rangle$ is the enstrophy, and t_η is the Kolmogorov time scale. The small time limit here is defined both by t_η and the time scale of molecular diffusion, Sct_η. Thus as Sc decreases, and molecular diffusion acts faster, the value of t required to observe this power law also becomes much smaller. The presence of a linear ($|\tau|$) term in (5.6) reflects the non-differentiable nature of the velocity at the molecular position. To non-dimensionalize the second term in (5.6) we use the relations $\langle\omega_i\omega_i\rangle = \langle\epsilon\rangle/\nu$ and $\langle\epsilon\rangle = 15\nu\sigma_u^2/\lambda^2$, where $\langle\epsilon\rangle$ is the mean dissipation rate and λ is the Taylor length scale, to obtain

$$\rho_m(\tau) = \rho_L(\tau) - \frac{\sqrt{15}}{3}\frac{1}{R_\lambda}\frac{1}{Sc}\frac{|\tau|}{t_\eta} + \mathcal{O}(\tau^2) \ , \qquad \text{for } \ |\tau|/t_\eta \ll \ \min(1, Sc) \ , \tag{5.7}$$

where $R_\lambda = \sigma_u\lambda/\nu$ is the Taylor-scale Reynolds number.

Substituting this in (5.3) and non-dimensionalizing by Kolmogorov variables leads to the following, up to $\mathcal{O}(t^3)$:

$$\frac{\langle Y_i^m Y_i^m \rangle(t)}{\eta^2} = \frac{6}{Sc}\frac{t}{t_\eta} + \frac{3R_\lambda}{\sqrt{15}}\left(\frac{t}{t_\eta}\right)^2 - \frac{1}{3Sc}\left(\frac{t}{t_\eta}\right)^3 \ , \tag{5.8}$$

where terms on the r.h.s represent the direct effect of molecular diffusion, fluid particle motion in the ballistic limit, and the interaction between turbulence and molecular diffusion. The diffusion term has the same form at any time t, while the t^2 ballistic term requires $|\tau|/t_\eta \ll 1$ and the t^3 interaction term requires $t/t_\eta \ll \min(1, Sc)$. It is apparent that, at any time t, the relative importance of different terms in (5.8) depends on both R_λ and Sc as well as t/t_η, while the interaction term itself (when written in Kolmogorov scaling) depends on Sc only, as:

$$\Delta(t)/\eta^2 = -\frac{1}{3Sc}(t/t_\eta)^3 + \mathcal{O}(t^4) \ . \tag{5.9}$$

At asymptotically large times, with a "molecular" integral time scale defined as $T_m = \int_0^\infty \rho_m(\tau)\ d\tau$, the mean-square displacement is expected to approach a diffusive regime of linear growth (Taylor 1921), i.e.

$$\langle Y_i^m Y_i^m \rangle(t) \approx 6\sigma_u^2 T_m t + 6\kappa t \ , \qquad \text{for} \ \ t \gg T_m \ . \tag{5.10}$$

With this and a similar result for $\langle Y_i^+ Y_i^+ \rangle$ in terms of the Lagrangian integral time scale (T_L), the interaction term in (5.5) becomes

$$\Delta(t) = 6\sigma_u^2 (T_m - T_L) t \ , \qquad \text{for} \ \ t \gg T_m, T_L \ \ . \tag{5.11}$$

Saffman (1960) also gave an approximate result for $\rho_m(\tau)$ at time lags $\tau \gg t_\eta$:

$$\rho_m(\tau) = \rho_L(\tau) - a\frac{\kappa\omega}{\sigma_u^2}\rho_L(\tau) \ , \tag{5.12}$$

where a is a proportionality constant, which Saffman (1960) estimated to be about 0.23. On substituting into (5.3), it can be shown that the interaction term then scales in the same way as $\langle Y_i^+ Y_i^+ \rangle$, such that for $t \gg t_\eta$, the ratio

$$\Delta/(\langle Y_i^+ Y_i^+ \rangle) \approx -a\sqrt{15} Sc^{-1} {R_\lambda}^{-1} \ \ , \tag{5.13}$$

becomes constant. Applying this relation for $t \gg (T_m, T_L)$ then (5.11) also gives

$$1 - T_m/T_L \approx a\sqrt{15} Sc^{-1} {R_\lambda}^{-1} \ , \tag{5.14}$$

which can be tested using the DNS data available in the present work.

5.2.2 Dispersion of molecular pairs

Consider two molecules at positions $\mathbf{x}^{m,1}(t)$ and $\mathbf{x}^{m,2}(t)$ respectively. Using (5.1), the separation vector $\mathbf{r}(t) = \mathbf{x}^{m,1}(t) - \mathbf{x}^{m,2}(t)$ evolves by

$$d\mathbf{r}(t) = \left[\mathbf{u}(\mathbf{x}^{m,1}, t) - \mathbf{u}(\mathbf{x}^{m,2}, t)\right] dt + \sqrt{4\kappa} d\mathbf{W}^{(r)} \ \ , \tag{5.15}$$

where $d\mathbf{W}^{(r)} = (d\mathbf{W}^{(1)} - d\mathbf{W}^{(2)})/\sqrt{2}$ is also a standardized incremental Wiener process (since the Brownian motion of each molecule is independent). The mean-square relative displacement for molecule pairs is given by

$$\langle |\mathbf{r}(t) - \mathbf{r}(0)|^2 \rangle = \int_0^t \int_0^t \langle \mathbf{u}^{(r)}(t') \cdot \mathbf{u}^{(r)}(t'') \rangle dt' dt'' + 12\kappa t \ \ , \tag{5.16}$$

where $\mathbf{u}^{(r)}(t)$ is the relative fluid velocity between molecular positions $\mathbf{x}^{m,1}(t)$ and $\mathbf{x}^{m,2}(t)$. Asymptotic behaviors at small, large and intermediate times are addressed below.

Unlike fluid particles, molecules can separate even if they happen to be coincident at a given time. For the case $\mathbf{r}(0) = \mathbf{0}$, and under the conditions $|\mathbf{r}(t)| = r(t) \ll \eta$ and $t \ll t_\eta$, Saffman (1960) obtained a small-time result which can be written as

$$\langle r^2(t) \rangle = 12\kappa t + \frac{4}{3}\kappa t^3/t_\eta^2 + \mathcal{O}(t^4) \ . \tag{5.17}$$

However, we are interested in a more general result that is also applicable to the small-time behavior of molecular pairs with small but finite initial separation. This requires a derivation based on Taylor series expansions in both time and space, which is presented in the Appendix A. Under the conditions $r(t) \ll \eta$ (and hence $|\mathbf{r}(0)| = r_0 \ll \eta$) and $t \ll t_\eta$, the result obtained, to $\mathcal{O}(t^3)$, can be written in Kolmogorov variables as

$$\frac{\left\langle |\mathbf{r}(t) - \mathbf{r}(0)|^2 \right\rangle}{\eta^2} = \left(\frac{r_0}{\eta}\right)^2 \left[\frac{1}{3}\left(\frac{t}{t_\eta}\right)^2 - \frac{7\ S_\epsilon}{18\sqrt{15}}\left(\frac{t}{t_\eta}\right)^3 \right] + \frac{12}{Sc}\left[\frac{|t|}{t_\eta} + \frac{1}{9}\left(\frac{|t|}{t_\eta}\right)^3 \right] , \tag{5.18}$$

where S_ϵ is the so-called dissipation skewness (Kerr 1985) which is directly related to the third moment of longitudinal velocity gradients. In (5.18) the first bracketed term represents the contribution from fluid particle dispersion, whereas the second bracketed term is essentially Saffman's result for coincident molecular pairs. It is clear that if $r_0 = 0$, we recover Saffman's result in (5.17), while for $Sc \to \infty$, we recover results for fluid particle pairs. This equation holds for forward relative dispersion. We have introduced the absolute value of the time in the Saffman term in (5.18) because for backward relative dispersion, which can be obtained by replacing t by $-t$, this term is unchanged (see Appendix A), whereas the sign of the fluid particle t^3 term in the first bracket changes (Jucha *et al.* 2014; Buaria *et al.* 2015). In general, under the specified conditions, the t^2 and t terms in both brackets will dominate compared to their respective t^3 counterparts. However the relative magnitude of the t^2 term in the first bracket, compared to both the t and t^3 terms in the second bracket depends strongly on r_0/η and Sc. For weak molecular diffusion ($Sc \gg 1$), we can find a range of time given by $Sc^{-1}(r_0/\eta)^{-2} \ll t/t_\eta \ll 1$, for which the t^2 term dominates over the t term (and hence also the t^3 term) in the second bracket. However for strong molecular diffusion, the linear t term will always dominate over the t^2 term, since $r_0 \ll \eta$.

Similarly, the Saffman t^3 interaction term in the second bracket dominates compared with the t^2 term for $(r_0/\eta)^2 \ll Sc^{-1}t/t_\eta$ and $t/t_\eta \ll \min(1, Sc)$. On the other hand, for any fixed r_0, the t^2 term dominates (over the t^3 term in the second bracket) for small enough time $t/t_\eta \ll Sc(r_0/\eta)^2$.

For arbitrary (not necessarily small) values of r_0 we can use (5.16) directly, to obtain, to leading order

$$\frac{\langle|\mathbf{r}(t)-\mathbf{r}(0)|^2\rangle}{\eta^2} = \frac{\langle D_{LL}(r_0)+2D_{NN}(r_0)\rangle}{\eta^2}\left(\frac{t}{t_\eta}\right)^2 + \frac{12}{Sc}\left(\frac{t}{t_\eta}\right) + \mathcal{O}(t^3) \quad , \tag{5.19}$$

where $D_{LL}(\cdot)$ and $D_{NN}(\cdot)$ are the Eulerian longitudinal and transverse structure functions respectively. The t^2 term on the r.h.s is the same as the fluid particle relative displacement at small times for any value of r_0 (Sawford *et al.* 2008). For $r_0 \ll \eta$, using a Taylor series expansion, this term gives the t^2 term in (5.18).

In the large-time limit, when the displacements of both molecules become independent of each other, the mean-square relative displacement becomes twice that of the displacement of a single molecule. Accordingly by (5.10), at times $t \gg T_m$, we obtain

$$\langle|\mathbf{r}(t)-\mathbf{r}(0)|^2\rangle \approx 12\sigma_u^2 T_m t + 12\kappa t \ . \tag{5.20}$$

In practice, because of memory effects in the displacement, the time needed to show clear agreement with (5.20) may be well over 10 integral time scales (Yeung 1994).

At intermediate times it is reasonable to look for an “inertial” scaling range where the mean-squared separation is independent of both the small-scale and large-scale motions, as well as the memory of initial separations. An extension of Richardson scaling for fluid particle pairs to molecules then suggests (Sawford & Pinton 2013)

$$\langle|\mathbf{r}(t)-\mathbf{r}(0)|^2\rangle = g_m\langle\epsilon\rangle t^3 \quad , \qquad \text{for } \max(t_\eta, t_0, t_\kappa) \ll t \ll T_m \tag{5.21}$$

where g_m is Richardson’s constant, $t_0 = (r_0^2/\langle\epsilon\rangle)^{1/3}$ is the Batchelor time scale which measures the memory of the initial separation (r_0) and $t_\kappa = (\kappa/\langle\epsilon\rangle)^{1/2}$ is the time scale of the interaction of molecular diffusion with inertial range eddies. Since backward dispersion is stronger than forward dispersion especially at intermediate times the Richardson constant for backward dispersion is larger than that for forward dispersion, as investigated in

Chapter 4 and also recently reported by Bragg *et al.* (2016); Buaria *et al.* (2015) of fluid particle pairs. At the same time, observation of Richardson scaling generally requires higher Reynolds number in the case of backward dispersion. For molecules an additional question is how the scaling depends on Schmidt number. One of our objectives in this work is to investigate Richardson scaling for both forward and backward molecular dispersion over a wider range of Reynolds and Schmidt numbers than have been reported by other authors (Eyink 2011; Eyink & Benveniste 2013; Benveniste & Drivas 2014).

5.2.3 Connections to Eulerian passive scalar mixing

In the Lagrangian theory of scalar mixing, the moments of the scalar concentration field can be expressed in terms of both the forward and backward displacement of marked molecules (Sawford & Pinton 2013). We decompose the instantaneous scalar field $\tilde{\phi}$ into the sum of the mean Φ and fluctuation ϕ. In general, the n^{th} order moment of $\widetilde{\phi}$ due to a source $S(\mathbf{x}, t)$, can be obtained in terms of backward displacements as

$$\begin{aligned} \langle \widetilde{\phi}^n(\mathbf{x}, t) \rangle = \int_{-\infty}^{t} ... \int_{-\infty}^{t} \int_V ... \int_V P(\mathbf{x}_1, t_1; ....; \mathbf{x}_n, t_n | \mathbf{x}, t) \\ S(\mathbf{x}_1, t_1)...S(\mathbf{x}_n, t_n) d\mathbf{x}_1 ....d\mathbf{x}_n dt_1 ...dt_n \quad , \end{aligned} \tag{5.22}$$

where $P(\mathbf{x}_1, t_1; ....; \mathbf{x}_n, t_n | \mathbf{x}, t)$ is the probability density function (PDF) for n molecules to be at positions $\mathbf{x}_1, ..., \mathbf{x}_n$ at earlier times $t_1, ..., t_n < t$ respectively, subject to the condition that they have all arrived at $\mathbf{x}$ at time t. This relation is exact and is the fundamental connection between the displacement statistics of molecular trajectories and scalar concentration statistics. The advantages of the backwards formulation are two-fold. Firstly, it is mathematically simpler in that the scalar moments are defined in terms of moments of the source function: by carrying out the integrations in space (5.22) also leads to

$$\langle \widetilde{\phi}^n(\mathbf{x}, t) \rangle = \int_{-\infty}^{t} ... \int_{-\infty}^{t} \left\langle S(\mathbf{x}^{m,1}(t_1))...S(\mathbf{x}^{m,n}(t_n)) \mid \mathbf{x}, t \right\rangle dt_1 ...dt_n \ . \tag{5.23}$$

Secondly, it is computationally more efficient since only trajectories ending at the measurement location $(\mathbf{x}, t)$ need to be sampled.

For the special case of an instantaneous uniform scalar gradient source in the x_1 direction $S(\mathbf{x}, t) = Gx_1\delta(t)$ in stationary isotropic turbulence, (5.22) can be simplified for $n = 2$ to obtain the scalar variance. Borgas *et al.* (2004) and Sawford *et al.* (2005) showed that

$$\begin{aligned}\langle\phi^2\rangle &= G^2\left\langle Y_1^{m,1}(0)Y_1^{m,2}(0)|r_0(t)\to 0\right\rangle \\ &= G^2\langle(Y_1^m)^2\rangle - \frac{1}{2}G^2\langle r_1^2(0)\ |r_0(t)\to 0\rangle \quad , \end{aligned} \tag{5.24}$$

where $\left\langle Y_1^{m,1}(0)Y_1^{m,2}(0)|r_0(t)\to 0\right\rangle$ is the conditional covariance of the x_1-component of the backward displacements at time zero of a pair of molecules labeled at time t, $\langle(Y_1^m)^2\rangle$ is the x_1-component of the one-particle dispersion over a time period t (equivalent for both backward and forward), and $\langle r_1^2\rangle$ is the x_1-component of the backward relative dispersion at time zero, such that at the final time t, the separation distance (r_0) between two molecules becomes zero. In isotropic turbulence it is also appropriate (and effective for improved sampling) to consider an ensemble average over gradient sources oriented along each of the three coordinate axes. It follows from (5.24) that

$$\langle\phi^2\rangle = \frac{1}{3}G^2\langle Y_i^m Y_i^m\rangle - \frac{1}{6}G^2\langle r_i r_i\rangle_{r_0(t)\to 0} \quad . \tag{5.25}$$

where we have simplified our notation for conditioning on $r_0(t)\to 0$. Substituting $\langle Y_i^m Y_i^m\rangle$ from (5.3) and differentiating with respect to t, it follows

$$\partial\langle\phi^2\rangle/\partial t = 2G^2\kappa_t + 2G^2\kappa - \frac{1}{6}G^2\frac{d}{dt}\langle r_i r_i\rangle_{r_0(t)\to 0} \quad , \tag{5.26}$$

where κ_t denotes $\sigma_u^2\int_0^t \rho_m(\tau)d\tau$ (from (5.3) using the Leibniz rule for integrals) which in the large time limit equals $\sigma_u^2 T_m$.

Equation (5.22) can be generalized to calculate joint velocity-scalar moments in terms of a similar integral over the joint velocity-displacement PDF. The result for the velocity-scalar covariance is (Sawford *et al.* 2005)

$$\langle u_i\phi\rangle = -G\kappa_t\delta_{i\alpha} \quad , \tag{5.27}$$

for a mean gradient G in the x_α direction. The gradient-transport nature of this relation suggests κ_t may be interpreted as the eddy diffusivity of the scalar fluctuations corresponding to the molecular motions.

Many Eulerian studies of turbulent mixing have considered a passive scalar field driven by a uniform mean gradient ($\nabla\Phi$), governed by the equation

$$\partial\phi/\partial t + \mathbf{u}\cdot\nabla\phi = -\mathbf{u}\cdot\nabla\Phi + \kappa\nabla^2\phi \ . \tag{5.28}$$

The scalar variance evolves by

$$\partial\langle\phi^2\rangle/\partial t = P - \chi \quad , \tag{5.29}$$

where $P = -2\langle\mathbf{u}\phi\rangle{\cdot}\nabla\Phi$ is the scalar production and $\chi = 2\kappa\langle\nabla\phi{\cdot}\nabla\phi\rangle$ is the scalar dissipation. Unlike in work focused on a stationary state, here we are interested in both production and dissipation as functions of time from $t = 0$ onwards. With the choice $\nabla\Phi = G\hat{e_1}$ (and averaging results for $\nabla\Phi$ along other coordinate directions) we obtain $P = 2G^2\kappa_t$ from (5.27), which is also the first term on the r.h.s. of in (5.26). Thus by comparing (5.26) with (5.29), we obtain

$$\chi(t) = \frac{1}{6}G^2\frac{d}{dt}\langle r_i r_i\rangle_{r_0(t)\to 0} - 2G^2\kappa \ . \tag{5.30}$$

It now follows from substitution into (5.29) and using (5.25) that

$$P(t) = \frac{1}{3}G^2\frac{d}{dt}\langle Y_i^m Y_i^m\rangle - 2G^2\kappa \ . \tag{5.31}$$

Thus we have exact results for the scalar production and dissipation in terms of the rate of change of the one- and two-molecule backward dispersion. In the current work, we first characterize the statistics of single molecules and pairs of molecules, comparing with Saffman's theoretical results wherever applicable. For molecular pairs, we are naturally more interested in backward statistics. Comparisons with Eulerian results are made primarily for $Sc \sim \mathcal{O}(1)$ because this is the range where detailed time history in the Eulerian frame is most readily available.

5.3 Numerical Approach and Database

We have performed simulations of stationary isotropic turbulence over a range of Reynolds numbers. Eulerian velocity and scalar fields are computed using a pseudo-spectral approach in space and second-order Runge Kutta integration in time as described in Chapter 2. Stationarity in the velocity field is achieved by maintaining (Donzis & Yeung 2010) the energy spectrum in the lowest few wavenumber shells at values suggested by long-time averages derived from previous simulations which used stochastic forcing (Eswaran & Pope 1988). For scalar fields the fluctuations are initially absent but subsequently generated by a uniform mean gradient. Although the forcing scheme employed tends to minimize temporal oscillations of the kinetic energy and dissipation rate, statistics in specific directions can still vary significantly at a given time instant. In order to minimize limitations in statistical sampling, for each value of Sc we simulate and subsequently average over results for three scalars with $\nabla\Phi$ in different coordinate directions.

Molecules are tracked by integrating (5.1), using an extension of a parallelized particle-tracking algorithm discussed in Chapter 3. To advance from time t_n to $t_{n+1} = t_n + \Delta t$ we calculate the predictor step estimate of the new position $\mathbf{x}^m(t_{n+1})$ by the formula

$$\mathbf{x}^{m,*} = \mathbf{x}^m(t_n) + \Delta t\ \mathbf{u}(\mathbf{x}^m(t_n), t_n) + \sqrt{2\kappa\Delta t}\ \mathbf{Z}\ , \tag{5.32}$$

where $\mathbf{Z}$ is a standardized Gaussian random variable in 3D, and the Wiener process increment is implemented as $d\mathbf{W} = \sqrt{\Delta t}\ \mathbf{Z}$. The end result, after the corrector step, is

$$\mathbf{x}^m(t_{n+1}) = \mathbf{x}^m(t_n) + \frac{1}{2}\Delta t\ [\mathbf{u}(\mathbf{x}^m(t_n), t_n) + \mathbf{u}(\mathbf{x}^{m,*}, t_{n+1})] + \sqrt{2\kappa\Delta t}\ \mathbf{Z}\ . \tag{5.33}$$

The fluid velocities at the two molecular positions shown in (5.33) are calculated by cubic-spline interpolation (Yeung & Pope 1988). This scheme is strong order 1/2 and weak order 1 (Kloeden & Platen 1992). However, in contrast to Eulerian simulations, no special numerical constraints arise for the time step or grid spacing at either very low or very high Schmidt number (Donzis *et al.* 2010; Yeung & Sreenivasan 2014), although having a substantial number of molecules is obviously important for statistical sampling. This approach is similar to the thermal marker technique of Papavassiliou & Hanratty (1995).

To obtain both forward and backward displacement statistics, we use our postprocessing approach described in Chapter 3. While single molecule statistics are relatively simple to obtain, two-molecule statistics require a careful approach in forming pairs of desired initial separation from the entire population. For a given trajectory extending from $t = 0$ to $t = T$, the initial separation for forward pairs is simply $r_0 = |\mathbf{r}(t = 0)|$, whereas for backward pairs the initial separation is defined as $r_0 = |\mathbf{r}(t' = 0)|$, where $t' = T - t$ is the backward time. Thus forward and backward statistics are compared using the properties of $\mathbf{r}(t)$ and $\mathbf{r}(t')$. However, since the turbulence is stationary, the statistics evaluated at any time t' are equivalent to those evaluated at time $-t$. Henceforth for convenience, we will use t to represent both forward and backward times, unless specified otherwise. Since pairs are formed from a population of many millions, samples of r_0 vary continuously over a wide range and are sorted into bins of finite width (see Chapter 3). This method allows us to compute the backward statistics without the need to store numerous time-resolved snapshots of the velocity field, which would be extremely memory-intensive, especially as the Reynolds number increases. Since final-time positions are not prescribed, we have no samples of initially coincident molecular pairs in the backward frame, and pairs of small r_0 are correspondingly fewer in number. However in most cases adequate sampling is achieved for pairs of initial separation down to as small as $\eta/4$, which as seen later in §5.6 is generally sufficiently small as an approximation to $r_0 \to 0$.

Table 5.1 gives a summary of the database used in the current work along with the main simulation parameters. In all cases the solution domain is of size $(2\pi)^3$, and the grid spacing is approximately twice the Kolmogorov length scale η. As mentioned earlier, the forcing scheme used (Donzis & Yeung 2010) tends to limit the variations in kinetic energy and mean dissipation rate, and thus both η and t_η can be taken as constant throughout each simulation. Most of the simulation parameters are the same as used in table 4.1 for fluid particles, except that the time span of both Eulerian and Lagrangian simulation at $R_\lambda = 650$ and 1000 is limited by computational expense. In the smaller simulations we have tracked molecules at several values of Schmidt number spanning many decades. For time-dependent Eulerian scalar fields we have limited ourselves to $Sc = 0.125$ and 1 (and only the latter in the more expensive 4096^3 simulation).

5.4 Single Molecule Statistics

Single-molecule statistics (where each molecule is an independent sample) provide a basic characterization of molecular trajectory properties and are also related to the production of scalar variance (§5.2.3). In this section we do not differentiate between forward and backward results, since in stationary turbulence these statistics are equivalent.

As suggested in §5.2.1, the first quantity to examine is the substance autocorrelation, $\rho_m(\tau)$, which by stationarity is an even function of the time lag (τ). Figure 5.1 shows (a) $\rho_m(\tau)$ for a range of Sc at given R_λ, and (b) data for a range of R_λ at given Sc, as a function of the time lag. The case $Sc = \infty$ corresponds to fluid particles. In (a), with R_λ held fixed at 140, as Sc decreases, we observe that the autocorrelation drops off to zero faster with time. This faster decorrelation at decreasing Sc is expected, because Brownian motion contributions to the displacements at successive time instants are independent and uncorrelated, and these contributions become stronger at higher molecular diffusivity. However the departure from the fluid particle case is substantial only for $Sc \ll 1$, showing that effects of molecular diffusion are weak compared to turbulence unless Sc is less than unity. The dependence on Sc is also expected to be weaker at higher R_λ.

It is well understood that since the velocity of a fluid particle is differentiable in time, the fluid particle velocity autocorrelation $\rho_L(\tau)$ has a parabolic decay near $\tau = 0$: i.e.,

$$\rho_L(\tau) \approx 1 - \frac{\tau^2}{\lambda_t^2} \ , \qquad \text{for} \ \ |\tau| \to 0 \ , \tag{5.34}$$

where λ_t is the Taylor time scale related to the acceleration variance σ_a^2 as $\sqrt{2}\sigma_u/\sigma_a$. By expressing σ_a in Kolmogorov variables and substituting this in (5.7) we obtain

$$\rho_m(\tau) = 1 - \frac{\sqrt{15}}{R_\lambda}\frac{a_0^2}{2}\left(\frac{\tau}{t_\eta}\right)^2 - \frac{\sqrt{15}}{3}\frac{1}{R_\lambda}\frac{1}{Sc}\frac{|\tau|}{t_\eta} \quad , \qquad \text{for} \ \ |\tau|/t_\eta \ll \min(1, Sc) \ , \tag{5.35}$$

where a_0 is the Kolmogorov-scaled acceleration variance (which is known to increase with Reynolds number as a result of intermittency (Yeung *et al.* 2006a)). The linear term in (5.35) will dominate if $\tau/t_\eta \ll a_0^2 Sc$, which is more easily satisfied at low R_λ and low Sc. To examine this behavior, in the inset in figure 5.1(a) we show $1-\rho_m$ versus τ/t_η on log-log scales. The approach to linear behavior, which would become more robust if the curves were extended to smaller time lags, is seen most readily for $Sc \ll 1$. For $Sc \gg 1$ there is a range of times $a_0^{-2}Sc^{-1} \ll t/t_\eta \ll 1$ over which the quadratic term in (5.35) dominates. Thus for $Sc > 1$, we can observe that the curves nearly overlap and display slope 2 at early time lags.

The effect of Reynolds number on Schmidt number dependence is seen in figure 5.1(b), which shows the substance autocorrelation for $Sc = 0.01$ and the fluid particle velocity autocorrelation (i.e. $Sc = \infty$). The difference between the two solid lines is substantial, showing that for fixed Sc the decorrelation with increasing time lag occurs more slowly when the Reynolds number increases. However, it is also clear at higher Reynolds number the difference between the solid and dashed blue (upper) lines is weak, which indicates sensitivity to Sc is much diminished as Reynolds number increases.

The areas under the curves in the two frames of figure 5.1 are (based on the normalization chosen) equal to the ratios T_m/t_η or T_m/T_L, respectively. These ratios are themselves related through the factor T_L/t_η, which increases with the Reynolds number. Table 5.2 shows the variation of T_m/T_L with Sc at R_λ up to 390. (At R_λ 650 and 1000 the simulation time T/T_L is too short to estimate T_m/T_L reliably.) It can be seen that T_m/T_L is relatively low for $Sc \ll 1$ and approaches unity as Sc increases. In addition, as Reynolds number increases, T_m/T_L at a given Sc becomes closer to unity. This is consistent with the fact that as the Reynolds number increases the influence of molecular diffusion also becomes very weak. However for finite Reynolds number, the effects of molecular diffusion must be taken into account, especially if Sc is low and R_λ is modest.

Figure 5.2 shows (a) the mean-square displacement, and (b) the magnitude of the interaction term (defined in (5.5)) , both normalized by Kolmogorov variables. As a result of molecular diffusion, the behavior of the mean-square displacement at small times, as given by (5.8), is very different depending on the Schmidt number. For sufficiently small times $t/t_\eta \ll Sc^{-1}R_\lambda^{-1}$ the linear diffusion term dominates, as is readily seen for $Sc < 1$ in part (a) of this figure, where Sc is varied over a wide range at fixed R_λ. For large Sc and/or large R_λ this linear growth is restricted to very small times and there is a range of times $Sc^{-1}R_\lambda^{-1} \ll t/t_\eta \ll 1$ over which the quadratic ballistic term dominates. This is readily seen in the collapse of curves for $Sc > 1$ onto the fluid particle result for $Sc = \infty$. At large times, all curves approach a diffusive regime where the growth of mean-square displacement is linear as given by (5.10). However the curve for $Sc = 0.001$ lies far above all the others, which is because in this case the diffusivity is so high that the second term in (5.10) dominates. By using $\sigma_u^2 T_m = \kappa_t$ as defined earlier, the mean-square displacement equals $6(\kappa_t + \kappa)t$, such that the slope in the large time limit is determined by the additive effect of the turbulent and molecular diffusivities. The Schmidt number dependence at other Reynolds numbers follows similar trends, but at higher R_λ generally a lower Sc is needed for molecular diffusion to be dominant.

A more sensitive test of Schmidt number effects is to plot the interaction term given by (5.5), which explicitly quantifies the effects of molecular diffusion on turbulence. In figure 5.2(b) it can be seen that, although there is some numerical noise resulting from taking differences between small values which are very close to each other, agreement with (5.10) is good for moderate and high Sc. However with decreasing Sc the DNS data fall increasingly below the theory. This is because, as noted before, (5.9) holds only at times $t/t_\eta \ll Sc$, which is not satisfied in the data range of figure 5.2(b).

On the other hand, at large times, the interaction term is given by (5.11), in which the relative magnitudes of the integral time scales T_m and T_L are important. In figure 5.3 we show data for $1-T_m/T_L$ versus Sc, which provides a test for the functional form suggested in (5.14), with each dashed line corresponding to a different value of the parameter a therein. At high Sc, or at moderate Sc at high R_λ, T_m becomes very close to T_L and the quantity $1 - T_m/T_L$ can become unreliable, or even spuriously negative, especially if T_m or T_L is affected by limitations such as the length of the simulation. As a result some data points corresponding to cases listed in table 5.2 are not shown in this figure where logarithmic scales are used. Nevertheless, good agreement with the Sc^{-1} dependence of Saffman's theoretical result is observed over a range of moderate Schmidt numbers, but with the parameter a dependent on Reynolds number. At very low Sc the discrepancy between theory and DNS is substantial, which is not surprising since physically both T_m and T_L must be non-negative with $T_m \leq T_L$, so $1 - T_m/T_L \leq 1$.

5.5 Statistics of molecule pairs

In this section, we present results for the forward and backward dispersion of molecular pairs. Since the turbulence is isotropic, dependence on the initial separation vector is through its magnitude (r_0) only. The statistics of molecule pairs are extracted using the same approach as fluid particle pairs, where samples of a continuous variation of r_0 are sorted into finite bins of logarithmic spacing. To enhance the sampling without sacrificing resolution in r_0, we choose overlapping bins within a factor of four, defined as $2^{i-3} \leq r_0/\eta \leq 2^{i-1}$ for $i = 0, 1, 2, 3, ...$ onwards. To identify a bin, we use $\tilde{r}_0/\eta$, which is the geometric mean between its lower and upper bounds, normalized by the Kolmogorov scale, i.e., $\tilde{r}_0/\eta = 2^{i-2}$ for $i = 0, 1, 2, 3, ...$ onwards. Consequently, all the pair statistics reported here are averages over the sample of initial separations in each bin and so are reported as functions of $\tilde{r}_0$ rather than random variable r_0. Earlier studies focused on fluid particles (Sawford *et al.* 2005; Berg *et al.* 2006) have shown that backward dispersion is similar to forward dispersion at both very short and very long times but stronger at intermediate times. More recently, it has been recognized that (Jucha *et al.* 2014; Buaria *et al.* 2015) forward and backward dispersion do differ at early but finite times — at a rate that grows as t^3, which could be overlooked if only the leading t^2 term in the Taylor-series expansions for both forward and backward mean-square relative displacement were retained.

An important question in this section is how molecular diffusion affects the behavior of mean-square relative displacement, $\langle|\mathbf{r}(t) - \mathbf{r}(0)|^2\rangle$. In view of the structure of (5.18–5.19), it is convenient to separate out the linear diffusive term which could become large at low Sc and obscure other effects of interest. Accordingly in figure 5.4 we show the evolution of the mean-square relative displacement compensated for the direct effect of molecular diffusion, i.e. $\left(\langle|\mathbf{r}(t) - \mathbf{r}(0)|^2\rangle - 12\kappa t\right)/\eta^2$, at three different Schmidt numbers with fixed $R_\lambda = 140$. On the scales of this figure forward and backward dispersion generally agree closely at both small and large times. At large times ($t \gg T_m$) curves for all values of $\tilde{r}_0$ are also seen to converge towards a linear diffusive limit, as given by (5.20). However, at very low Sc (0.01 or lower) where molecular diffusion is dominant, differences between forward and backward dispersion are small even at intermediate times. This is consistent with the results of Sawford *et al.* (2005) which showed that forward and backward dispersion are equivalent if the turbulence is Gaussian. As Sc decreases Brownian motion contributions (which are Gaussian) are more prominent. Approach to the large-time diffusive limit also occurs earlier for such small Sc since the ratio T_m/T_L (and hence T_m/t_η) decreases with decreasing Sc.

The nature of the behavior at early times in figure 5.4 is sensitive to both initial separation and Schmidt number. If $\tilde{r}_0$ is large then unless Sc is extremely small, the early-time growth is quadratic as explained by (5.19). Lines for large $\tilde{r}_0$ are also closer to each other since the Eulerian structure functions increase monotonically with $\tilde{r}_0$ until becoming constant at large $\tilde{r}_0$. However as discussed in relation to (5.18) if $\tilde{r}_0$ is small the early time behavior depends strongly on Sc, being cubic for $\tilde{r}_0^2/\eta^2 \ll Sc^{-1}t/t_\eta$ with $t/t_\eta \ll \min(1, Sc)$ and quadratic for $t/t_\eta \ll Sc(\tilde{r}_0/\eta)^2$. Thus in the data at $Sc = 0.01$, for $\tilde{r}_0/\eta \to 0$ we see a convergence to a stronger than quadratic dependence on time, but the times shown are too large for the Saffman t^3 behavior to be observed. For $Sc = 1$, data for $\tilde{r}_0/\eta = 1/4$ converge to the Saffman result for both forward and backward dispersion. Finally for $Sc = 100$ much smaller values of $\tilde{r}_0/\eta$ are needed to observe the Saffman result, and we see instead the ballistic t^2 behavior.

The most important dynamical issue at high Reynolds number is, of course, the possibility of Richardson scaling at intermediate times as defined by (5.21). An effective way to characterize the scaling behavior is to calculate the so-called cubed-local slope (CLS) (Sawford *et al.* 2008),

$$\frac{1}{\langle\epsilon\rangle}\left(\frac{d}{dt}\langle r^2\rangle^{1/3}\right)^3 . \tag{5.36}$$

If a well-defined Richardson scaling range is present, then the plot of the CLS versus t/t_0 will show a plateau at height equal to Richardson's constant, over a range of $\tilde{r}_0$ and in the range $(t_\eta, t_0, t_\kappa) \ll t \ll T_m$. In figure 5.5, we show data at the three highest Reynolds numbers for $Sc = 0.125$ and 1, for four values of $\tilde{r}_0/\eta$. In general there is clear evidence for Richardson scaling, at slightly different plateau heights, for all cases shown, while (as for fluid particles) the Richardson constant for backward dispersion is higher. For the forward case of $Sc = 0.125$, as R_λ increases, the plateau indicating Richardson scaling shifts down from 0.59 at $R_\lambda = 390$ to 0.56 at $R_\lambda = 650$ and $R_\lambda = 1000$. For $Sc = 1$, the data for $R_\lambda = 650$ and 1000 overlap almost perfectly with each other, indicating a very robust scaling with the Richardson constant being 0.55, a little lower than the value 0.56 for $Sc = 0.125$.

For backward dispersion, convergence towards Richardson scaling is not as strong as forward, especially at $Sc = 1$, but nevertheless still clearly evident. For $Sc = 0.125$, as R_λ increases from 390 to 1000, there is a clear trend with plateaus at 1.41, 1.55 and 1.57. For $Sc = 1$, the plateaus tend to be defined by the decreasing trends in the peak values with decreasing $\tilde{r}_0$, towards coincident values for $\tilde{r}_0/\eta = 2$ and 4, rather than as an extended plateau for any one value of $\tilde{r}_0$. These coincident values are 1.32, 1.50 and 1.53 for $R_\lambda = 390$, 650 and 1000 respectively.

While figure 5.5 shows the Reynolds number dependence at fixed Schmidt numbers, it is also useful to examine the Schmidt number dependence of the CLS at the highest available R_λ, including the case of $Sc = \infty$ (where we used fluid particle results given in Chapter 4. Figure 5.6 shows such data at $R_\lambda = 1000$ for $Sc = 0.125$, 1 and ∞. For forward dispersion (left frame), curves for $Sc = 1$ and ∞ essentially coincide at a plateau at height 0.55, a little lower than the plateau at 0.56 for $Sc = 0.125$. This suggests the Richardson's constant inferred here is well-converged with respect to Sc even if a weak decrease with Sc may still persist. For the backward case (right frame), dependence on Sc is more visible, with curves for $Sc = 0.125$ plateauing at 1.57, which is slightly above the value 1.53 for $Sc = 1$. For $Sc = \infty$, the trends with both $\tilde{r}_0/\eta$ and R_λ suggest a best estimate of 1.5 for the backward Richardson constant. This value corresponds to the short plateau for $\tilde{r}_0/\eta = 8$ in figure 5.6. This again suggests that an even higher R_λ is required to reach the asymptotic state for backward dispersion, at which the backward Richardson constant would also become independent of Sc.

A summary of our estimates for both forward and backward Richardson constants is given in Table 6.1. There are systematic trends with respect to both Schmidt number and Reynolds number and clear convergence with both increasing Sc at fixed R_λ and vice versa. The trends are also consistent with the work of Eyink (2011), who estimated the forward and backward constants to be 0.64 and 1.35 respectively using DNS results on stochastic tracers with zero initial separation for $Sc = 1$ at $R_\lambda = 433$; and that of Benveniste & Drivas (2014) who reported the backward constant to be 1.33 using the same database as Eyink (2011). Thus, the overall conclusion is that both Schmidt number and Reynolds number effects on the value of Richardson's constant (forward and backward) are weak, and that the values inferred here are consistent with those reported earlier for fluid particles (0.55 and 1.5 for forward and backward respectively, as shown in table 6.1 for $Sc = \infty$).

The general appearance of figures 5.5 and 5.6 bears several similarities to our analysis of Richardson scaling for fluid particles in Chapter 4. However, the scaling for molecules appears to be more robust. One possible explanation is that as a pair of molecules moves under the combined effects of turbulence and molecular diffusion, its memory of initial separation is lost faster than for fluid particles. If the Schmidt number is not too low, this effect may result in an early onset of a wider inertial range, with a wider plateau. While $Sc \sim \mathcal{O}(1)$, produces a more robust Richardson scaling, for $Sc \ll 1$ molecular diffusion may be so strong that the nature of dispersion becomes increasingly similar to pure Brownian motion, which deviates strongly from inertial range scaling. A complete absence of Richardson scaling is indeed found for our CLS data at $Sc = 0.01$ and 0.001 (not shown), although at higher Reynolds number this behavior would require increasingly lower Schmidt numbers.

The results of §5.4 and §5.5 have provided reliable information on one- and two-molecule statistics over a Reynolds and Schmidt number range considerably wider than previously reported in the literature. In the next section we use these results to address turbulent mixing in a Lagrangian frame.

5.6 Lagrangian Description of Scalar Mixing

In this section, we use the results for displacement statistics given in earlier sections to derive scalar field statistics from a Lagrangian perspective. Comparisons with Eulerian results are made only for $Sc = 0.125$ and 1 since higher or lower Sc require more computational resources. As derived earlier in §5.2, the scalar production and dissipation can be written in terms of displacement statistics for single molecules and pairs of molecules, as given by (5.31) and (5.30) respectively. However, both of these expressions involve numerical differentiation and subtraction between terms which may be very close to each other, especially for moderate and low Sc. To avoid numerical inaccuracies caused by these issues we derive alternative formulas in Appendix B. The formulas then we actually use to compute the scalar production and dissipation terms are

$$P(t) = \frac{2}{3} G^2 \langle Y_i^m(t) u_i \rangle \ , \tag{5.37}$$

$$\chi(t) = \frac{1}{3} G^2 \langle r_i(0) u_i^{(r)}(0) | \tilde{r}_0(t) \to 0 \rangle \ \ , \tag{5.38}$$

where u_i is the fluid velocity at the molecular position and $u_i^{(r)}$ is the relative fluid velocity between two molecules. In addition, stationarity allows us to replace (5.38) by

$$\chi(t) = \frac{1}{3}G^2\langle r_i(t')u_i^{(r)}(t')|\tilde{r}_0(T) \to 0\rangle \quad , \tag{5.39}$$

where $t' = T - t$ and conditioning on properties at the fixed final time (T) of the simulations is more readily implemented. However, as seen later, (5.31) and (5.30) are still useful from a theoretical perspective.

Figure 5.7 shows results for the scalar production normalized in the form $P/G^2\nu$, for $Sc = 1/8$ and 1, as the Reynolds number is varied from 140 to 1000. Excellent agreement is observed between Lagrangian results (calculated from (5.31) and (5.37)) and the Eulerian result (dotted black lines) $P = -2\langle \mathbf{u}\phi\rangle \cdot \nabla\Phi$ (§5.3), which is ensemble averaged over mean gradients aligned with each of the three coordinate axes. The normalization chosen allows the small-time results to be written wholly in terms of t/t_η, R_λ and Sc. In particular, for small times, substituting (5.8) in (5.31) gives the Lagrangian result as

$$\frac{P}{G^2\nu} = \frac{2R_\lambda}{\sqrt{15}}\frac{t}{t_\eta} - \frac{1}{3Sc}\left(\frac{t}{t_\eta}\right)^2 \quad , \tag{5.40}$$

which clearly supports a leading slope 1 behavior for $Sc = 1/8$ and 1 in the figure, with a direct dependence on R_λ which is also clearly seen. In the Eulerian frame, with $\phi = 0$ everywhere as initial conditions, at small times $\partial\phi/\partial t = -\mathbf{u}\cdot\nabla\Phi$ from (5.28), which implies the scalar fluctuations and hence production term grow linearly with time, at a rate consistent with (5.40).

At large times, a stationary state is expected as production and dissipation become balanced by each other (Overholt & Pope 1996). Substitution of (5.10) in (5.31) gives the Lagrangian result as

$$\frac{P}{G^2\nu} = 2\sigma_u^2 T_m/\nu \quad , \qquad \text{for} \ \ t \gg T_m \quad , \tag{5.41}$$

which becomes a constant, consistent with stationarity. Agreement between Lagrangian and Eulerian results is also verified by using (5.27) with $\sigma_u^2 T_m$ approaching κ_t. The time taken to reach a stationary state, if measured in t_η, is seen to be longer as the Reynolds number increases. This is expected, since approach to stationary state is determined by the large scale motions, whose time scale increases with respect to t_η as the Reynolds number increases.

As noted earlier (§5.2.3 and §5.5) statistics for pairs with zero backward initial separation are not available: i.e., the limiting condition $\tilde{r}_0(T) \to 0$ written above cannot be exactly attained. Thus we are interested in the quantity

$$\tilde{\chi}(\tilde{r}_0) = \frac{1}{6} G^2 \frac{d}{dt} \langle r_i(t) r_i(t) | \tilde{r}_0(T) \rangle - 2G^2 \kappa \ . \tag{5.42}$$

which effectively provides a Lagrangian estimate of χ based on results at a finite nonzero $\tilde{r}_0(T)$ approaching zero, but not exactly equal to zero. Figure 5.8 shows non-dimensionalized $\tilde{\chi}(\tilde{r}_0)$ for $\tilde{r}_0/\eta = 1/4$ to 4 at $Sc = 1$, along with corresponding Eulerian result, for R_λ ranging from 140 to 1000. It can be seen that as $\tilde{r}_0$ becomes smaller, $\tilde{\chi}(\tilde{r}_0)$ approaches the Eulerian result χ, with lines in red virtually coinciding with the black dashed lines. At large times all lines shown converge towards

$$\frac{\tilde{\chi}}{G^2 \nu} = 2\sigma_u^2 T_m / \nu \quad , \qquad \text{for} \quad t \gg T_m \quad , \tag{5.43}$$

which can be obtained by noting that the mean-squared relative displacement in (5.30) becomes twice the one-molecule mean-squared displacement used to obtain the scalar production term. To understand the convergence of results in the limit of $\tilde{r}_0 \to 0$ we can consider theoretical results on $\tilde{\chi}(\tilde{r}_0)$ at small times, If we consider pairs of very small separation only, i.e., $\tilde{r}_0 \ll \eta$, we can obtain the time derivative in (5.42) by differentiating (the backward version of, with a change in sign in the ballistic t^3 term) (5.18). The result, non-dimensionalized in the same manner as the production term, is

$$\frac{\tilde{\chi}(\tilde{r}_0)}{G^2 \nu} = \frac{\langle r_0^2 \rangle}{\eta^2} \left[\frac{1}{9} \left(\frac{t}{t_\eta} \right) + \frac{7}{36} \frac{S_\epsilon}{\sqrt{15}} \left(\frac{t}{t_\eta} \right)^2 \right] + \frac{2}{3Sc} \left(\frac{t}{t_\eta} \right)^2 \ . \tag{5.44}$$

where $\langle r_0^2 \rangle$ is the average over all initial separations in the bin centered on $\tilde{r}_0$. This expression has a strong dependence on $\tilde{r}_0$ which is (to leading order) linear in time, while the last term, scaling as t^2, is the true scalar dissipation in the limit of $\tilde{r}_0 \to 0$. A short dotted line of slope 2 drawn between t/t_η from 0.1 to 1 confirms excellent agreement with the data at small times in figure 5.8. For a given Sc and R_λ, the relative magnitude of first bracket can be controlled by choosing a sufficiently small r_0. In figure 5.8 it can be seen that, at small times, $\tilde{r}_0/\eta = 1/4$ is sufficiently small to obtain very close agreement with the Eulerian result (which becomes $(2/3Sc)(t/t_\eta)^2$).

As noted earlier, one advantage of the Lagrangian approach adopted here is that it is able to provide results on the statistics of scalar field when Sc is far from unity more easily than in the Eulerian frame. In figure 5.9 we show results for $\tilde{\chi}(\tilde{r}_0)$ for various $\tilde{r}_0$ at one very low value (0.01) and one very high value (100) of Sc, at the highest R_λ (390) for which we have such data available. Both are clearly quite distinct from the case of $Sc = 1$ at the same R_λ, which is already shown in the center panel of figure 5.8.

For $Sc = 0.01$, we can see that curves for all $\tilde{r}_0/\eta$ almost completely overlap, since molecular diffusion effects are so strong that the effect of $\tilde{r}_0$ is almost negligible. The discrepancy between the DNS data lines and the Saffman limit (which has slope 2 in this figure) is because the observation times t do not satisfy the condition $t/t_\eta \ll Sc = 0.01$. We see though that the results are trending towards the Saffman limit with decreasing time.

A substantial contrast for $Sc = 100$ is evident in frame (b) of figure 5.9, where the $\tilde{r}_0$ dependence is very strong. While the data at small times agree very well with (5.44), in this case well-sampled results for $\tilde{r}_0$ substantially smaller than $\eta/4$ are necessary to approximate the limiting case $\tilde{r}_0 \to 0$ well. This is a challenging requirement, since a substantial increase in the number of pairs of small separation can be achieved only by tracking a much larger population of molecules. The need for more samples will also grow with increasing Reynolds number, such that a satisfactory convergence to $\tilde{r}_0 \to 0$ at high Sc and high R_λ would be almost impossible to achieve in practice. However, $\tilde{\chi}(\tilde{r}_0/\eta = 1/4)$ provides a better estimate for the dissipation at larger times, and particularly for the stationary state, as the dependence on $\tilde{r}_0$ weakens and eventually vanishes.

In (5.41 and 5.43), it has been already noted that in the large time limit, both the production and dissipation approach $2\sigma_u^2 T_m/\nu$ under the normalization used above. A semi-empirical estimate of this dimensionless quantity can be made by writing it in terms of the Reynolds number and several time scales in turbulence, as

$$2\sigma_u^2 T_m/\nu = 2\frac{{R_\lambda}^2}{15}\frac{T_L}{T_E}\frac{T_m}{T_L} \quad , \tag{5.45}$$

where the Eulerian large-eddy timescale $T_E = \sigma_u^2/\langle\epsilon\rangle$, and for $R_\lambda \geq 140$ the ratio of the Lagrangian to Eulerian timescales is $T_L/T_E = 2/\tilde{C}_0$, with $\tilde{C}_0 \approx 6.5$ (Sawford *et al.* 2008). Thus we have the result

$$\frac{P}{G^2\nu} = \frac{\chi}{G^2\nu} \approx 0.041\ {R_\lambda}^2\ \frac{T_m}{T_L}\ , \tag{5.46}$$

where the ratio T_m/T_L has (as in table 5.2) a very weak dependence on Sc at large R_λ.

It is worth recapitulating that, to leading order and in the limit of vanishing backward initial separation, the rate of production of scalar fluctuations is initially independent of Sc according to (5.40) whereas the rate of dissipation is initially independent of Reynolds number according to (5.44). Figure 5.10 shows the evolution of both production and $\tilde{\chi}(\tilde{r}_0/\eta = 1/4)$, our Lagrangian approximation to the scalar dissipation, as they eventually approach the same large-time limit represented by (5.46) The behavior at small times is exactly as expected from (5.40) and (5.44) . At large times, for $R_\lambda = 140$, both scalar production and dissipation approach the same stationary state, although the curves for $Sc = 0.01$ are distinctively lower than that of $Sc \gtrsim 1$. However at $R_\lambda = 390$, we observe that all Sc cases nearly overlap at large times, since for the same Sc, T_m/T_L is closer to unity for $R_\lambda = 390$ compared to $R_\lambda = 140$. This observation that in the stationary state the scalar dissipation becomes independent of Sc with increasing R_λ, which in this case is derived from Lagrangian displacement statistics of molecules, is a manifestation of, and is consistent with and the same as the corresponding Eulerian understanding of the scalar dissipation anomaly (Donzis *et al.* 2005) and is evidence for so-called “spontaneous stochasticity” (Eyink 2011; Bernard *et al.* 1998). As a consequence, in the large Reynolds number limit fluid particles can be used in place of molecules to calculate scalar statistics on scales outside the dissipation sub-range.

Finally we examine the evolution of the non-dimensional scalar time scale, in the form of the ratio of the scalar field time scale, $\langle\phi^2\rangle/\langle\chi\rangle$ to the turbulence time scale $K/\langle\epsilon\rangle$, where $K = \frac{3}{2}\sigma_u^2$ is the turbulence kinetic energy. At small times, from (5.25) we have

$\langle\phi^2\rangle \approx \sigma_u^2 t^2 G^2$, while from (5.44) in the limit $\tilde{r}_0 \to 0$ we have $\langle\chi\rangle \approx \frac{2}{3} Sc^{-1}(t^2/t_\eta^2)G^2\nu$. This readily leads to

$$\frac{\langle\phi^2\rangle/\langle\chi\rangle}{K/\langle\epsilon\rangle} = Sc \ , \qquad \text{for} \ \ t \to 0 \ . \tag{5.47}$$

Data for the non-dimensional scalar time scale in the large-time stationary limit in DNS have been examined by Borgas *et al.* (2004) (for $Sc \geq 1$) and Donzis *et al.* (2005) (for $Sc \geq 1/8$). Both present semi-empirical results, based on integration of the scalar spectrum, describing the dependence of the timescale on Reynolds number and Schmidt number. For $Sc = 1$ the result given by Borgas *et al.* (2004) is simpler (and is found to fit the data slightly better). It is of the form

$$\frac{\langle\phi^2\rangle/\langle\chi\rangle}{K/\langle\epsilon\rangle} = a + bR_\lambda^{-1} \ , \tag{5.48}$$

where values $a = 0.41$ and $b = 4.33$ represent the DNS data well. Clearly (5.48) breaks down for $R_\lambda = 0$, but we are mostly interested in the large Reynolds number limit. For $Sc \gg 1$ both groups propose a correction logarithmic in Schmidt number, which arises from the Batchelor k^{-1} spectrum (Batchelor 1959), so that (5.48) becomes

$$\frac{\langle\phi^2\rangle/\langle\chi\rangle}{K/\langle\epsilon\rangle} = a + bR_\lambda^{-1} + \frac{5\sqrt{15}}{3} B_\phi R_\lambda^{-1} \ln Sc \ , \tag{5.49}$$

where $B_\phi \approx 5$ (Borgas *et al.* 2004; Donzis *et al.* 2010) is the Batchelor constant. For $Sc \ll 1$, Donzis *et al.* (2005) propose an inverse square-root correction, so in this case (5.48) becomes

$$\frac{\langle\phi^2\rangle/\langle\chi\rangle}{K/\langle\epsilon\rangle} = a + bR_\lambda^{-1} - cR_\lambda^{-1} Sc^{-1/2} \ . \tag{5.50}$$

Here we take $c = 1.25$. The data used in developing these semi-empirical relations were averaged over an extended time period of several eddy-turnover times in a stationary state, whereas the present data are time series subject to significant sampling variation, particularly at low Reynolds number. In order to smooth out these variations, we have fitted suitable functions, typically an exponential decay with a linear correction, to the data. These functions have been constrained to satisfy the small time limit (5.47) and the stationary limits (5.48) – (5.50). The left panel of figure 5.11 shows the result of such a fit to Eulerian time series for $Sc = 1/8$ and $Sc = 1$ at $R_\lambda = 140$. Given the variation, particularly at large times, the fitted functions are good representations of the data. The sampling variation decreases, and the fits improve, with increasing Reynolds number. The center panel shows the fitted functions for $R_\lambda = 140 - 650$. There are two points to note. Firstly, at small times, the timescale is directly proportional to Sc even in the large Reynolds number limit, so molecular diffusion can never be neglected. Secondly, in the stationary state for fixed Sc, the timescale becomes independent of Sc with increasing Reynolds number. This is again a manifestation of the scalar dissipation anomaly. These findings are confirmation of the small and large time predictions presented above. Finally, the third panel shows results as a function of Sc at $R_\lambda = 140$. In this case we show Lagrangian results for $\tilde{r}_0/\eta = 1/4$, which approximate the dissipation rate and hence the scalar timescale, since our Eulerian results do not cover a wide range of Sc. We see that at small times our results, shown as the dashed lines, deviate from the limit (5.47) because $\tilde{r}_0/\eta = 1/4$ is not small enough. Nevertheless, we have again been able to use suitable functional forms, shown as the solid lines, to fit our data and interpolate to the small-time limit. In this case of fixed Reynolds number, we see that with increasing Sc, the timescale stationary limit increases in agreement with the logarithmic dependence in (5.49). Thus in agreement with the theory developed in Borgas *et al.* (2004) and Donzis *et al.* (2005), our data show that the limit $\kappa \to 0$ is a singular. For $R_\lambda \to \infty$ at finite Sc the scalar dissipation and the scalar timescale are independent of molecular diffusion. On the other hand for $Sc \to \infty$ at finite R_λ, the scalar dissipation vanishes and the scalar timescale diverges.

5.7 Summary

Statistics of the trajectories of diffusing molecules undergoing Brownian motion relative to the fluid are important in a Lagrangian description of turbulent mixing, but not readily available in the literature. In this chapter, we have addressed several extensions to classical theory and have reported results on molecular dispersion at Schmidt numbers (Sc) ranging from 0.001 to 1000, in direct numerical simulations of stationary isotropic turbulence at Taylor-scaled Reynolds numbers (R_λ) 140 to 1000. Statistics of molecular pairs followed both forwards and backwards in time are obtained using a postprocessing approach which is adapted for massively parallel computation with a large sample of size (of order 10^{13} pairs). Our two main objectives are to understand how the statistics of molecules (singly and in pairs) at different temporal regimes depend on R_λ and Sc, and to relate these statistics to Eulerian results for a passive scalar driven by a uniform mean gradient (which, compared to the Lagrangian approach adopted here, are less readily obtained if $Sc \ll 1$ or $Sc \gg 1$).

As Saffman (1960) showed, the mean-squared displacement of a single molecule is the sum of a double integral of the autocorrelation of fluid velocity along the molecular trajectory (called the substance autocorrelation, $\rho_m(\tau)$) and a direct diffusion term which is linear in time. In general, as Sc decreases, $\rho_m(\tau)$ decreases more rapidly with time lag τ, resulting in a molecular integral time scale (T_m) which for any finite Sc is smaller than the Lagrangian velocity integral time scale (T_L). However this departure from fluid particle behavior, and correspondingly the effect of molecular diffusion on one-molecule statistics, is substantial only for $Sc \ll 1$, and also becomes weak at high R_λ with Sc fixed. Very good agreement is obtained with the theoretical predictions of Saffman (1960) except for scaling of T_m/T_L at low Sc.

For two-molecule statistics, we are able to extend a theoretical result of Saffman (1960) from the case of initially coincident pairs to pairs of finite initial separation. Excellent agreement is obtained between DNS and theory in the ballistic and diffusive limits. At intermediate times both forward and backward dispersion show clear signs of Richardson's t^3 scaling, with the backward Richardson constant being larger, as expected from the results on fluid particle pairs. As a result of the Brownian motion molecular pairs separate and lose memory of their initial separation faster, which appears to lead to more robust Richardson scaling for molecules compared to fluid particles. However if molecular diffusion is very strong (when Reynolds number is not large and Sc is very low), no scaling is observed. Our data suggest the forward and backward Richardson constants to be about 0.55 and 1.5 respectively for large Sc and large R_λ, which is in good agreement with the limited data in the literature. An observed weak dependence on Sc implies a Reynolds number higher than those in this work is required to reach the asymptotic behavior independent of Sc.

The connection between molecular displacements and passive scalar statistics in turbulent mixing is well known in theory but in practice rarely demonstrated explicitly. For the case of a scalar field generated by a uniform mean gradient we are able to relate numerical results on one and two-molecule statistics to Eulerian results which are more restricted in the range of Schmidt numbers accessible in DNS without much greater computational cost. The rate of production of scalar fluctuations inferred from one-molecule mean-squared displacement is seen to be in excellent agreement with Eulerian DNS results. The scalar dissipation requires the consideration of initially coincident backward trajectories of molecular pairs. However for $Sc \sim \mathcal{O}(1)$, pairs initially about 1/4 of a Kolmogorov length scale (η) apart appear to give adequate results. In the case of $Sc \ll 1$ a close correspondence is also possible but can be clearly observed only at smaller times than were recorded in our DNS. In the opposite limit of $Sc \gg 1$, a similar degree of agreement requires good sampling of backward pairs that are initially much closer than a distance of $\eta/4$ and correspondingly a much larger population of molecules tracked in the simulations.

Our results confirm that molecular diffusion cannot be neglected at small times where the scalar dissipation depends directly on Sc. At large times our results show that both the scalar dissipation rate and the scalar timescale become independent of Sc for fixed Sc in the large Reynolds number limit. This is a manifestation of the scalar dissipation anomaly (Donzis *et al.* 2005) and is evidence for so-called "spontaneous stochasticity" (Eyink 2011; Bernard *et al.* 1998). On the other hand, for fixed Reynolds number, in the limit of large Sc the scalar dissipation rate vanishes and the scalar timescale diverges. Thus, the limit $\kappa \to 0$ is singular. As a consequence of the scalar dissipation anomaly and spontaneous stochasticity, in the large Reynolds number limit fluid particles can be used in place of molecules to calculate scalar statistics on scales outside the dissipation sub-range.

In conclusion, we stress that the effects of molecular diffusion, which are often neglected in Lagrangian models of turbulent transport, have many interesting facets which may become prominent under a combination of conditions such as early times, small initial separations, and low Schmidt numbers. The analysis of molecular trajectories especially in a backwards-in-time reference frame as validated in this work can potentially provide useful answers for the mixing of a passive scalar at Schmidt numbers beyond those readily accessible in an Eulerian framework. We have focused on first and second moments. Higher-order moments require the study of multi-molecular clusters such as tetrads of various initial sizes and shapes.

Table 5.1: Parameters of the simulations performed: the Taylor-scale Reynolds number (R_λ) , number of grid points (N^3), the mean dissipation rate ($\langle\epsilon\rangle$), the kinematic viscosity (ν), the ratio of Lagrangian integral time scale (T_L) to Kolmogorov time scale (t_η), output time interval (h) in Kolmogorov scales, time span of simulation (T) in integral time scales, the number of molecules (P) tracked for each value of Schmidt number (Sc) and the values of Sc computed for each case in both the Lagrangian (Lag) and the Eulerian (Eul) part. $Sc = \infty$ corresponds to fluid particles.

R_λ	140	240	390	650	1000
N^3	256^3	512^3	1024^3	2048^3	4096^3
$\langle\epsilon\rangle$	1.32	1.27	1.27	1.42	1.44
ν	0.0028	0.0011	0.000437	0.0001732	0.00006873
T_L/t_η	13.5	23.0	36.1	54.0	79.4
h/t_η	0.174	0.172	0.177	0.172	0.174
T/T_L	10.3	9.55	4.76	1.94	1.86
P	4,194,304	4,194,304	16,777,216	33,554,432	50,331,648
Sc (Lag)	10^{-3}, 0.01, 0.125, 1, 8, 100, 10^3, ∞	10^{-3}, 0.125, 1, 8, 10^3, ∞	0.01, 0.125, 1, 100, ∞	0.125, 1, ∞	0.125, 1, ∞
Sc (Eul)	0.125, 1	0.125, 1	0.125, 1	0.125, 1	1

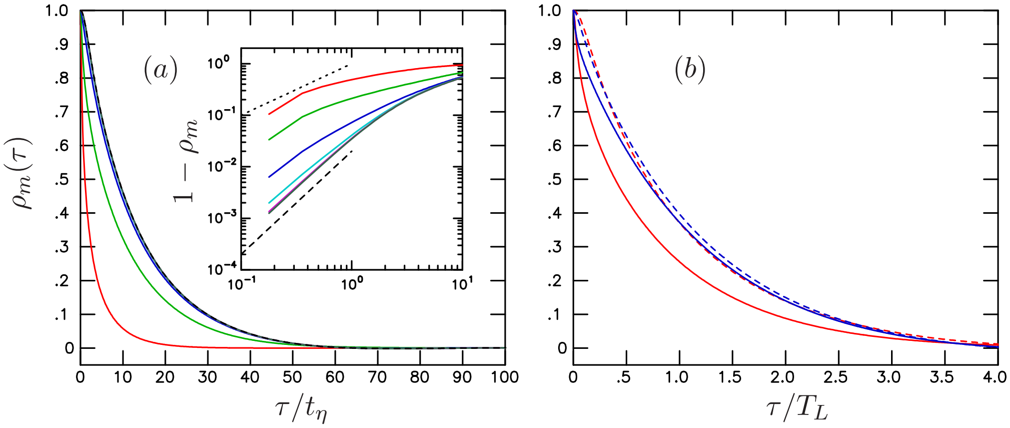

Figure 5.1: Substance auto-correlation, (a) as a function of non-dimensional time lag (τ/t_η) for $R_\lambda = 140$ and, bottom to top, for $Sc = 0.001$ (red), 0.01 (green), 0.125 (blue), 1 (cyan), 8 (magenta); data for $Sc = 100$ and 1000 are almost indistinguishable from $Sc = \infty$ (black). The inset shows $1 - \rho_m$ on log-log scales with Sc increasing downwards, with dotted and dashed lines, indicating slopes 1 and 2 respectively; (b) versus time lag scaled by T_L, for $Sc = 0.01$ (solid) and ∞ (dashed), at $R_\lambda = 140$ (red) (lower lines) and 390 (blue) (upper lines).

Table 5.2: Lagrangian integral time scale for molecular trajectories

R_λ/Sc	0.001	0.01	0.125	1	8	100	1000
140	0.2074	0.7199	0.9568	0.9921	0.9989	0.9997	0.9999
240	0.3770		0.9848	0.9974	0.9992		0.9999
390		0.9408	0.9943	0.9992		1.000	

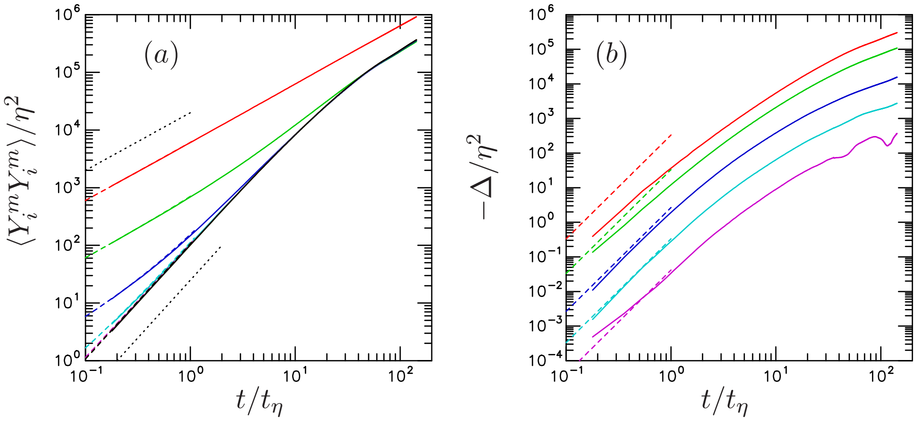

Figure 5.2: (*a*) Single molecule Kolmogorov-scaled mean-square displacement at $R_\lambda = 140$, for $Sc = 0.001$ (red), 0.01 (green), 0.125 (blue), 1 (cyan), 8 (magenta), 100 (orange) and 1000 (black) increasing from top to bottom (the last three cases being virtually indistinguishable). Dashed color lines are corresponding small time results given by (5.8). Dotted black lines are for slopes 1 and 2. (*b*) Negative of interaction term given by (5.5), scaled by Kolmogorov variables, for $R_\lambda = 140$ and $Sc = 0.001$, 0.01, 0.125, 1 and 8 (same colors as in (*a*)), increasing from top to bottom. Dashed color lines represent Saffman's small-time results given by (5.9).

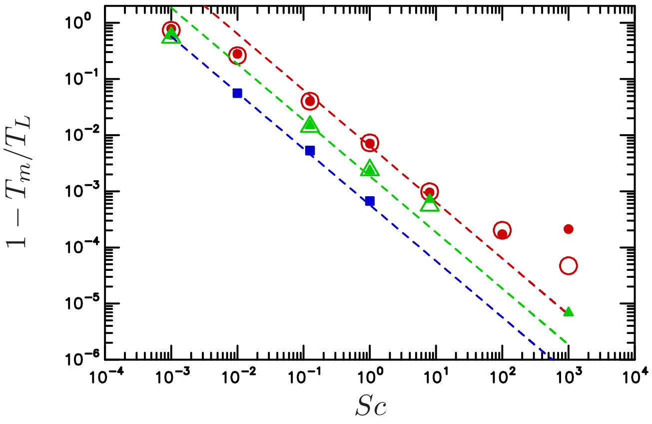

Figure 5.3: Variation of molecular integral time scale with respect to Lagrangian time scale as a function of Sc for $R_\lambda = 140$ (circle, in red), 240 (triangle, in green) and 390 (square, in blue). Open and closed symbols represent estimates based on the substance autocorrelation and the interaction term respectively. Dashed lines at slope -1.

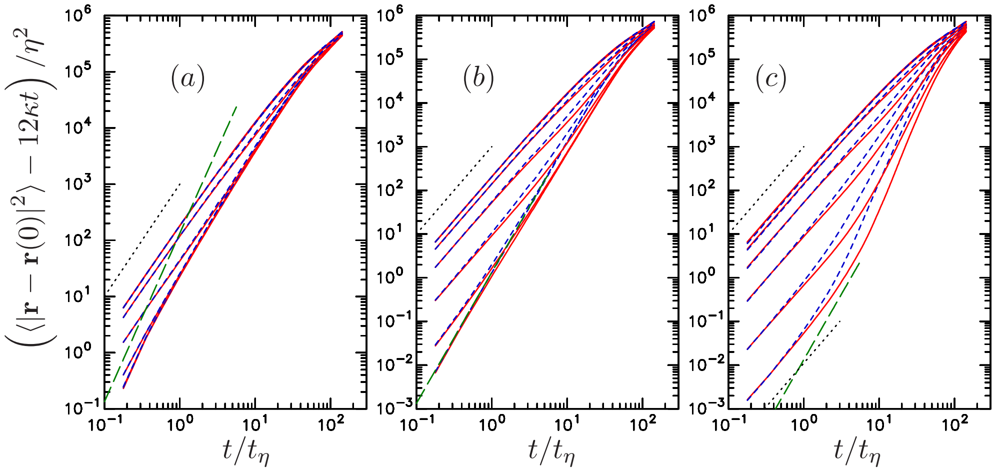

Figure 5.4: Compensated mean-square relative displacement of molecule pairs as a function of forward time (solid lines, in red) and backward time (dashed lines, in blue), scaled by Kolmogorov variables, at $R_\lambda = 140$ for $Sc = 0.01$ (left), 1 (center), 100 (right). Green dashed lines represent the Saffman t^3 small-time limit. Values of $\tilde{r}_0/\eta$ (1/4, 1, 4, 16, 64) increase from bottom to top. (In (a) lines for $\tilde{r}_0/\eta = 1/4$ and 1 are virtually indistinguishable whereas in (b) the $\tilde{r}_0/\eta = 1/4$ data coincide with the green dashed line at small times.) Black dotted lines indicate slope of 2.

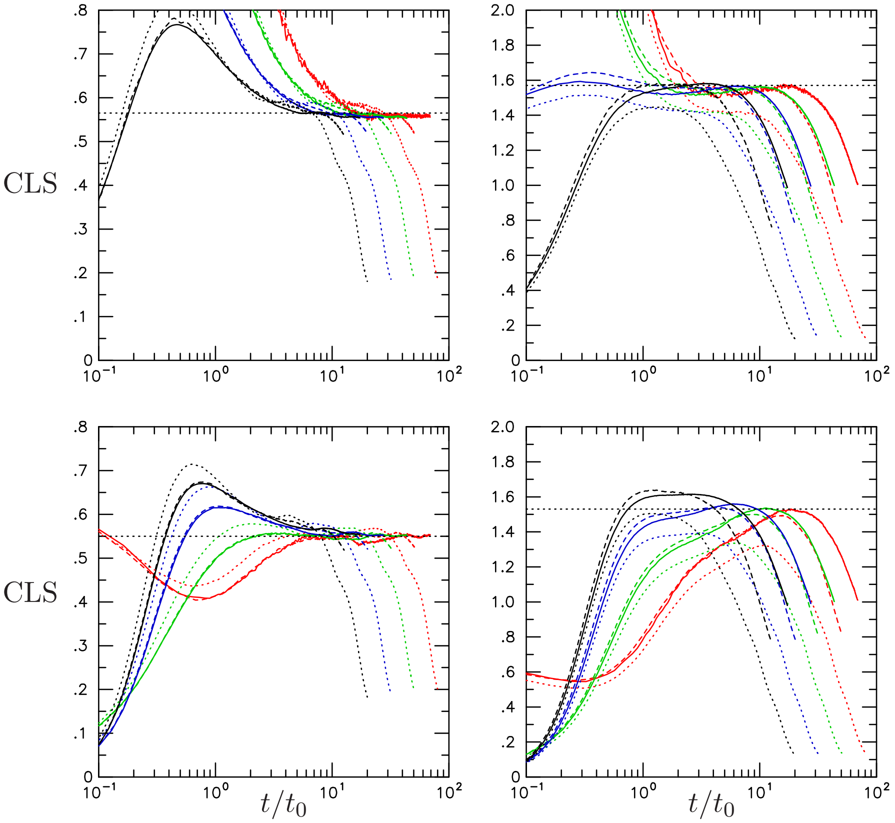

Figure 5.5: Forward (left) and backward (right) cubed-local slope (CLS) of mean-square separation, defined by (5.36), at $R_\lambda = 390$ (dotted), 650 (dashed) and 1000 (solid) for $Sc = 0.125$ (top row) and 1 (bottom row). Initial separations are $\tilde{r}_0/\eta = 2$ (red), 4 (green), 8 (blue) and 16 (black). Horizontal dotted lines drawn for reference at the heights: 0.56 (forward) and 1.57 (backward) for $Sc = 0.125$; 0.55 (forward) and 1.53 (backward) for $Sc = 1$.

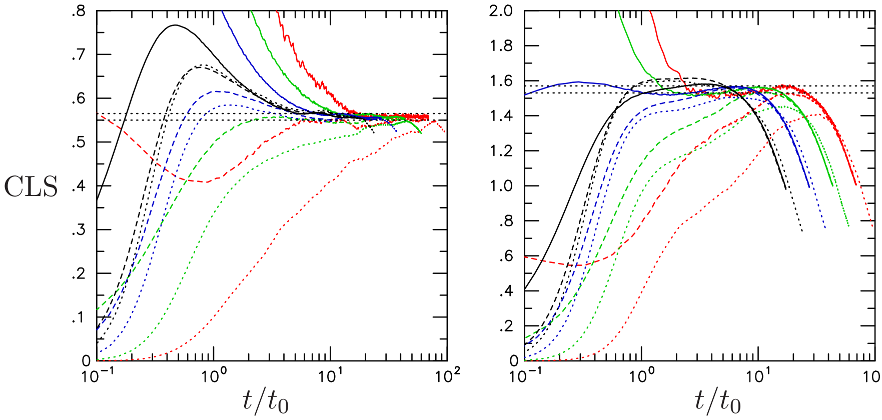

Figure 5.6: Forward (left) and backward (right) cubed-local slope (CLS) at $R_\lambda = 1000$ for $Sc = 0.125$ (solid), 1 (dashed) and ∞ (dotted). Same initial separations as figure 5.5. Horizontal dotted lines drawn for reference at the heights: 0.55 and 0.56 for forward; 1.53 and 1.57 for backward.

Table 5.3: Forward and backward Richardson constants as estimated from the cubed-local slope plots for various R_λ and Sc. Data for $Sc = \infty$ same as that reported in Chapter 4.

Forward				Backward			
R_λ/Sc	0.125	1	∞	R_λ/Sc	0.125	1	∞
390	0.59	0.57		390	1.41	1.32	
650	0.56	0.55		650	1.55	1.50	
1000	0.56	0.55	0.55	1000	1.57	1.53	1.50

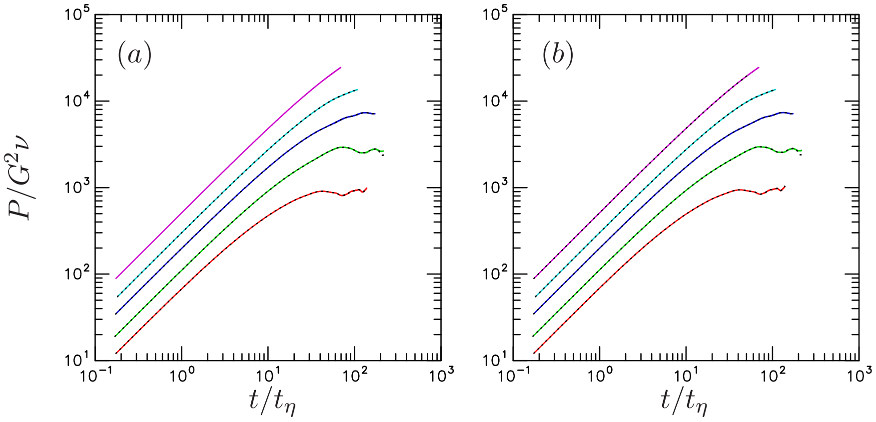

Figure 5.7: Non-dimensional scalar production as obtained from Lagrangian (solid lines) and Eulerian (dotted black lines) approaches, at $R_\lambda = 140$ (red), 240 (green), 390 (blue), 650 (cyan) and 1000 (magenta), increasing from bottom to top. Frames (a) and (b) show data for $Sc = 1/8$ and 1 respectively. Eulerian result at $R_\lambda = 1000$ only for $Sc = 1$.

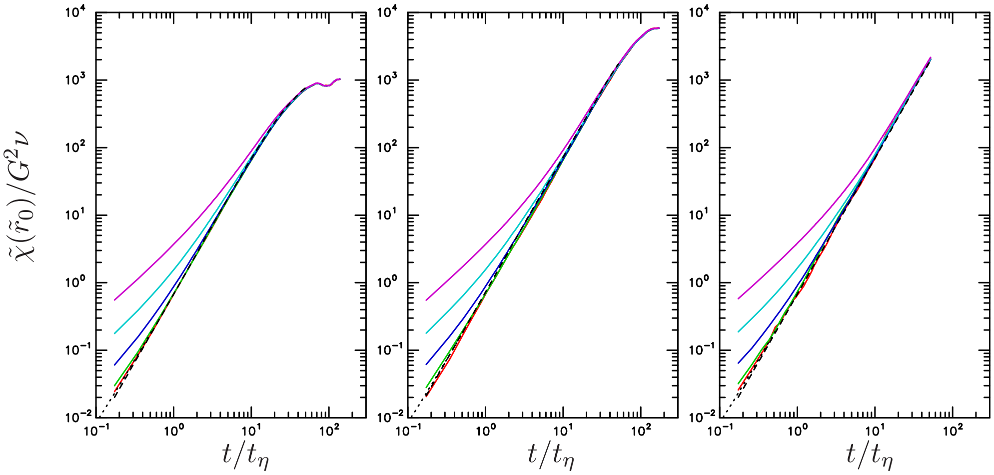

Figure 5.8: Lagrangian estimates of $\tilde{\chi}(\tilde{r}_0)$ at $Sc = 1$ and $R_\lambda = 140$, 390 and 1000 (from left to right), for $\tilde{r}_0/\eta = 1/4$ (red), 1/2 (green), 1 (blue), 2 (cyan) and 4 (magenta) (increasing from bottom to top at small times). The scalar dissipation is given by $\tilde{\chi}(\tilde{r}_0 = 0)$. Dashed black line is the corresponding Eulerian result for the scalar dissipation (which is virtually coincident with Lagrangian data for $\tilde{\chi}$ at $\tilde{r}_0/\eta = 1/4$). A short dotted black line restricted to small times represents (5.44) with $\tilde{r}_0/\eta = 1/4$.

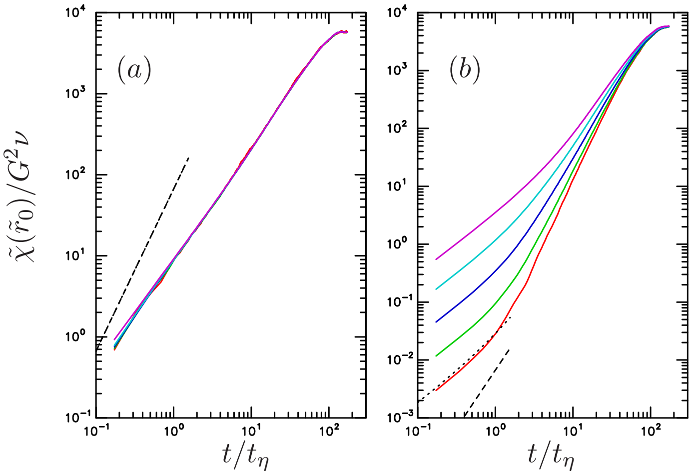

Figure 5.9: Same as figure 5.8, but for $R_\lambda = 390$ at (a) $Sc = 0.01$ and (b) $Sc = 100$. In each frame the black dotted line represents (5.44) while the dashed line represents the Saffman's term in the same equation with $\tilde{r}_0 = 0$.

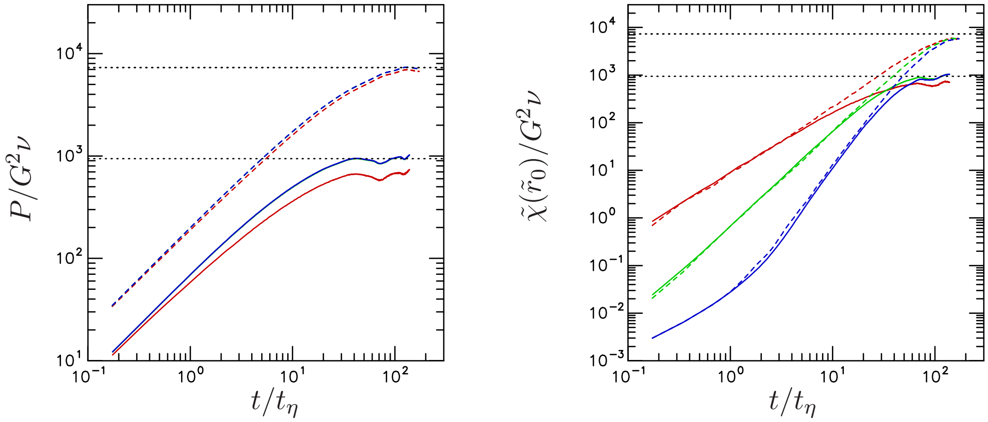

Figure 5.10: Evolution of normalized rates of production (left) and the quantity $\tilde{\chi}(\tilde{r}_0/\eta = 1/4)$ (right) computed from molecular statistics for R_λ 140 (solid lines) and 390 (dashed lines), at $Sc = 0.01$ (red), 1 (green) and 100 (blue), For production the lines for $Sc = 1$ and 100 are virtually indistinguishable. Horizontal black dotted lines drawn for comparison are at heights 0.041 ${R_\lambda}^2$.

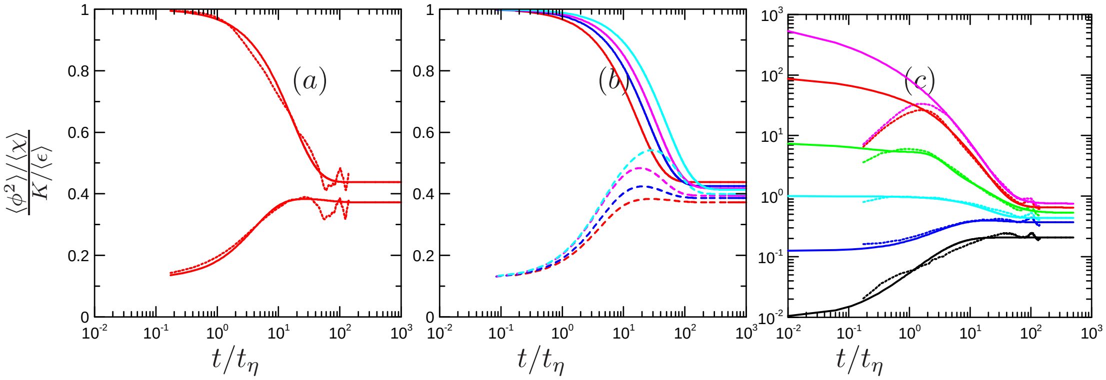

Figure 5.11: Evolution of the ratio of scalar to mechanical time scales. The dashed lines in (a) represent Eulerian data for $Sc = 1/8$ (lower curve) and $Sc = 1$ (upper curve). The corresponding solid lines are smoothing functions satisfying the small and large time limits (6.11)-(6.14). Panel (b) shows these smoothing functions (dashed and solid curves are for $Sc = 1/8$ and 1 respectively) from fits to data at $R_\lambda = 140$ (red), 240 (blue), 390 (magenta) and 650 (cyan) (bottom to top at small times). The dashed lines in panel (c) show Lagrangian data (for $\tilde{r}_0/\eta = 1/4$) at $R_\lambda = 140$ for $Sc = 0.01$ (black), 0.125 (blue), 1 (cyan) , 8 (green), 100 (red) and 1000 (magenta) (bottom to top). The corresponding solid lines are smoothing functions interpolated to the small-time limit (6.11).

CHAPTER VI

BACKWARD DISPERSION OF MULTI-PARTICLE CLUSTERS

6.1 Introduction

While the study of particle (and molecule) pairs is critical in understanding the process of dispersion and mixing, in order to understand the geometrical effects of turbulence, we need to consider clusters of three and four particles. As noted earlier, the n-th moment of the concentration field is in general, determined by the displacement statistics of a n-particle cluster, more specifically in a backward reference frame. Thus in order to predict say the third and fourth order moments of the concentration field, it is important to consider the collective motions of three (triangles) and four (tetrads) particles or molecules. The study of tetrads is of special interest (Pumir *et al.* 2000; Biferale *et al.* 2005; Luthi *et al.* 2007; Hackl *et al.* 2011), since it is the minimum configuration which allows a volume to be defined and hence contains a rich amount of shape information in 3D space. However, backward statistics of tetrads are even more difficult to obtain compared to that of pairs. Recently, Jucha *et al.* (2014) reported backward statistics for tetrads of fluid particles. But the time of observation in their work was very short and restricted to ballistic range and hence no inertial range characteristics were reported. To our best knowledge no other study has reported backward statistics of tetrads. As a result, it is useful to extend the current work to also investigate the backward in time evolution of these multi-particle clusters.

We begin by providing the theoretical background for study of multi-particle clusters, with references to previous work in the forward tracking framework. Then some basic results for tetrads are provided.

6.2 Theory

In general we consider a cluster of n particles located at instantaneous positions: $\mathbf{x}^{(1)}$, $\mathbf{x}^{(2)}$,..., $\mathbf{x}^{(n)}$, at time t (Hackl *et al.* 2011). To derive measures of cluster size, it is useful to consider a hierarchy of transformed variables, for each $1 \leq m \leq n-1$, which expresses the position of $(m+1)^{th}$ particle relative to the center of mass of the first m particles. This defines a set of reduced separation vectors, of the form

$$\mathbf{r}^{(m)} = \sqrt{\frac{m}{m+1}} \left(\mathbf{x}^{(m+1)} - \frac{1}{m} \sum_{i=1}^{m} \mathbf{x}^{(i)} \right) , \tag{6.1}$$

where the coefficients have been chosen such that each $\mathbf{r}^{(m)}$ would have the same variance as the position vector of a single particle, if all position vectors involved were independent. Using these reduced separation vectors, we can define a $3 \times (n-1)$ matrix G, with each column of G being one of the $n-1$ separation vectors as defined in (6.1). We can further form two tensors from G: $\mathbf{G} = GG^T$, which is the moment of inertia tensor, and $\mathbf{C} = G^T G$, which is the dispersion tensor. It can be shown that both $\mathbf{G}$ and $\mathbf{C}$, have the same non-zero and non-negative eigenvalues, which are arranged in descending order as $g_1 \geq g_2 ... \geq g_{n-1}$ (Hackl *et al.* 2011).

A fully rigorous specification of the geometry of an n-particle cluster can be made using the so-called Euler parametrization (Shraiman & Siggia 1998). This consists of the $\min(3, n-1)$ eigenvalues of the tensor $\mathbf{G}$ (or $\mathbf{C}$) defined above and $(n-1)(n-2)/2$ Euler angles which define rotation in $(n-1)$- dimensional pseudo-space (while rotations in physical space merely determine the orientation of the cluster). For tetrads ($n = 4$) we get three Euler angles, which make their use very difficult and hence we focus primarily on the role of three eigenvalues g_1, g_2 and g_3. However for triangles ($n = 3$), there is only one Euler angle and two eigenvalues, which are easier to characterize.

The sum of $\min(3, n-1)$ eigenvalues, or equivalently the trace of $\mathbf{G}$, gives the square of the gyration radius (R) of the cluster, which is also related to the sum of squares of separation distances of all particles involved, i.e.,

$$R^2 = \sum_{\alpha=1}^{n-1} g_\alpha = Tr(\mathbf{G}) = \sum_{m=1}^{n-1} \left|\mathbf{r}^{(m)}\right|^2 = \frac{1}{2n} \sum_{l,m=1}^{n} \left|\mathbf{x}^{(l)} - \mathbf{x}^{(m)}\right|^2 . \tag{6.2}$$

The sum of the eigenvalues represents the size of the clusters, while their ratios, i.e.,

$$I_\alpha = g_\alpha / R^2 , \quad (\alpha = 1, 2, ..., n-1) \tag{6.3}$$

give useful information about the cluster shape (and by definition sum to unity).

For the case of tetrads, with $n = 4$, the reduced separation vectors are given as (Chertkov *et al.* 1999)

$$\mathbf{r}^{(1)} = \left(\mathbf{x}^{(2)} - \mathbf{x}^{(1)}\right)/\sqrt{2} \tag{6.4}$$

$$\mathbf{r}^{(2)} = \left(2\mathbf{x}^{(3)} - \mathbf{x}^{(2)} - \mathbf{x}^{(1)}\right)/\sqrt{6} \tag{6.5}$$

$$\mathbf{r}^{(3)} = \left(3\mathbf{x}^{(3)} - \mathbf{x}^{(3)} - \mathbf{x}^{(2)} - \mathbf{x}^{(1)}\right)/\sqrt{12}\ . \tag{6.6}$$

We can obtain the corresponding volume (regardless of the ordering of particles) as

$$V = \frac{1}{6}\left|\left(\mathbf{x}^{(2)} - \mathbf{x}^{(1)}\right) \cdot \left[\left(\mathbf{x}^{(3)} - \mathbf{x}^{(1)}\right) \times \left(\mathbf{x}^{(3)} - \mathbf{x}^{(1)}\right)\right]\right| \ , \tag{6.7}$$

which is also related to the determinant of the matrix $\mathbf{G}$

$$V = \frac{1}{3}\left(g_1 g_2 g_3\right)^{1/2}\ . \tag{6.8}$$

The interpretation of cluster volume is subject to the caveat that for sheet-like structure, its volume can approach zero even though the particles in the tetrads may be spreading apart from each other. However, the dimensionless parameter defined as

$$\Lambda = V^{2/3}/R^2\ , \tag{6.9}$$

is a convenient measure of the shape, as it varies between 0 for sheet like tetrads of all four particles lying on a plane, to a maximum of $3^{-5/3} = 0.16025$ in the case of a regular tetrahedron with all sides equal and $g_1 = g_2 = g_3$ (Hackl *et al.* 2011). This result follows from the standard inequality between arithmetic and geometric means, i.e., $(g_1+g_2+g_3)/3 \geq (g_1 g_2 g_3)^{1/3}$. It is also related to the shape factors (as defined in (6.3)) as

$$\Lambda = V^{2/3}/R^2 = 3^{-2/3}\left(I_1 I_2 I_3\right)^{1/3}\ , \tag{6.10}$$

which shows its usefulness, in condensing the information on cluster shape. An important point to note is that of I_1, I_2, I_3 and Λ, only two are independent, as the knowledge of any two completely determines all four of them. There are three limiting cases corresponding to (1) $I_3 = 0$ $(I_1 + I_2 = 0)$, which gives sheet like tetrads, (2) $I_1 = I_2 > I_3$, which gives pancake-shaped tetrads, and (3) $I_1 = 1$ with $I_2 = I_3 = 0$, which gives needle-shape tetrads.

The case of $n = 3$ corresponds to triangles, with no volume and just the first two reduced separation vectors. The third eigenvalue g_3 is always identically zero and the radius of gyration is simply give by $R^2 = g_1 + g_2$. This also gives $I_3 \equiv 0$ and $I_1 + I_2 = 1$. An important parameter for triangles is the ratio of its area A to the square of the gyration radius, which is a direct measure of the aspect ratio (Castiglione & Pumir 2001). Following Shraiman & Siggia (1998), we define the aspect ratio w as

$$w = \frac{4A}{\sqrt{3}R^2} \ , \tag{6.11}$$

where the numerical factors are chosen such that w always lies between 0 (for collinear points) and 1 (for equilateral triangles). Both I_1 and I_2 are directly related to w as

$$I_1 = \frac{1}{2}\left(1 + \sqrt{1 - w^2}\right) \ , \tag{6.12}$$

$$I_2 = \frac{1}{2}\left(1 - \sqrt{1 - w^2}\right) \ . \tag{6.13}$$

The aspect ratio w along with one Euler angle χ defined as

$$\chi = \frac{1}{2}\arctan\left(\frac{2\mathbf{r}^{(1)} \cdot \mathbf{r}^{(2)}}{|\mathbf{r}^{(2)}|^2 - |\mathbf{r}^{(1)}|^2}\right) \ , \tag{6.14}$$

fully specifies the two degrees of freedom in the shape of the triangle. The Euler angle χ expresses the orientation of the principal axes in the vector space spanned by $\mathbf{r}^{(1)}$ and $\mathbf{r}^{(2)}$. While the value of χ depends on the ordering of the vertices, one can always define an unique ordering which will result in χ between 0 and $\pi/6$. For an equilateral triangle, χ is undefined since both the numerator and the denominator in (6.14) vanishes. Both extremes of 0 and $\pi/6$ occur for isosceles triangles, with $\chi = 0$ for triangles with two equal sides much greater than the third side and $\chi = \pi/6$ for triangles with two equal sides shorter than the third side. While I_1, I_2 and w are easily interpreted as measures of aspect ratio (note only one of them is independent), χ can be interpreted as a measure of symmetry as reflected in deviation from an isosceles shape.

6.3 Simulation parameters and database

To obtain the statistics of triangles and tetrads, we use the same database as used for particle pairs in Chapter 4. Thus the simulation parameters and database are the same as given by table 4.1. Both the forward and backward statistics are obtained by the postprocessing approach described in § 3.3. However, the number of samples for tetrads (and triangles) for the same bin is significantly less compared to pairs, since now the conditioning requires all six sides to satisfy the same condition (and three for triangles). As a result, the smallest well sampled bin for tetrads is at a larger value of r_0/η compared to that for pairs. The smallest well sampled r_0/η also depends on the Reynolds number (see figure 3.1 and § 3.3 for discussion). For these reasons, the results for tetrads are presented for $r_0/\eta = 8$ and upwards for $R_\lambda = 1000$, whereas for $R_\lambda = 140$ it starts from $r_0/\eta = 1$. To study the inertial range characteristics (which are most closely attained larger Reynolds number), we will mostly focus on the results obtained for $R_\lambda = 1000$.

6.4 Statistics of cluster size

In this section, we present forward and backward statistics of tetrad size, namely, the gyration radius (R) and the volume (V). Similar to two particle statistics, a key objective is the investigation of Richardson scaling at intermediate times.

Figure 6.1 shows the forward and backward time evolution of the tetrad volume, in terms of the square root of its two-thirds moment ($\langle V^{2/3}\rangle^{1/2}$), scaled by Kolmogorov variables, at the lowest and highest Reynolds number listed in table 4.1 (R_λ 140 and 1000 respectively). The choice of the two-thirds moment is primarily motivated by the functional form of Richardson scaling in the inertial range. Since $\langle V^{2/3}\rangle$ is of the same dimension as length-squared, the corresponding inertial range relationship would be linear in $\langle\epsilon\rangle$ (similar to (1.1)) and thus free of intermittency corrections. Similar to results for particle pairs, the forward and backward volume behave similarly at small and large times, while at intermediate times, the backward volume grows faster. At large times, the approach to diffusive limit is again clearest for R_λ 140 simulation, which was relatively long ($T \approx 10T_L$) compared to the R_λ 1000 simulation ($T \approx 2.5T_L$).

Figure 6.2 shows the forward and backward time evolution of r.m.s. gyration radius, $\langle R^2\rangle^{1/2}$, scaled by Kolmogorov variables, under conditions similar to figure 6.1. The trends in different temporal regimes for both forward and backward results are qualitatively similar to the corresponding results for tetrad volume. However at early times, the gyration radius starts increasing from its initial state much earlier than the tetrad volume. This suggests that the effects of dispersion are felt more strongly on gyration radius than on volume. This is not surprising since the tetrad volume is an ambiguous measure of size as discussed previously. For many tetrads, even though the particles might be moving apart, the volume can actually decrease depending on the orientation of the particles (if all particles are on the same plane, the volume becomes zero). As a result, the average volume stays the same for longer duration than the gyration radius. This slow growth in volume also leads to a weaker contrast between the forward and backward result for volume compared to the gyration radius.

Since the gyration radius is directly obtained by summing the squares of each side of the tetrad (multiplied by the factor of 1/4), we can treat each tetrad at $t = 0$ as a collection of six pairs of equal separation (since we consider regular tetrads, which by definition have all six sides equal). Thus the temporal evolution of gyration radius can be studied simply by multiplying the temporal evolution of mean-square displacement of particle pairs by a factor of 3/2, i.e., 6 times the factor 1/4. Thus by using (4.3) we get

$$\langle R^2(t)\rangle - \frac{3}{2}\langle r_0^2\rangle = \begin{cases} \frac{3}{2}\left\langle D_{LL}(r_0) + 2D_{NN}(r_0)\right\rangle t^2 & \text{if} \quad t \ll \max(t_\eta, t_0) \\ \frac{3}{2} g\langle\epsilon\rangle t^3 & \text{if} \quad \max(t_\eta, t_0) \ll t \ll T_L \\ 18\sigma_u^2 T_L t & \text{if} \quad t \gg T_L \ , \end{cases} \tag{6.15}$$

where the symbols have the same meaning as before and the term $3\langle r_0^2\rangle/2$ on the left hand side is the mean-square gyration radius at $t = 0$.

Similar to particle pairs in Chapter 4 and the forward tetrads results of Hackl *et al.* (2011), the small and large time behaviors can be easily verified. We are more interested in the intermediate time behavior, especially for backward statistics which has not been studied before. As discussed and used before, a robust way to identify Richardson scaling at intermediate times is to look at the so called cubed-local slope (CLS),

$$\frac{1}{\langle\epsilon\rangle}\left(\frac{d}{dt}\left[\langle R^2\rangle^{1/3}\right]\right)^3 \tag{6.16}$$

versus Batchelor-scaled times (t/t_0). For gyration radius, if a well-defined Richardson scaling range exists, then a plot of CLS should show a plateau with height equal to 3/2 times the Richardson constant (which was obtained in Chapter 4). In figure 6.3, we show both the forward and backward CLS data for the largest Reynolds number available in current work ($R_\lambda = 1000$), at five values of separation distances. The smallest value starts from $r_0/\eta = 8$ for tetrads due to the sampling issues discussed before.

For the forward case, there is weak indication in this figure of Richardson scaling for $r_0/\eta = 8$ and 16, with the forward Richardson constant around 0.85. This value agrees exactly with that of Hackl *et al.* (2011). For the backward case, the CLS quickly increases to a larger value, however no clear convergence is visible. Based on the backward Richardson constant for particle pairs (estimated as 1.5 in Chapter 4), a horizontal line at 2.25 (3/2 time 1.5) is drawn. While the curve for $r_0/\eta = 8$ seems to plateau around that value at intermediate times, the overall trend is still inconclusive. This suggests that the backward in time gyration radius for tetrads, possibly requires even larger Reynolds number compared to the mean-square separation of two particles to observe Richardson scaling. Even for the forward results, the convergence towards the plateaus is much stronger for the two-particle results. A similar analysis can be repeated for the CLS of volume. However since the gyration radius is a more reliable measure of the size, we currently restrict ourselves to that.

For further information of the structural aspects of tetrads, we consider the individual eigenvalues $g_1 \geq g_2 \geq g_3$ of the moment-of-inertia matrix, whose sum and product give gyration radius and volume respectively. In figure 6.4, we show the forward and backward in time evolution of all three mean eigenvalues, scaled by Kolmogorov variables for the R_λ 1000 simulation. While at small times, both forward and backward statistics are same, the growth at intermediate times is qualitatively different.

For g_1, the backward statistic grows faster as expected, but for g_2 and g_3 there is a brief period where the backward statistic is less than the forward, before ultimately the backward result starts growing faster again.

To analyze this further, we plot the mean eigenvalues along with the mean-square gyration radius for a fixed $\tilde{r}_0/\eta$ in figure 6.5. As it can be seen from the figure, the individual eigenvalues in the backward frame start differing from the forward counterparts earlier than the mean-square gyration radius. This suggests that the small time ballistic behavior of the eigenvalues is different compared to the gyration radius. While the mean-square gyration radius grows according to (6.15) with a t^2 term at small times, the ballistic behavior of individual eigenvalues has a linear t term (Jucha *et al.* 2014; Hackl *et al.* 2011), which cancels out for all eigenvalues when they summed up to obtain R^2. This can also explain the faster decrease for g_2 and g_3 in the backward frame at small times, when the linear term dominates. However at sufficiently large times, the cubic term (with larger backward Richardson constant) dictates the growth rate, leading to stronger backward growth.

The different behavior of different eigenvalues suggest possibly different inertial range scaling characteristic for each eigenvalue. To understand it better, we extend the CLS approach to the eigenvalues. If a well defined Richardson scaling exists for each eigenvalue separately, we can define three new constants, such that, for instance, $\langle g_1 \rangle = C_1 \langle \epsilon \rangle t^3$ and similarly for the other eigenvalues. The CLS curves will then plateau at these new constants, whose sum $C_1 + C_2 + C_3$ should be $3g/2$ (since the sum the eigenvalues is equal to R^2). Figures 6.6 to 6.8 show the forward and backward CLS plots for the three eigenvalues using the same r_0/η values as figure 6.3. Since g_1 is the largest contribution to R^2, it is not surprising that the CLS of g_1 in figure 6.6 resembles that of R^2 in figure 6.3. Both the forward and backward CLS for g_1 show the same behavior, with the plateau approximately at 0.72 and 2.0 respectively. The forward value is once again in excellent agreement with Hackl *et al.* (2011). On the other hand, the CLS curves of g_2 (figure 6.7) and g_3 (figure 6.8), show better convergence with respect to different r_0/η values. Although the results for g_2 and g_3 are noisier, both the forward and backward results show all the r_0/η curves peaking around the same value. The forward constants for g_2 and g_3 are estimated to be 0.12 and 0.012 respectively, which is again in excellent agreement with Hackl *et al.* (2011). The backward constants for g_2 and g_2 are about 0.23 and 0.018. The sum $C_1 + C_2 + C_3$ also is approximately equal to $3g/2$ for both the forward and backward case. The inertial range constants as obtained from all CLS results are summarizes in table 6.1

While the forward results presented here similar to that of Hackl *et al.* (2011), there is a small difference, especially relevant at small times. In the current work, we consider regular tetrads at $t = 0$ such that all sides are r_0 (or rather fall in the bin around r_0). However, Hackl *et al.* (2011) starts from a *trirectangular tetrad* configuration, such that three sides forming the right angle are r_0 and other three sides are $\sqrt{2}r_0$. This leads to $g_1 = g_2 > g_3$ at $t = 0$. Due to this special configuration, the small time behavior of g_1 and g_2, and hence also their CLS is somewhat different. However at intermediate times, once the dependence on initial conditions is lost, regardless of any starting configuration, the same behavior is expected.

6.5 Statistics of cluster shape

It is well known that the forward in time statistics of cluster shape show more robust Richardson scaling than that of cluster size (Hackl *et al.* 2011). Naturally it is important to understand the corresponding behavior for backward statistics. The general nature of backward statistics of cluster size (such as gyration radius, volume, eigenvalues of the moment-of-inertia tensor) is similar to that of two-particle backward statistics. That is, the backward statistics of cluster size are similar to forward at small and large times but stronger at intermediate times, such that observing backward Richardson scaling requires even higher Reynolds number. To understand the corresponding behavior for statistics of cluster shape, we again consider the results for tetrads.

We begin with the shape parameter $\Lambda = V^{2/3}/R^2$. As discussed earlier, in the current work tetrads are formed by identifying four particles such that all six sides fall within the same bin. Since the bins chosen are sufficiently wide to ensure adequate sampling, each individual sample obtained is almost never a regular tetrad (the samples are regular tetrads only on an average). As a result, the initial value of Λ can vary anywhere from 0 to 0.16025. The samples with Λ closer to 0 are essentially planar tetrads, whereas the samples closer to 0.16025 are regular tetrads. Since our aim is to consider regular tetrads, we impose another sampling condition $\Lambda(t = 0) \geq 0.12$. This ensures that the starting tetrads are close to being regular and also provides reasonable sampling (it would be nearly impossible to get any samples of Λ exactly equal to 0.16025).

Figure 6.9 shows the forward and backward in time evolution of the mean value of Λ in Batchelor-scaled time at R_λ 1000 for various r_0/η values. Once again the forward and backward results are similar at small times, both being dictated by ballistic behavior. However at intermediate times, the backward $\langle\Lambda\rangle$ decreases faster than the forward. A scaling regime of near constant $\langle\Lambda\rangle$ emerges for both forward and backward results, although the forward curves show more robust scaling at intermediate times. The strongest scaling for both forward and backward results is obtained for the bin $\tilde{r}_0/\eta = 16$, with the plateaus obtained at 0.045 and 0.036 for the forward and backward results respectively. This exact value for the forward case was also reported by Hackl *et al.* (2011), although the current simulation is shorter and does not show the approach towards the diffusive limit (as marked by the dotted line at 0.0645).

While the inertial scaling for backward $\langle\Lambda\rangle$ is not as strong as the forward case (which is a key feature of all backward statistics reported in current work), it is still better when compared to the backward statistics of cluster size reported in previous section. Furthermore, the smaller scaling value for backward statistics in the inertial range suggests that the distorting effect of turbulence is stronger in the backward reference frame than the forward reference frame. In order to better understand the inertial range behavior, we plot the forward and backward $\langle\Lambda\rangle$ at various Reynolds numbers for the case of $\tilde{r}_0/\eta = 16$ in figure 6.10. At small times all curves nearly overlap, which is a consequence of small-scale universality. At intermediate times, for the smallest R_λ (140), both the forward and backward curves quickly move towards the diffusive limit, showing no signs of inertial range scaling. However as the Reynolds number is increased, the curves gradually start to form a plateau. The plateau is most evident for $R_\lambda = 1000$, extending nearly a decade for the forward case and little less than a decade for the backward case. Approach to diffusive limit is not obtained at higher Reynolds numbers due to the simulation being shorter (however sufficiently long enough to study the inertial range).

Since a tetrad is a 3D entity, its shape cannot be fully described by one single parameter.

Hence, we next consider the shape factors I_1, I_2 and I_3 as defined by (6.3). Since by definition they add up to unity only two of them are independent. Figures 6.11–6.13 show the mean of all the three shape factors at R_λ 1000 for both forward and backward reference frames. The general trend for all shape factors is very similar to that of Λ in figure 6.9. After the initial ballistic behavior, where the forward and backward results are same, there is a flat scaling region at intermediate times, with the forward results showing more robust scaling compared to the backward results. However the backward value of I_1 (figure 6.11) is larger than the forward at intermediate times, whereas for I_2 (figure 6.12) and I_3 (figure 6.13) the backward value is smaller than the forward at intermediate times (similar to Λ). This behavior can be explained by understanding the behavior of the individual eigenvalues (g_1, g_2, g_3) along with R^2. While we know that the backward growth in cluster size is stronger than the forward in time growth, the difference between the backward and forward growth rate is clearly much stronger for g_1 compared to g_2 and g_3 as seen earlier from figure 6.4. Since g_1 is always the dominant contribution to R^2, the backward $\langle I_2 \rangle$ and $\langle I_3 \rangle$ decreases faster (whereas backward $\langle I_1 \rangle$ increases faster) than the forward counterparts.

The behavior of backward in time shape factors is consistent with that of backward Λ, though it further quantifies the degree of deformation in each direction. While the overall distortion in shape is faster in backward reference frame, this distortion is achieved by an increasing value of $\langle I_1 \rangle$ and decreasing value of $\langle I_2 \rangle$ and $\langle I_3 \rangle$. This means there is an overall tendency of the tetrads elongating more along the I_1 direction resulting in more needle-like structures, although a detailed investigation of the joint PDF of shape factors will provide more conclusive evidence. To summarize, we have listed the inertial range constants for all shape parameters (both forward and backward) in table 6.2. The forward results are in perfect agreement with the work of Hackl *et al.* (2011). In general backward dispersion causes similar distortion as forward dispersion, though the amplitude of distortion is higher in backward frame.

6.6 Summary

In this chapter we have investigated the forward and backward statistics of multi-particle clusters. While the work is still ongoing, we have presented some initial results for the forward and backward statistics of tetrads. The postprocessing algorithm discussed in Chapter 3 is used to extract tetrads from single particles such that all the sides of chosen tetrads fall in the same bin (statistically we can treat them as regular tetrads) at $t = 0$.

The statistics of tetrad size, such as gyration radius, volume and eigenvalues of the moment-of-inertia tensor have been reported. The general behavior of forward and backward statistics of tetrad size is similar to that particle pairs. At small and large times, the forward and backward statistics are similar, whereas at intermediate times the backward statistics grow faster. The cubed-local slope (CLS) approach is used to investigate Richardson scaling at intermediate times. In general the Richardson scaling for forward statistics is more robust than the backward statistics. However compared to two-particle statistics, Richardson scaling for measures of tetrad size seems less robust.

The statistics of tetrad shape, as represented by Λ and the shape factors have also been reported. A consequence of stronger backward dispersion appears to be faster distortion of tetrad shape in the backward reference frame. An overall observation in this work, consistent with that of Hackl *et al.* (2011), is that the inertial range scaling is more readily observed in the statistics of shape than those of size. However, the forward results always show more robust inertial range scaling, while a higher Reynolds number is required for backward statistics (a recurring requirement observed even in Chapters 4 and 5). It is evident that the backward dispersion statistics for both size and shape needs more investigation and also needs to be extended to triangles. Furthermore, a similar extension to study triangles and tetrads of molecules is necessary to understand turbulent mixing.

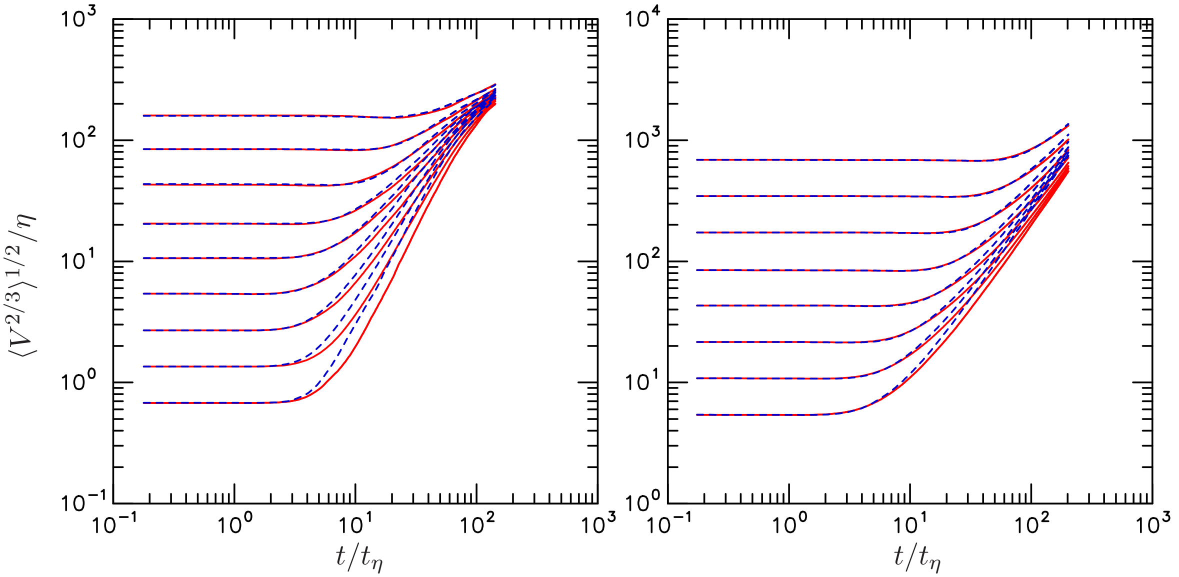

Figure 6.1: Forward (solid red lines) and backward (dashed blue lines) in time evolution of linear tetrad size derived from the tetrad volume, in the form $\langle V^{2/3}\rangle^{1/2}$, normalized by Kolmogorov variables, at $R_\lambda = 140$ (left frame) and $R_\lambda = 1000$ (right frame). The initial separations, increasing from bottom to top are $\tilde{r}_0/\eta = 1$, 2, 4, 8, 16, 32, 64, 128, 256 for R_λ 140 and $\tilde{r}_0/\eta = 8$, 16, 32, 64, 128, 256, 512, 1024 for R_λ 1000.

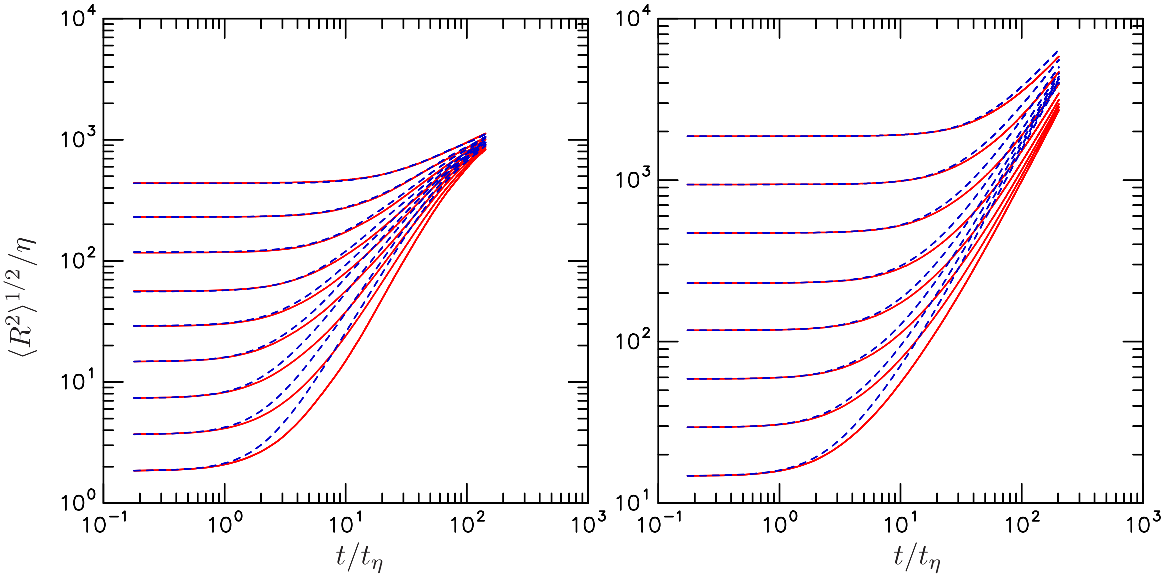

Figure 6.2: Forward (solid red lines) and backward (dashed blue lines) in time evolution of root-mean-squared gyration radius, $\langle R^2\rangle^{1/2}/\eta$, normalized by Kolmogorov variables, at same conditions shown in figure 6.1.

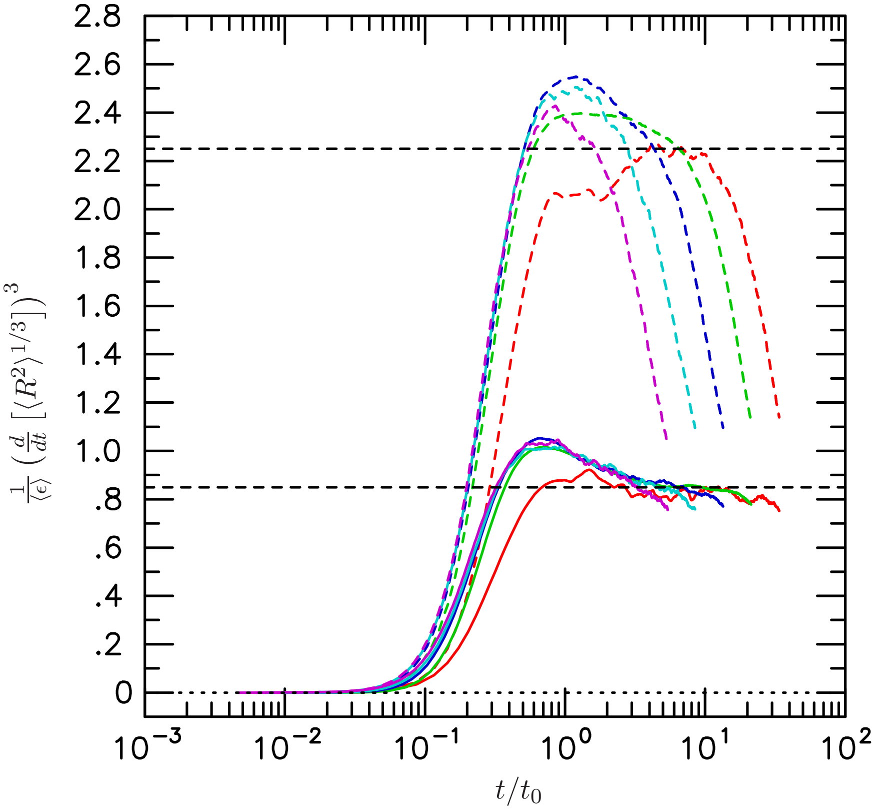

Figure 6.3: Forward (solid lines) and backward (dashed lines) cubed-local-slope for mean-square gyration radius at $R_\lambda = 1000$. Initial separations are $\tilde{r}_0/\eta = 8$ (red), 16 (green), 32 (blue), 64 (cyan) and 128 (magenta). Curves move to the left with increasing $\tilde{r}_0/\eta$. Horizontal dashed lines are drawn for reference at heights 0.85 (forward) and 2.25 (backward).

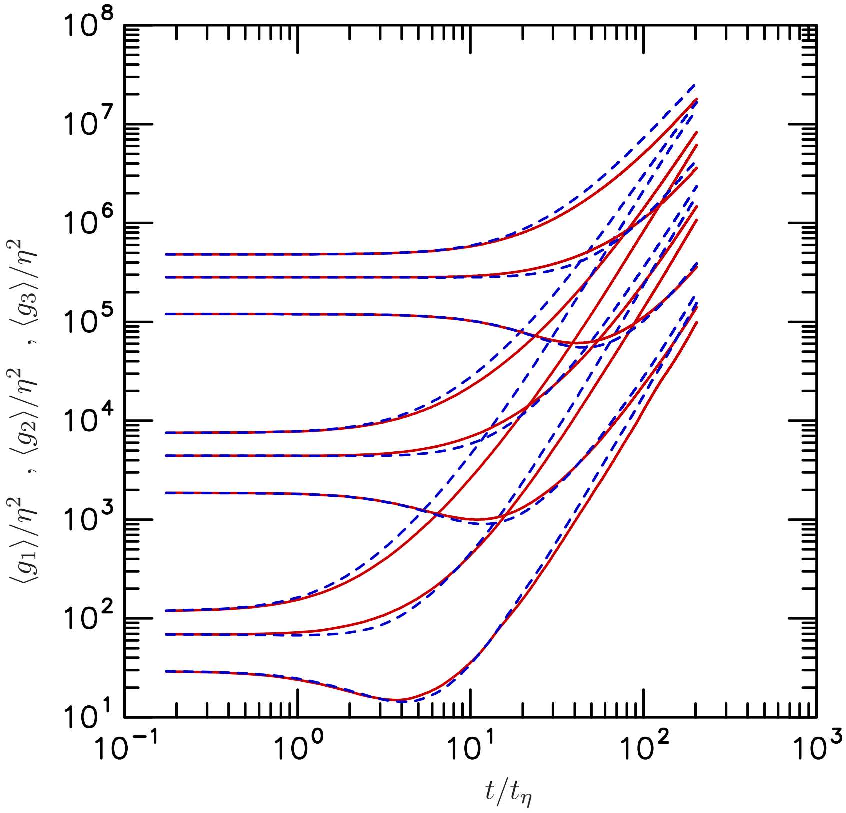

Figure 6.4: Forward (solid red lines) and backward (dashed blue lines) in time evolution of mean tetrad eigenvalues in Kolmogorov variables at $R_\lambda = 1000$. Three sets of curves for $\langle g_1\rangle$, $\langle g_2\rangle$, $\langle g_3\rangle$ are shown, for initial separations $\tilde{r}_0/\eta = 8$ (lower), 64 (middle), and 512 (upper). Note that $g_1 > g_2 > g_3$, by definition. At sufficiently large times curves for each eigenvalue (but different $\tilde{r}_0/\eta$) are seen to converge upon one another.

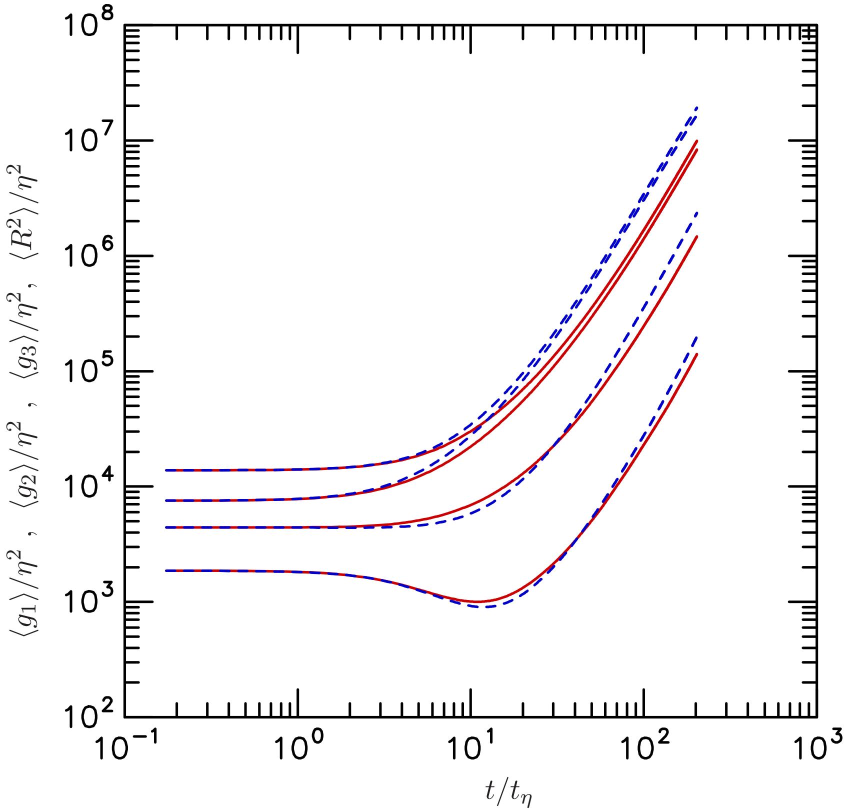

Figure 6.5: Forward (solid red lines) and backward (dashed blue lines) in time evolution of mean tetrad eigenvalues and mean-square gyration radius scaled by Kolmogorov variables at $R_\lambda = 1000$ for $\tilde{r}_0/\eta = 64$. The curves from bottom to top represent g_1, g_2, g_3 and R^2.

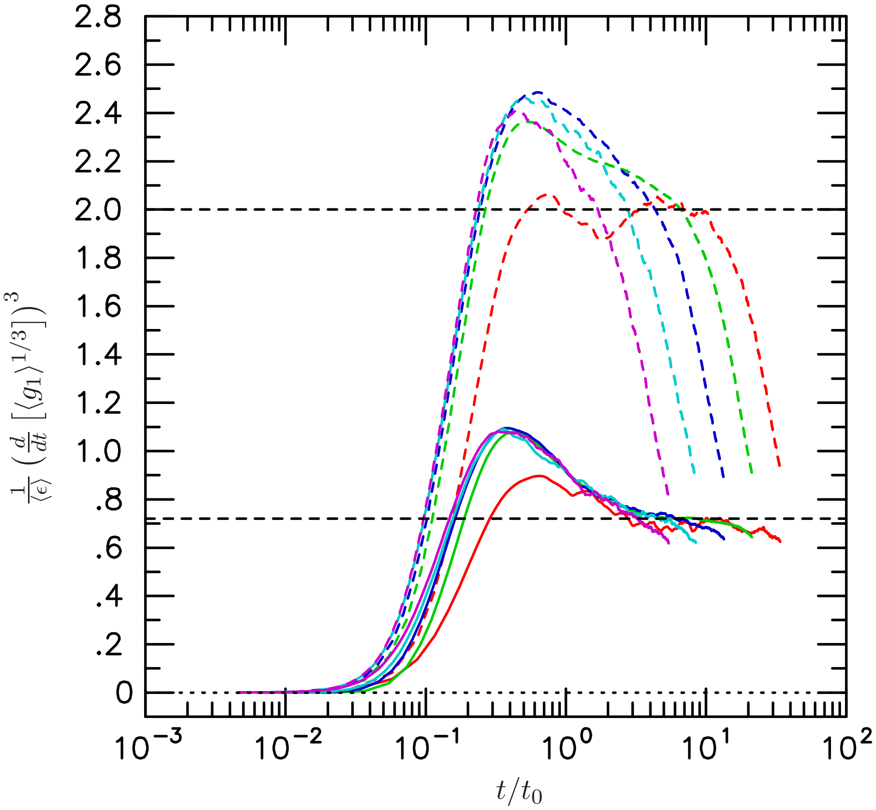

Figure 6.6: Forward (solid lines) and backward (dashed lines) cubed-local-slope of mean of first eigenvalue ($\langle g_1\rangle$) under same conditions and labeled in the same manner as in figure 6.3. Horizontal dashed lines are drawn for reference at heights 0.72 (forward) and 2.0 (backward).

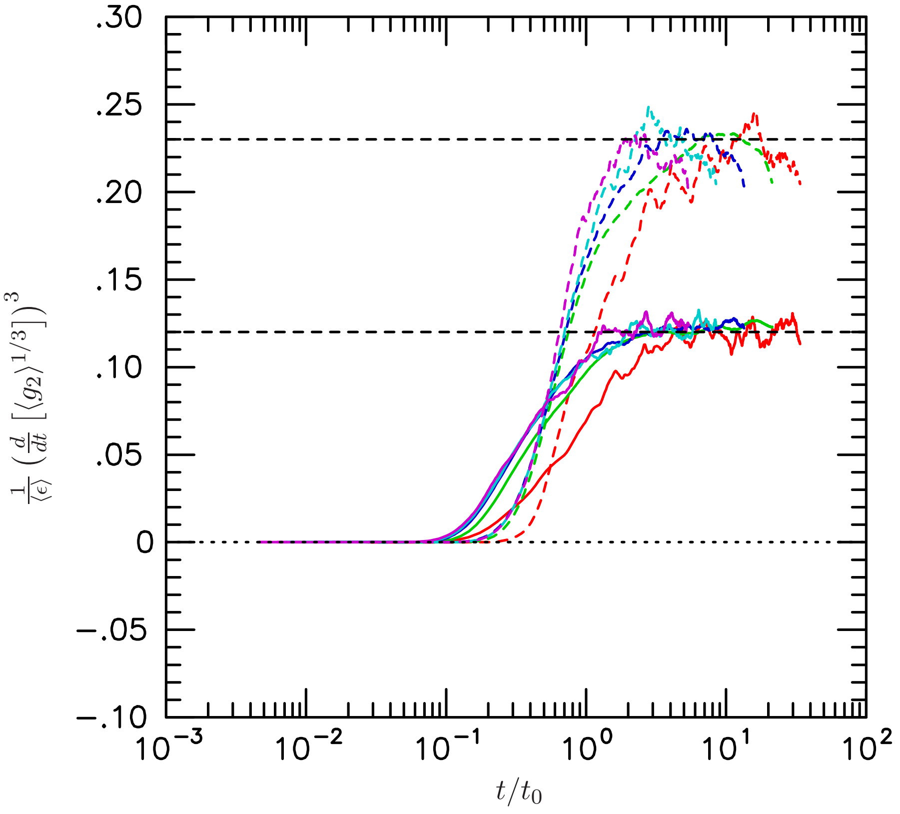

Figure 6.7: Forward (solid lines) and backward (dashed lines) cubed-local-slope of mean of first eigenvalue ($\langle g_2 \rangle$) under same conditions and labeled in the same manner as in figure 6.3. Horizontal dashed lines are drawn for reference at heights 0.12 (forward) and 0.23 (backward).

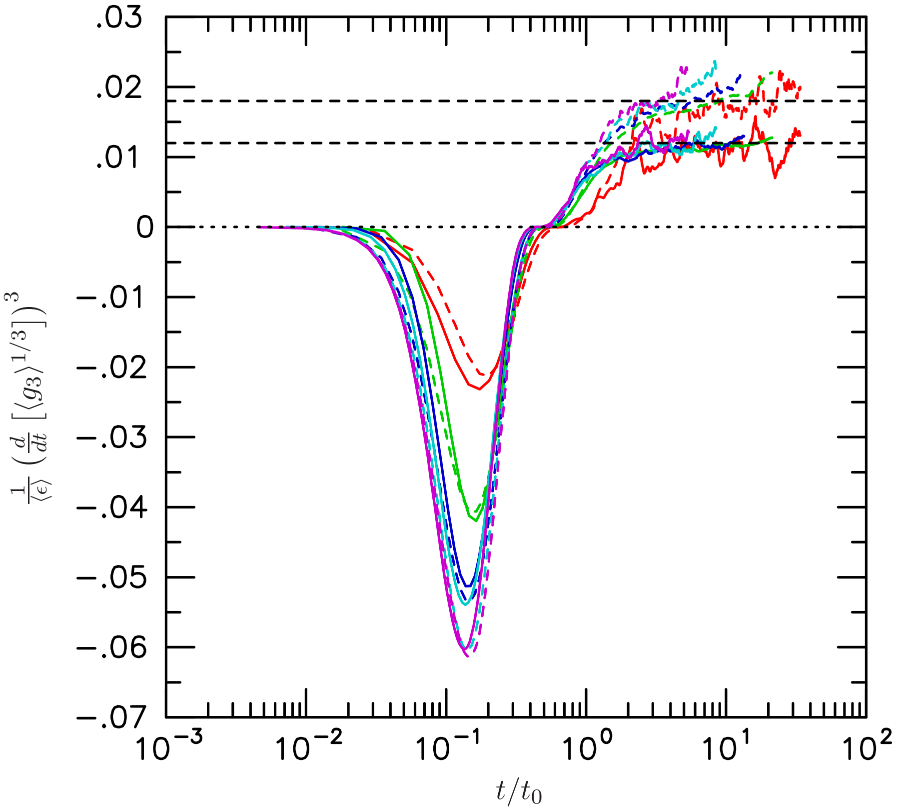

Figure 6.8: Forward (solid lines) and backward (dashed lines) cubed-local-slope of mean of first eigenvalue ($\langle g_3\rangle$) under same conditions and labeled in the same manner as in figure 6.3. Horizontal dashed lines are drawn for reference at heights 0.012 (forward) and 0.018 (backward).

Table 6.1: Estimated values of inertial range scaling constants, forward and backward, based on cubed-local-slopes of statistics of tetrad size. These values are inferred from the simulation data at $R_\lambda = 1000$ as shown in figures 6.3, 6.6–6.8.

	$\langle R^2 \rangle$	$\langle g_1 \rangle$	$\langle g_2 \rangle$	$\langle g_3 \rangle$
Forward	0.85	0.72	0.12	0.012
Backward	2.25	2.0	0.23	0.018

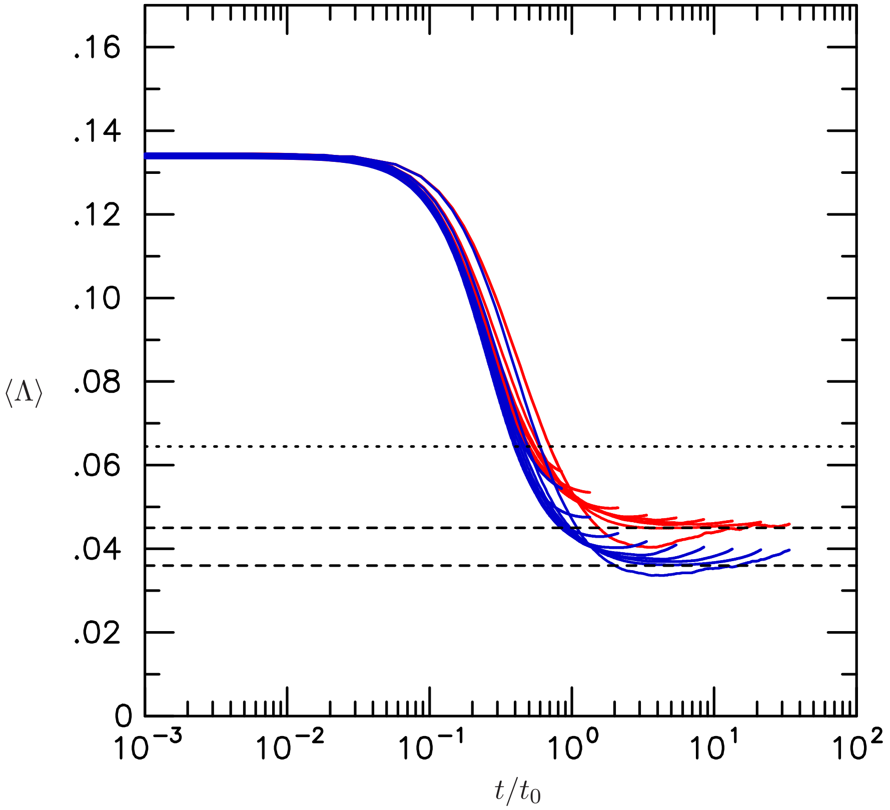

Figure 6.9: Forward (solid red lines) and backward (solid blue lines) in time evolution of mean of $\Lambda = V^{2/3}/R^2$ at $R_\lambda = 1000$. Initial separations are, for curves terminating at the rightmost edge of the plot to the left, $\tilde{r}_0/\eta$ = 8, 16, 32, 64, 128, 256, 512, and 1024. Curves for backward $\langle\Lambda\rangle$ lie below curves for forward $\langle\Lambda\rangle$. Dashed horizontal lines at 0.045 (forward) and 0.036 (backward) marks the inertial range scaling constants. Dotted horizontal line at 0.065 marks the diffusive limit.

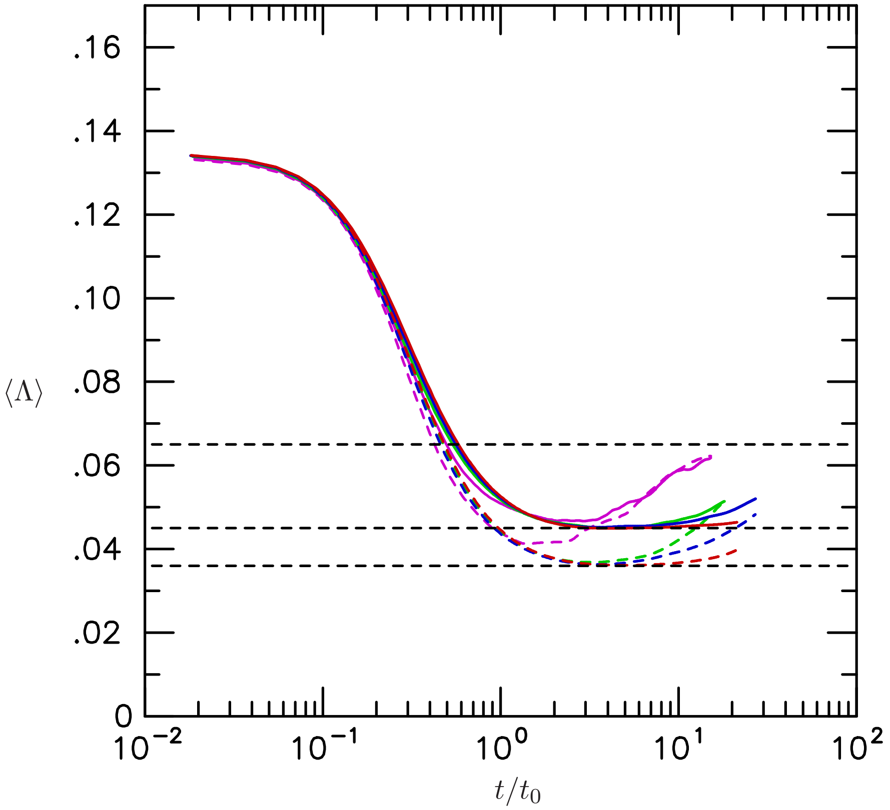

Figure 6.10: Forward (solid lines) and backward (dashed lines) in time evolution of mean of $\Lambda = V^{2/3}/R^2$ at $R_\lambda = 140$ (magenta), 390 (green), 650 (blue) and 1000 (red) for $\tilde{r}_0/\eta = 16$. Curves for backward $\langle\Lambda\rangle$ lie below the curves for forward $\langle\Lambda\rangle$. Dashed horizontal lines at 0.045 (forward) and 0.036 (backward) marks the inertial range scaling constants. Dotted horizontal line at 0.065 makes the diffusive limit.

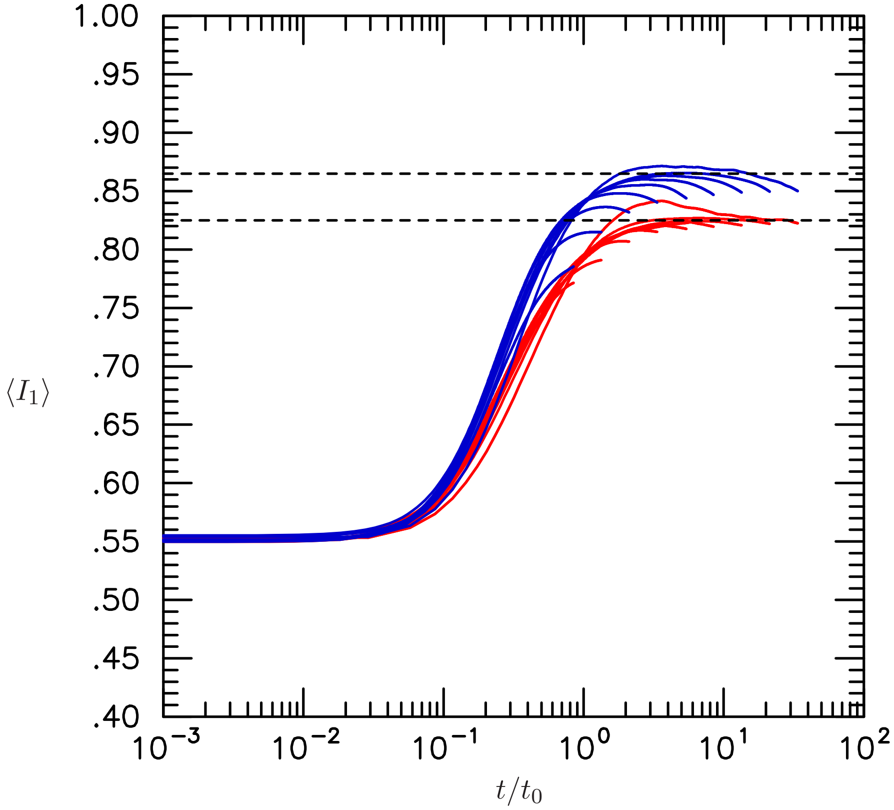

Figure 6.11: Forward (solid red lines) and backward (solid blue lines) in time evolution of mean of shape factor $I_1 = g_1/R^2$ under same conditions as figure 6.9. Curves for backward $\langle I_1 \rangle$ lie above the curves for forward $\langle I_1 \rangle$. Dashed horizontal lines at 0.825 (forward) and 0.865 (backward) marks the inertial range scaling constants.

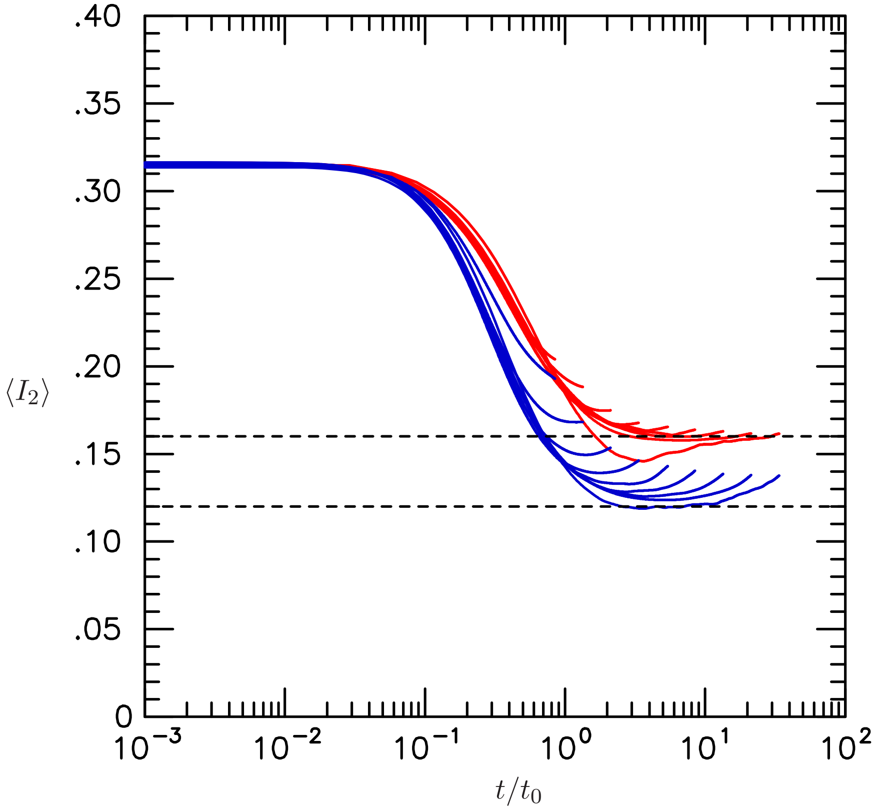

Figure 6.12: Forward (solid red lines) and backward (solid blue lines) in time evolution of mean of shape factor $I_2 = g_2/R^2$ under same conditions as figure 6.9. Curves for backward $\langle I_2 \rangle$ lie below the curves for forward $\langle I_2 \rangle$. Dashed horizontal lines at 0.16 (forward) and 0.12 (backward) marks the inertial range scaling constants.

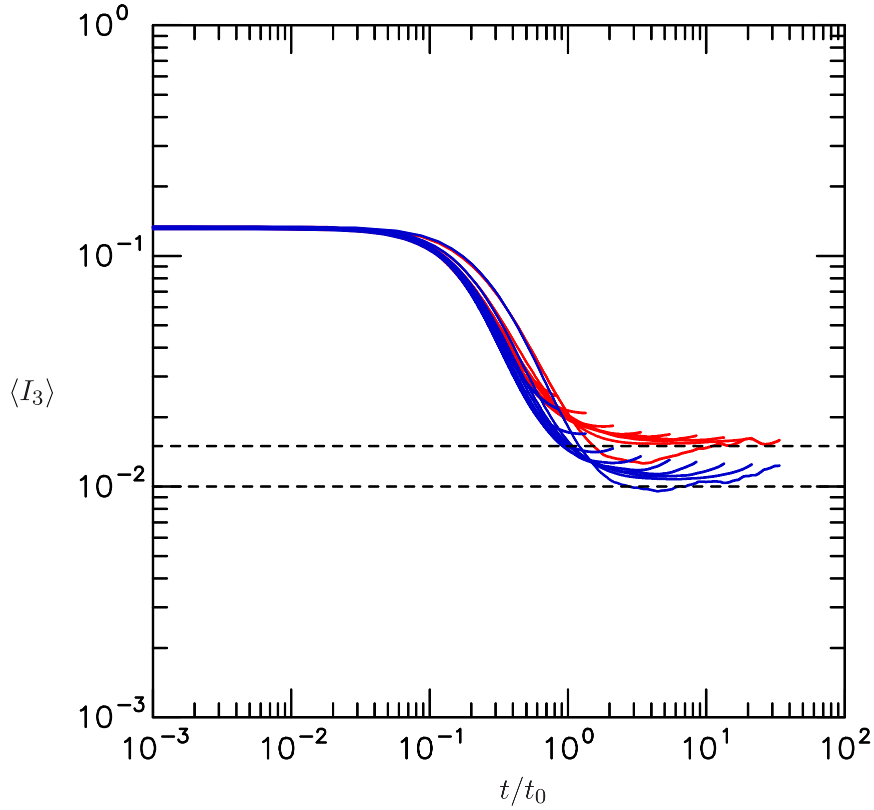

Figure 6.13: Forward (solid red lines) and backward (solid blue lines) in time evolution of mean of shape factor $I_3 = g_3/R^2$ under same conditions as figure 6.9. Curves for backward $\langle I_3 \rangle$ lie below the curves for forward $\langle I_3 \rangle$. Dashed horizontal lines at 0.015 (forward) and 0.01 (backward) marks the inertial range scaling constants.

Table 6.2: Estimated values of inertial range scaling constants, forward and backward, for statistics of tetrad shape. These values are inferred from the simulation data at $R_\lambda = 1000$ as shown in figures 6.9, 6.11–6.13.

	$\langle \Lambda \rangle$	$\langle I_1 \rangle$	$\langle I_2 \rangle$	$\langle I_3 \rangle$
Forward	0.045	0.825	0.16	0.015
Backward	0.036	0.865	0.12	0.010

CHAPTER VII

CONCLUSIONS AND FUTURE WORK

In the current work, we have used direct numerical simulations (DNS) to study turbulent dispersion and mixing from a Lagrangian perspective over a wide range of Reynolds numbers. In DNS, the Navier-Stokes equations are solved numerically (in an Eulerian framework) and a large population of particles are simultaneously tracked using a massively parallel algorithm. A new computational framework has been developed to enable particle tracking in DNS at Petascale problem sizes, at Reynolds numbers higher than previously available in the literature. A new massively parallel postprocessing algorithm has also been developed and applied to obtain Lagrangian statistics from saved particle trajectories (as obtained from DNS). These statistics have provided new physical insights into the process of turbulent dispersion and mixing. The conclusions for the main topics undertaken in this thesis are summarized next, followed by some remarks about possible future work.

7.1 Summary of the main conclusions

7.1.1 Numerical and computational aspects

In DNS, a key task in particle tracking is to obtain the velocity at particle positions by interpolating from the neighboring grid points. Since the entire solution domain is divided among a large number of parallel processors (or so-called MPI tasks) and the particles are free to wander under the influence of turbulence, this interpolation operation requires frequent exchange of information between the processors. One approach is to keep each processor responsible for the same set of particles (which were initiated on that processor) and receive the required information for interpolation from other processors at every time step. This approach requires global exchange of information using collective communication protocols and hence is called the ‘global’ approach. Another approach is to allow each processor to be responsible for a dynamically evolving population of particles, such that at every time step the required information for interpolation is available locally on the processor, and hence is called the 'local' approach. The global approach performs reasonably well at small to moderate problem sizes and has been used in the previous works. However, it scales very poorly at large Petascale problem sizes due to expensive collective communication calls. In the current work we have developed a new local approach for particle tracking. The communication process is limited to neighboring processors in a localized region and as a result has excellent scaling characteristics. Special consideration has been given in optimizing the performance of both the Eulerian and the Lagrangian part of the DNS code, by using one-sided communication to accomplish the interpolation in parallel. For the largest problem size of 8192^3 grid points with 300 million particles on $262,144$ processors a speed up of more than 40X is obtained for the Lagrangian part of the DNS code, using the newly developed local approach.

Another key computational task is the postprocessing of raw data written out from DNS. While from DNS time histories of millions of single particles are obtained, to study turbulent dispersion and mixing, we need to calculate statistics of particle pairs and clusters (three or four particles). This is done in postprocessing by choosing all the available combinations of two or more particles from the single particles. For example, given N_p particles, a total of $N_p(N_p-1)/2$ unique particle pairs can be formed. In general, for a cluster of n particles ($n=2$ for pairs, 3 for triangles and 4 for tetrads), a population in the order of N_p^n clusters can be formed. As a result, the cost of postprocessing can grow very rapidly (typically N_p is many millions). In the current work, we have developed and used a new massively parallel postprocessing algorithm to obtain statistics of particle pairs and clusters. The entire population of N_p particles is divided among a large number of processors. The desired clusters are formed simultaneously on each processor, by systematically cycling the data, until statistical convergence is achieved. Near-perfect strong and weak scaling is obtained for the corresponding code.

7.1.2 Relative dispersion of fluid particles

In problems related to turbulent dispersion, the common approach is to follow the fluid particle trajectories forward in time, along with the Eulerian flow. However, in Lagrangian studies of turbulent mixing, the trajectories of fluid particle pairs tracked backward in time are of greater importance. In principle, backward tracking can be accomplished by storing complete velocity fields at every time step in a previously conducted DNS. However, such an approach becomes prohibitively expensive at large Reynolds numbers. The new postprocessing approach developed in this work has enabled the study of both forward and backward dispersion without being restricted by expensive data storage algorithms. In particular it has allowed us to study the process of backward dispersion at Reynolds numbers significantly higher than previously reported in literature.

In Chapter 4, we have studied backward dispersion of fluid particle pairs. A major focus is to understand and quantify the differences between backward and forward relative dispersion, especially at intermediate times, where inertial subrange universality holds. Using the data over a wide range of Reynolds number and initial separations, we have been able to demonstrate and quantify Richardson t^3 scaling for the mean-squared separation in both forward and backward dispersion. At intermediate times, backward dispersion is stronger than forward, leading to an earlier approach to diffusive conditions. As a result, backward statistics have a diminished range of inertial range behavior, requiring higher Reynolds number to observe Richardson scaling. However, the Reynolds numbers in our simulations are sufficiently high to demonstrate Richardson scaling for both forward and backward cases. The corresponding forward and backward Richardson constants are found to be $g_f = 0.55$ and $g_b = 1.5$ respectively. In contrast to second order moments, higher order moments of separation do no show Richardson scaling, since with increasing order the moments are increasingly influenced by dissipation range effects. Furthermore, the so-called distance-neighbor function showed only transitory agreement with the well-known Richardson prediction.

The asymmetry between backward and forward relative dispersion was further investigated by considering a Taylor series expansion in the small-time limit. The difference between the backward and forward mean-square relative displacement has a t^3 dependence at small times, controlled by the covariance of relative acceleration and relative velocity, which is non-zero and equal to $-2\langle\epsilon\rangle$ in the inertial range at large Reynolds numbers. The analysis is also extended to higher order moments of the relative displacement, which show a similar asymmetry in time. However, we conclude that these asymmetries and particularly the t^3 growth of the difference between backward and forward mean-square relative displacement, are not simply connected to the t^3 growth in the Richardson regime and the asymmetry manifested there.

7.1.3 Lagrangian turbulent mixing: dispersion of molecules

In Chapter 5, we have addressed the effects of molecular diffusion which are crucial in understanding turbulent mixing from a Lagrangian perspective. The postprocessing algorithm to study forward and backward dispersion is extended to extract statistics of the trajectories of diffusing molecules that undergo Brownian motion relative to the fluid. Detailed results are obtained for Schmidt numbers (Sc) from 0.001 to 1000 at Taylor-scale Reynolds number (R_λ) up to 1000. We have first investigated how the forward and backward statistics of molecules (singly and in pairs) in different temporal regimes depend on Sc and R_λ. Then these statistics are related to Eulerian results for a passive scalar driven by a uniform mean-gradient.

Statistics of displacements of single molecules compare well with the earlier theoretical work of Saffman (1960) except for the scaling of the integral time scale of the fluid velocity following the molecular trajectories. For molecular pairs we extend Saffman's theory to include pairs of small but finite initial separation. Excellent agreement is obtained between the theory and numerical results in the ballistic and diffusive limits. At intermediate times, both forward and backward statistics of molecular pairs exhibit a more robust Richardson scaling behavior than for the fluid particles. This is due to the added Brownian motion, which causes pairs to separate and lose memory of their initial separation faster. However if molecular diffusion is very strong (when Reynolds number is not large and Sc is very low), no scaling is observed. The forward scaling constant is very close to 0.55, whereas the backward constant is about 1.53–1.57, with a weak Schmidt number dependence, which is in good agreement with the limited data in the literature.

An important innovation in this work is to demonstrate explicitly the practical utility of a Lagrangian description of turbulent mixing, where molecular displacements and separations in the limit of small backward initial separation can be used to calculate the evolution of scalar fluctuations resulting from a known source function in space. Lagrangian calculations of production and dissipation rates of the scalar fluctuations are shown to agree very well with Eulerian results for the case of passive scalars driven by a uniform mean gradient. Although the Eulerian-Lagrangian comparisons are made only for $Sc \sim \mathcal{O}(1)$, the Lagrangian approach is more easily extended to both very low and very high Schmidt numbers. The well known scalar dissipation anomaly is also addressed in a Lagrangian context. Our results show that molecular diffusivity cannot be neglected at small times, where the scalar dissipation depends directly on Sc, whereas in the large time limit, both scalar dissipation rate and the scalar timescale become independent of Sc in the limit of large Reynolds number.

7.1.4 Multi-particle clusters

In Chapter 6, we investigate forward and backward dispersion of multi-particle clusters of fluid particles. As in study of particle pairs, our primary focus is on inertial range scaling, especially for backward dispersion statistics of clusters. Measures of cluster size and shape are considered separately, with the latter exhibiting more robust inertial range scaling. We mostly focus on statistics of four-particle clusters, namely tetrads, which is the smallest possible cluster configuration allowing a volume to be defined and contains a rich amount of information in 3D space.

For measures of tetrad size, we have investigated the volume (V) and more appropriately, gyration radius (R). Similar to particle-pair dispersion, the statistics of tetrad size grow faster in the backward reference frame at intermediate times. Since a tetrad can be interpreted as a collection of six particle pairs, the mean-square gyration radius of tetrad has a functional form similar to that of mean-square relative displacement of particle pairs, only differing by a constant factor of 3/2. However, the Richardson scaling for mean-square gyration radius, in both forward and backward reference frame, is not as robust as that of mean-square separation of particle pairs. Nevertheless, we have been able to demonstrate Richardson scaling for mean-square gyration radius and the eigenvalues of the moment-of-inertia tensor (the sum of the eigenvalues is equal to the square of gyration radius). Excellent agreement is obtained for the forward results with previously reported data in the literature, whereas the backward results are first of its kind.

The tetrad shape is represented by the non-dimensional ratio $\Lambda = V^{2/3}/R^2$ as well as the shape factors defined as normalized eigenvalues of the moment-of-inertia tensor. Both the forward and backward statistics of tetrad shape show inertial range scaling, and is more robust than that of statistics of tetrad size. This suggests that the geometrical effects of turbulence, represented by statistics of tetrad shape are more amenable to modeling or theoretical description than the dispersive effects of turbulence, as represented by measures of tetrad size. At the same time, the general behavior of forward and backward statistics of tetrad shape, suggests that the distorting effects of turbulence at intermediate times are stronger in the backward frame, resulting in a stronger deformation of the tetrad shape.

7.2 Future work

It is evident that the problem of multi-particle cluster evolution is less studied and less understood than the case of two-particle relative dispersion, especially for the case of backward dispersion. An immediate extension of the current work would be to further the study the backward dispersion of multi-particle clusters. While some results for tetrads are presented in the current work, they need to be understood in greater detail and also extended to triangles. Furthermore, we can extend the current work to multi-particle clusters of molecules, for which, to best of our knowledge, no formal study exists in literature. The backward statistics of triangle and tetrads are directly connected to the third and fourth order moments of a passive scalar field and can be tremendously useful for understanding the highly and weak diffusive regimes (given by very low and very high Schmidt numbers respectively) of scalar mixing, which are very difficult to study in Eulerian simulations.

In the current study, we have focused on turbulent mixing of one passive scalar, also called 'Level-1' mixing in the review by Dimotakis (2005). A natural extension is to study mixing of two or more coupled passive scalars of different molecular diffusivities, which is important in many applications in both nature and engineering. Most notable examples include mixing of temperature and salinity fields in ocean currents (Adkins *et al.* 2002; Wunsch 2002; Wunsch & Ferrari 2004), differential diffusion of passive scalars (Yeung & Pope 1993; Juneja & Pope 1996) and broadcast spawning in marine biology (Crimaldi & Browning 2004; Crimaldi 2012). The current approach developed in Chapter 5 can be readily extended to study this. For example, by considering pairs of molecules with different Schmidt numbers, one can obtain the covariance between two scalars and hence also the joint scalar dissipation. As mentioned earlier, this would be particularly beneficial for very low or very high Schmidt numbers, which are very difficult to study in an Eulerian framework.

The computational advances made in particle tracking in the current work has allowed us to generate Lagrangian data at Reynolds number higher than previously reported in the literature. While the simulation is still in the production phase, it will eventually allow us to answer many outstanding questions in fundamental turbulence research. Recently, Yeung *et al.* (2015) found that the nature of extreme events in dissipation and enstrophy at very large Reynolds number is fundamentally different from that previously observed at low to moderate Reynolds number (Kawahara 2005). However, the origin of such extreme events is still not well understood. From a Lagrangian viewpoint, one can trace the evolution of clusters of particles originating in such regions, which can be useful in understanding the origins of such extreme events.

A higher Reynolds number also provides a more reliable way of understanding inertial range scaling behavior, especially for Lagrangian statistics, which have a smaller extent of inertial range compared to the Eulerian statistics. A higher Reynolds number is also required to study Lagrangian intermittency, which is strongly manifested in small scale statistics such as acceleration. While the subject is well established, there still remains many open questions about the small scale universality of single particle Lagrangian statistics (Sawford & Yeung 2011).

The study of velocity gradients along trajectories of fluid particles can also help shed some light on the behavior of the small scales. The local straining and rotational effects of turbulence and hence the local structure of turbulence, is completely described by the velocity gradient tensor. The velocity gradient tensor contains other geometric and statistical information such as the alignment of vorticity with respect to the strain-rate eigenvectors, rate of deformation and shapes of fluid material volumes, intermittency, etc. Furthermore in reacting flows, the velocity gradients not only determine the growth rate of flamelet area, but also the flamelet orientation and hence the direction of propagation of the flame (Girimaji & Pope 1990). While obtaining complete information of the local velocity gradient tensor is still not possible in experiments, it is readily obtained in DNS. The results from DNS help in both improving our physical understanding and develop new models applicable to more complex flows (Meneveau 2011).

In the last few decades, the exponential growth of computing power has constantly allowed us to the push the limit of highest Reynolds number achievable in simulations. However, recently this growth in computing is also accompanied by a paradigm shift towards modern architectures involving accelerators such as graphical processing units (GPUs), and Intel Many Integrated Core (MIC). It is evident that achieving even higher Reynolds number will require modern codes capable of exploiting such architectures. While some initial steps have already been taken in this work to port our codes to machines using such architectures, substantial effort will be required in future to utilize them to their full capacity, which may even involve implementing new numerical and parallel approaches from scratch.

The study of fluid particles serves as a good approximation to study dispersion of material in turbulent flows. Similarly, the effects of molecular diffusion are captured reasonably well by the motion of so-called molecules. However in reality, all transported substances also have mass and it is clear that because of inertia effects, suspended solid particles and vapor droplets in multiphase flow also do not follow the same trajectories as fluid particles. The subject of multiphase turbulence (Balachandar & Eaton 2010). is very broad, and additional complexities such as two-way couplings (Ferrante & Elghobashi 2003) for particles of substantial size present at high mass density are well-known. In practical dispersion problems (in contrast to, say, multiphase combustion and sooty flames), because of small particle size and low mass loading two-way couplings are usually unimportant. The important parameter is then the Stokes number (usually defined as ratio of particle time scale to Kolmogorov time scale), which has been studied by other investigators (e.g. Sundaram & Collins 1997; Bec *et al.* 2010). It is well known that inertial particles tend to cluster inhomogeneously even in homogeneous flows (Guha 2008). The study of backward dispersion in this regard is crucial as recently demonstrated by Bragg *et al.* (2016), and still warrants additional investigation.

To conclude, we have developed a new massively parallel computational framework, which has enabled Lagrangian investigations of turbulent dispersion and mixing at Reynolds number higher than previously available in the literature. New insights are found into the physical process of turbulent dispersion, especially from a backward in time reference frame. The backward dispersion of molecules is used to understand turbulent mixing from a Lagrangian perspective across a wide range of Schmidt numbers, a task incredibly difficult from the Eulerian perspective. A key focus of the current work has been to identify and understand the inertial range characteristics of various Lagrangian statistics. All this has been made possible due to the rapid growth of supercomputers in the past decade. The computing power of the upcoming supercomputers holds even greater potential in both expanding our current state of knowledge and enabling new topics of research in turbulence, which were previously inaccessible.

APPENDIX A

SMALL-TIME ASYMPTOTE FOR MOLECULAR PAIRS OF FINITE INITIAL SEPARATION

We work in Cartesian tensor notation, with summation implied over repeated Roman subscripts. Starting with (5.15) and using a Taylor series expansion for the relative velocity under the condition $r(t) \ll \eta$, we can write

$$dr_i(t) = A_{ij}(t) r_j(t) dt + \sqrt{4\kappa} dW_i^{(r)} \ , \tag{A.1}$$

where $A_{ij} = \partial u_i / \partial x_j$ is the velocity gradient tensor. This upon integration gives

$$r_i(t) - r_i(0) = \int_0^t A_{ij}(t) r_j(t) dt + \sqrt{4\kappa} \int_0^t dW_i^{(r)} \ . \tag{A.2}$$

For $t \ll t_\eta$, we can approximate the first term on the r.h.s. to first order and write

$$r_i(t) - r_i(0) = A_{ij}(0) r_j(0) t + \sqrt{4\kappa} W_i^{(r)}(t) \ . \tag{A.3}$$

Now substituting $r_i(t)$ from this into the r.h.s. of (A.1), we get

$$dr_i(t) = A_{ij}(t) \left(r_j(0) + A_{jk}(0) r_k(0) t + \sqrt{4\kappa} W_j^{(r)}(t) \right) dt + \sqrt{4\kappa} dW_i^{(r)}(t) \ . \tag{A.4}$$

The first term can be integrated by approximating the velocity gradient by its value at $t = 0$ again and introducing the integrated Wiener process $\mathbf{W}^{-1}(t)$ (Gardiner 1983) (the function whose time derivatives give $\mathbf{W}(t)$). We obtain

$$r_i(t) - r_i(0) = A_{ij}(0) \left(r_j(0) t + A_{jk}(0) r_k(0) \frac{t^2}{2} + \sqrt{4\kappa} W_j^{-1}(t) \right) + \sqrt{4\kappa} W_i^{(r)}(t) \ . \tag{A.5}$$

By definition $\mathbf{W}^{-1}(t)$ has zero mean and its covariance tensor is equal to $\left\langle W_i^{-1}(t) W_j^{-1}(t) \right\rangle$ $= \delta_{ij} t^3/3$. Now squaring and averaging (A.5), we get, up to $\mathcal{O}(t^3)$

$$\begin{aligned} \langle |\mathbf{r}(t) - \mathbf{r}(0)|^2 \rangle = & \langle A_{ij} A_{il} \rangle r_j(0) r_l(0) \ t^2 + \langle A_{ij} A_{jk} A_{il} \rangle r_k(0) r_l(0) \ t^3 \\ & + 4\kappa \langle W_i^{(r)}(t) W_i^{(r)}(t) \rangle + 4\kappa \langle A_{ij} A_{il} \rangle \langle W_j^{-1}(t) W_l^{-1}(t) \rangle \ , \end{aligned} \tag{A.6}$$

where covariances between velocity gradients and Wiener process are zero since they are independent. To simplify the notation we also omit the dependence on $t = 0$ here and thereafter. Now we can write, $r_i(0) = r_0 e_i$, where r_0 is the initial separation (distance) and e_i is the i-th component of the unit vector along the initial separation vector, with the property $e_i e_i = 1$. Also substituting the covariances of Wiener processes, we obtain

$$\begin{aligned} \langle |\mathbf{r}(t) - \mathbf{r}(0)|^2 \rangle = r_0^2 \left(\langle A_{ij} A_{il} \rangle e_j e_l \ t^2 + \langle A_{ij} A_{jk} A_{il} \rangle e_k e_l \ t^3 \right) \\ + 12\kappa t + 4\kappa \langle A_{ij} A_{il} \rangle \ \delta_{jl} \frac{t^3}{3} \ . \end{aligned} \tag{A.7}$$

Next, to analyze the second and third moments in (A.7) it is useful to note the properties of fourth and sixth order tensors in isotropic incompressible turbulence. In particular, we can write (Pope 2000):

$$F_{ikjl} = \langle A_{ij} A_{kl} \rangle = \alpha \left(2\delta_{ik}\delta_{jl} - \frac{1}{2}\delta_{ij}\delta_{kl} - \frac{1}{2}\delta_{il}\delta_{jk} \right) \ , \tag{A.8}$$

$$\begin{aligned} G_{ijkpqr} = \langle A_{ip} A_{jq} A_{kr} \rangle = \beta \Bigg(& \delta_{ip}\delta_{jq}\delta_{kr} \\ & - \frac{4}{3} \left[\delta_{ip}\delta_{jk}\delta_{qr} + \delta_{jq}\delta_{ik}\delta_{pr} + \delta_{kr}\delta_{ij}\delta_{pq} \right] \\ & - \frac{1}{6} \left[\delta_{ip}\delta_{jr}\delta_{qk} + \delta_{jq}\delta_{ir}\delta_{pk} + \delta_{kr}\delta_{iq}\delta_{pj} \right] \\ & - \frac{3}{4} \left[\delta_{iq}\delta_{pk}\delta_{jr} + \delta_{ir}\delta_{pj}\delta_{qk} \right] \\ & + \left[\delta_{ij}\delta_{pk}\delta_{qr} + \delta_{ij}\delta_{qk}\delta_{pr} + \delta_{ik}\delta_{pj}\delta_{qr} \right. \\ & \left. + \ \delta_{ik}\delta_{rj}\delta_{pq} + \delta_{jk}\delta_{qi}\delta_{pr} + \delta_{jk}\delta_{ri}\delta_{pq} \right] \Bigg) \ . \end{aligned} \tag{A.9}$$

where $\alpha = \langle A_{11}^2 \rangle$ and $\beta = \langle A_{11}^3 \rangle$ are the second and third order moments respectively of A_{11}, i.e., a longitudinal velocity gradient. Standard isotropy relations give $\alpha = \langle \epsilon \rangle / (15\nu)$ and $\beta = S_u \alpha^{3/2}$, where S_u is the skewness of A_{11}. In isotropic turbulence S_u is also equal to the negative of the dissipation skewness S_ϵ (Kerr 1985). By evaluating F_{iijl} and G_{ijijkl}

according to the tensor relations above, we obtain

$$\langle A_{ij} A_{il} \rangle \; e_j e_l = 5\alpha = \frac{1}{3t_\eta^2} \; , \tag{A.10}$$

$$\langle A_{ij} A_{il} \rangle \; \delta_{jl} = 15\alpha = \frac{1}{t_\eta^2} \; , \tag{A.11}$$

$$\langle A_{ij} A_{jk} A_{il} \rangle \; e_k e_l = \frac{35}{6}\beta = -\frac{7}{18\sqrt{15}} \frac{S_\epsilon}{t_\eta^3} \; . \tag{A.12}$$

Substituting these in (A.7), we get

$$\left\langle |\mathbf{r}(t) - \mathbf{r}(0)|^2 \right\rangle = r_0^2 \left[\frac{1}{3} \left(\frac{t}{t_\eta} \right)^2 - \frac{7 \; S_\epsilon}{18\sqrt{15}} \left(\frac{t}{t_\eta} \right)^3 \right] + 12\kappa t + \frac{4}{3}\kappa \frac{t^3}{t_\eta^2} \; , \tag{A.13}$$

In the steps taken so far we have assumed that we are integrating forward in time, such that this formula strictly holds for forward dispersion. To consider backward dispersion, we may replace t by $-t$ on the l.h.s and and in the square bracket on the r.h.s. However, since the last 2 terms in (A.13) represent the non-negative variances of Wiener and integrated Wiener processes, they retain the same sign if t is replaced by $-t$. A result valid for both backward and forward dispersion can thus be written with the absolute value of time $|t|$ in the last two terms of (A.13). Finally, dividing both sides by η^2 recovers the result (5.18), as required.

APPENDIX B

ROBUST APPROACH FOR MOLECULAR DISPLACEMENT STATISTICS IN LAGRANGIAN VIEW OF MIXING

Starting with $Y_i^m(t) = x_i^m(t) - x_i^m(0)$ and using Ito's rule (Gardiner 1983), we can write a stochastic differential equation (SDE) for $Y_i^m Y_i^m$ as

$$d(Y_i^m Y_i^m) = 2Y_i^m dY_i^m + dY_i^m dY_i^m \ . \tag{B.1}$$

Recognizing $dY_i^m = dx_i^m$ and substituting dx_i^m from (5.1), we get

$$d(Y_i^m Y_i^m) = 2Y_i^m (u_i dt + \sqrt{2\kappa} dW_i) + (u_i dt + \sqrt{2\kappa} dW_i)(u_i dt + \sqrt{2\kappa} dW_i) \ \ , \tag{B.2}$$

where u_i is the fluid velocity at the molecular position. Ignoring higher order terms of the form $dtdt$ and $dtdW_i$, and using $dW_i dW_i = \delta_{ii} dt = 3dt$ from the property of Wiener processes, we get

$$d(Y_i^m Y_i^m) = 2Y_i^m u_i dt + 2Y_i^m \sqrt{2\kappa} dW_i + 6\kappa dt \ . \tag{B.3}$$

Taking the ensemble average over the entire population of molecules, the second term on the r.h.s. becomes zero, and the result can be rearranged to give

$$d\langle Y_i^m Y_i^m \rangle / dt = 2\langle Y_i^m u_i \rangle + 6\kappa \ . \tag{B.4}$$

Substituting this result in (5.31) gives

$$P = \frac{2}{3} G^2 \langle Y_i^m u_i \rangle \ . \tag{B.5}$$

Thus we have now obtained an expression for scalar production in terms of the covariance of molecular displacement and fluid velocity at molecular positions, which is easier is calculate reliably.

A similar analysis for molecular pairs would give

$$d\langle r^2 \rangle / dt = 2\langle r_i u_i^{(r)} \rangle + 12\kappa \ , \tag{B.6}$$

which on substituting in (5.30) gives

$$\chi = \frac{1}{3} G^2 \langle r_i u_i^{(r)} \rangle_{r_0(t) \to 0} \quad , \tag{B.7}$$

The expressions for scalar production and dissipation developed in this Appendix have the advantage of avoiding numerical differentiation, which is prone to numerical noise.

Bibliography

Adkins, J. F., McIntyre, K. & Schrag, D. P. (2002). The salinity, temperature, and δ^{18}O of the glacial deep ocean. *Science* **298**, 1769–1773.

Balachandar, S. & Eaton, J. K. (2010). Turbulent dispersed multiphase flow. *Annu. Rev. Fluid Mech.* **42**, 111–133.

Batchelor, G. K. (1949). Diffusion in a field of homogeneous turbulence. I. Eulerian analysis. *Aust. J. Sci. Res.* **2**, 437–450.

Batchelor, G. K. (1950). The application of the similarity theory of turbulence to atmospheric diffusion. *Quart. J. Roy. Meteorol. Soc.* **76**, 133–146.

Batchelor, G. K. (1952).*a* Diffusion in a field of homogeneous turbulence. II. The relative motion of particles. *Proc. Cambr. Philos. Soc.* **48**, 345–362.

Batchelor, G. K. (1952).*b* The effect of homogeneous turbulence on material lines and surfaces. *Proc. Roy. Soc. Lond., Ser. A* **213**, 349–366.

Batchelor, G. K. (1953). *The Theory of Homogeneous Turbulence*. Cambridge, U.K.: Cambridge University Press.

Batchelor, G. K. (1959). Small-scale variation of convected quantities like temperature in turbulent fluid .1. General discussion and the case of small conductivity. *J. Fluid Mech.* **5**, 113–133.

Batchelor, G. K., Howells, I. D. & Townsend, A. A. (1959). Small-scale variation of convected quantities like temperature in turbulent fluid .2. The case of large conductivity. *J. Fluid Mech.* **5**, 134–139.

Bec, J., Biferale, L., Lanotte, A. S., Scagliarini, A. & Toschi, F. (2010). Turbulent pair dispersion of inertial particles. *J. Fluid Mech.* **645**, 497–528.

Benveniste, D. & Drivas, T. D. (2014). Asymptotic results for backwards two-particle dispersion in turbulent flow. *Phys. Rev. E* **89**, 041003.

Berg, J., Luthi, B., Mann, J. & Ott, S. (2006). Backwards and forwards relative dispersion in turbulent flow: An experimental investigation. *Phys. Rev. E* **74**, 016304.

Bernard, D., Gawedzki, K. & Kupiainen, A. (1998). Slow modes in passive advection. *J. Stat. Phys.* **90**, 519–569.

Biferale, L., Boffetta, G., Celani, A., Devenish, B. J., Lanotte, A. & Toschi, F. (2005). Multiparticle dispersion in fully developed turbulence. *Phys. Fluids* **17**, 111701.

Bitane, R., Homann, H. & Bec, J. (2012). Time scales of turbulent relative dispersion. *Phys. Rev. E* **86**, 045302.

Bitane, R., Homann, H. & Bec, J. (2013). Geometry and violent events in turbulent pair dispersion. *J. Turb.* **14** (2), 23 – 45.

Bodenschatz, E., Malinowski, S.P, Shaw, R. A. & Stratmann, F. (2010). Can we understand clouds without turbulence? *Science* **327**, 970–971.

Borgas, M. S. & Sawford, B. L. (1991). The small-scale structure of acceleration correlations and its role in the statistical theory of turbulent dispersion. *J. Fluid Mech.* **228**, 295.

Borgas, M. S. & Sawford, B. L. (1996). Molecular diffusion and viscous effects on concentration statistics in grid turbulence. *J. Fluid Mech.* **324**, 25–54.

Borgas, M. S., Sawford, B. L., Xu, S., Donzis, D. A. & Yeung, P. K. (2004). High Schmidt number scalars in turbulence: structure functions and Lagrangian theory. *Phys. Fluids* **16**, 3888–3899.

Borgas, M. S. & Yeung, P. K. (2004). Relative dispersion in isotropic turbulence: Part 2. A new stochastic model with Reynolds number dependence. *J. Fluid Mech.* **503**, 125–160.

Bourgoin, M. (2015). Turbulent pair dispersion as a ballistic cascade phenomenology. *J. Fluid Mech.* **772**, 678 – 704.

Bragg, A. D., Ireland, P. J. & Collins, L. R. (2016). Forward and backward in time dispersion of fluid and inertial particles in isotropic turbulence. *Phys. Fluids* **28**, 013305.

Buaria, D., Sawford, B. L. & Yeung, P. K. (2015). Characteristics of backward and forward two-particle relative dispersion in turbulence at different reynolds numbers. *Phys. Fluids* **27**, 105101.

Buaria, D. & Yeung, P. K. (2014). Challenges in particle tracking in turbulence on a massive scale. In *Proc. of the 2014 Annual Conference on Extreme Science and Engineering Discovery Environment*. Atlanta, GA.

Canuto, C., Hussaini, M. Y., Quarteroni, A. & Zang, T. A. (1987). *Spectral Methods in Fluid Dynamics*. Springer-Verlag.

Castiglione, P. & Pumir, A. (2001). Evolution of triangles in a two-dimensional turbulent flow. *Phys. Rev. E* **64**, 056303.

Chan, A., Balaji, P., Gropp, W. & Thakur, R. (2008). Communication analysis of parallel 3D FFT for flat Cartesian meshes on large Blue Gene systems. In *15th IEEE Int. Conf. on High Perf. Comp.*, pp. 422–429.

Chang, K., Malec, B. J. & Shaw, R. A. (2015). Turbulent pair dispersion in the presence of gravity. *New J. Phys.* **17**, 033010.

Charbonnel, C. & Talon, S. (2007). Mixing a stellar cocktail. *Science* **318**, 922–923.

Chertkov, M., Pumir, A. & Shraiman, B. I. (1999). Lagrangian tetrad dynamics and the phenomenology of turbulence. *Phys. Fluids* **11**, 2394–2410.

Coarfa, C., Dotsenko, Y., Mellor-Crummey, J., Cantonnet, F., El-Ghazawi, T., Mohanti, A., Yao, Y. & Chavarría-Miranda, D. (2005). An evaluation of global address space languages: Co-array fortran and unified parallel c. In *Proceedings of the*

Tenth ACM SIGPLAN Symposium on Principles and Practice of Parallel Programming, pp. 36–47. New York, NY, USA: ACM.

Cooley, J. W. & Tukey, J. W. (1965). An algorithm for the machine calculation of complex Fourier series. *Math. Comput.* pp. 297–301.

Corrsin, S. (1952). Heat transfer in isotropic turbulence. *J. Appl. Phys.* **23**, 113–118.

Crimaldi, J.P. & Browning, H.S. (2004). A proposed mechanism for turbulent enhancement of broadcast spawning efficiency. *J. Marine Syst.* **49**, 3 – 18.

Crimaldi, J. P. (2012). The role of structured stirring and mixing on gamete dispersal and aggregation in broadcast spawning. *J. Exp. Biol.* **215**, 1031–1039.

Czechowski, T., McClanahan, C., Battaglino, C., Iyer, K. P., Yeung, P. K. & R., Vuduc (2012). On the communication complexity of 3D FFTs and its implications for exascale. In *Proc. ACM Int'l. Conf. Supercomputing (ICS)*. San Servolo Island, Venice, Italy.

Dimotakis, P. E. (2005). Turbulent mixing. *Annu. Rev. Fluid Mech.* **37**, 329–356.

Donzis, D. A., Sreenivasan, K. R. & Yeung, P. K. (2005). Scalar dissipation rate and dissipative anomaly in isotropic turbulence. *J. Fluid Mech.* **532**, 199–216.

Donzis, D. A., Sreenivasan, K. R. & Yeung, P. K. (2010). The Batchelor spectrum for mixing of passive scalars in isotropic turbulence. *Flow, Turb. & Combust.* **85**, 549–566.

Donzis, D. A. & Yeung, P. K. (2010). Resolution effects and scaling in numerical simulations of passive scalar mixing in turbulence. *Physica D* **239**, 1278–1287.

Donzis, D. A., Yeung, P. K. & Pekurovsky, D. (2008). Turbulence simulations on $O(10^4)$ processors. In *Proc. TeraGrid '08 Conf.*.

Dubey, A. & Tessera, D. (2001). Redistribution strategies for portable parallel fft: a case study. *Concurrency and Computation: Practice and Experience* **13**, 209–220.

Durbin, P. A. (1980). A stochastic model of 2-particle dispersion and concentration fluctuations in homogeneous turbulence. *J. Fluid Mech.* **100**, 279–302.

Durham, W. M., Climent, E., Barry, M., Lillo, F. De, Boffetta, G., Cenceni, M. & Stocker, R. (2013). Turbulence drives microscale patches of motile phytoplankton. *Nature Comm.* **4**.

Enos, J., Bauer, G., Brunner, R., Islam, S., Fiedler, R. A., Steed, M. & Jackson, D. (2014). Topology-aware job scheduling strategies for Torus networks. In *Cray User Group Proc.*. Switzerland.

Eswaran, V. & Pope, S. B. (1988). An examination of forcing in direct numerical simulations of turbulence. *Comput. Fluids* **16**, 257–278.

Eyink, G. (2011). Stochastic flux freezing and magnetic dynamo. *Phys. Rev. E* **83**, 056405.

Eyink, G. & Benveniste, D. (2013). Diffusion approximation in turbulent two-particle dispersion. *Phys. Rev. E* **88**, 041001(R).

Falkovich, G., Gawadzki, K. & Vergassola, M. (2001). Particles and fields in fluid turbulence. *Rev. Mod. Phys.* **73**, 913–975.

Ferrante, A. & Elghobashi, S. (2003). On the physical mechanisms of two-way coupling in particle-laden isotropic turbulence. *Phys. Fluids* **15** (2), 315–329.

Fiedler, R. A., Wichmann, N., Whaeln, S. & Pekurovsky, D. (2013). Improving the performance of the PSDNS pseudo-spectral turbulence application of Blue Waters using Coarray Fortran and task placement. In *Cray User Group Proc.*. Napa Valley, CA.

Foster, T. & Worley, H. (1997). Parallel algorithms for the spectral transform method. *SIAM J. Sci. Comput.* **18**, 806–837.

Frigo, Matteo & Johnson, Steven G. (2005). The design and implementation of FFTW3. *Proceedings of the IEEE* **93** (2), 216–231, special issue on "Program Generation, Optimization, and Platform Adaptation".

Frisch, U. (1995). *Turbulence*. Cambridge University Press.

Frisch, U., Mazzino, A., Noullez, A. & Vergassola, M. (1999). Lagrangian method for multiple correlations in passive scalar advection. *Phys. Fluids* **11**, 2178–2186.

Galanti, B. & Tsinober, A. (2004). Is turbulence ergodic? *Phys. Lett. A* **330**, 173 – 180.

Garabato, A. C. N., Polzin, K. L., King, B. A., Heywood, K. J. & Visbeck, M. (2004). Widespread intense turbulent mixing in the southern ocean. *Science* **303**, 210–213.

Gardiner, C. (1983). *Handbook of Stochastic Methods for Physics, Chemistry and the Natural Sciences*. Berlin: Springer.

Garrett, C. (2003). Internal tides and ocean mixing. *Science* **301**, 1858–1859.

Girimaji, S. S. & Pope, S. B. (1990). A diffusion model for velocity gradients in turbulence. *Physics of Fluids A: Fluid Dynamics (1989-1993)* **2** (2), 242–256.

Grassberger, P. & Procaccia, I. (1983). Measuring the strangeness of strange attractors. *Physica D* **9**, 189–208.

Griffa, A. (1996). Applications of stochastic particle models to oceanographic problems. In *Stochastic Modelling in Physical Oceanography* (ed. R. J. Adler, P. Müller & B. L. Rozovskii), pp. 113–140. Cambridge, MA, USA: Birkhauser Boston Inc.

Guha, A. (2008). Transport and deposition of particles in turbulent and laminar flow. *Annu. Rev. Fluid Mech.* **40**, 311–341.

Hackl, J. F., Yeung, P. K. & Sawford, B. L. (2011). Multi-particle and tetrad statistics in numerical simulations of turbulent relative dispersion. *Phys. Fluids* **23**, 065103.

Humphreys, R. M. & Davidson, K. (1984). The most luminous stars. *Science* **223**, 243–249.

Ireland., P. J., Vaithianathan, T., Sukheswalla, P. S., Ray, B. & Collins, L. (2013). Highly parallel particle-laden flow solver for turbulence research. *Comput. Fluids* **76**, 170–177.

Iribarne, J. J. V. & Cho, H. H. R. (1980). *Atmospheric Physics*. D. Reidel Publishing Company.

Ishihara, T., Gotoh, T. & Kaneda, Y. (2009). Study of high-Reynolds number isotropic turbulence by direct numerical simulation. *Annu. Rev. Fluid Mech.* **41**, 165–180.

Ishihara, T. & Kaneda, Y. (2002). Relative diffusion of a pair of fluid particles in the inertial range of turbulence. *Phys. Fluids* **14**, L69.

Jucha, J., Xu, H., Pumir, A. & Bodenschatz, E. (2014). Time-reversal-symmetry breaking in turbulence. *Phys. Rev. Lett.* **113**, 054501.

Juneja, A. & Pope, S. B. (1996). A DNS study of turbulent mixing of two passive scalars. *Phys. Fluids* **8**, 2161–2184.

Kaneda, Y., Ishihara, T., Yokokawa, M., Itakura, K. & Uno, A. (2003). Energy dissipation rate and energy spectrum in high resolution direct numerical simulations of turbulence in a periodic box. *Phys. Fluids* **15**, L21–L24.

Kawahara, G. (2005). Energy dissipation in spiral vortex layers wrapped around a straight vortex tube. *Phys. Fluids* **17**, 055111.

Kerr, R. M. (1985). Higher-order derivative correlations and the alignment of small-scale structures in isotropic numerical turbulence. *J. Fluid Mech.* **153**, 31–58.

Kloeden, P.E. & Platen, E. (1992). *Numerical Solution of Stochastic Differential Equations*. Springer-Verlag.

Kolmogorov, A. N. (1941). The local structure of turbulence in an incompressible fluid with very large reynolds numbers. *Dokl. Akad. Nauk SSSR* **30**, 301–305.

Kumar, S., Sabharwal, Y & Heidelberger, P. (2008). Optimization of all-to-all communication on the blue gene/l supercomputer. *International Conference on Parallel Processing* pp. 320–329.

Lumley, J. L. & Yaglom, A. M. (2001). A century of turbulence **66**, 241–286.

Luthi, B., Ott, S. & Mann, J. (2007). Lagrangian multi-particle statistics. *J. Turb.* **8**, 45.

L'vov, V. S., Podivilov, E. & Procaccia, I. (1997). Temporal multiscaling in hydrodynamic turbulence. *Phys. Rev. E* **55**, 7030–7035.

Meneveau, C. (2011). Lagrangian dynamics and models of the velocity gradient tensor in turbulent flows. *Annu. Rev. Fluid Mech.* **43**, 219–245.

Moin, P & Mahesh, K (1998). Direct numerical simulation: A tool in turbulence research. *Annu. Rev. Fluid Mech.* **30**, 539–578.

Monin, A. S. & Yaglom, A. M. (1971). *Statistical Fluid Mechanics, Vol. 1*. MIT Press.

MONIN, A. S. & YAGLOM, A. M. (1975). *Statistical Fluid Mechanics, Vol. 2*. MIT Press.

MOORE, G. E. (1965). Cramming more components onto integrated circuits. *Electronics* **38** (8).

OBUKHOV, A. M. (1941). Spectral energy distribution in a turbulent flow. *Izv. Akad. Nauk. SSSR* **5**, 453–466.

OTT, S. & MANN, J. (2000). An experimental investigation of the relative diffusion of particle pairs in three-dimensional turbulent flow. *J. Fluid Mech.* **422**, 207–223.

OUELLETTE, N. T., XU, H., BOURGOIN, M. & BODENSCHATZ, E. (2006). An experimental study of turbulent relative dispersion models. *New J. Phys.* **8**, 109.

OVERHOLT, M. R. & POPE, S. B. (1996). Direct numerical simulation of a passive scalar with imposed mean gradient in isotropic turbulence. *Phys. Fluids* **8**, 3128–3148.

PAPAVASSILIOU, D. V. & HANRATTY, T. J. (1995). Synthesis of temperature fields in terms of the behavior of instantaneous wall sources. *Proc. Tenth Symp. on Turbulent Shear Flows* pp. 31–19–31–24.

PEKUROVSKY, D. (2012). P3DFFT: A framework for parallel computations of Fourier transforms in three dimensions. *SIAM J. Sci. comp.* pp. C192–C209.

PEYRET, R. & TAYLOR, T. D. (1983). *Computational Methods for Fluid Flow*. Springer-Verlag.

PHILLIPS, J. C., BRAUN, R., WANG, W., GUMBART, J., TAJKHORSHID, E., VILLA, E., CHIPOT, C., SKEEL, R. D., KALE, L. & SCHULTEN, K. (2005). Scalable molecular dynamics with NAMD. *J. Comput. Chem.* **26**, 1781–1802.

PICKARD, G. L. & EMERY, W. J. (1990). *Descriptive Physical Oceanography: An Introduction*. Butterworth-Heinemann.

PLETCHER, R. H., TANNEHILL, J. C. & ANDERSON, D. A. (2012). *Computational Fluid Mechanics and Heat Transfer, Third Edition*. CRC Press.

PLIMPTON, S. (1995). Fast parallel algorithms for short-range molecular dynamics. *J. Comput. Phys.* **117**, 1–19.

POPE, S. B. (1994). Lagrangian pdf methods for turbulent flows. *Annu. Rev. Fluid Mech.* **26**, 23–63.

POPE, S. B. (1998). The vanishing effect of molecular diffusivity on turbulent dispersion: Implications for turublent mixing and scalar flux. *J. Fluid Mech.* **359**, 299–312.

POPE, S. B. (2000). *Turbulent Flows*. Cambridge University Press.

PUMIR, A., SHRAIMAN, B. I. & CHERKTOV, M. (2001). The Lagrangian view of energy transfer in turbulent flow. *Europhys. Lett.* **56**, 379–385.

PUMIR, A., SHRAIMAN, B. I. & CHERTKOV, M. (2000). Geometry of Lagrangian dispersion in turbulence. *Phys. Rev. Lett.* **85**, 5324–7.

Richardson, L. F. (1926). Atmospheric diffusion shown on a distance neighbor graph. *Proc. Roy. Soc. Lond., Ser. A* **110**, 709–737.

Riley, J. J. & Patterson, G. S. (1974). Diffusion experiments with numerically integrated isotropic turbulence. *Phys. Fluids* **17**, 292–297.

Rodean, H. C. (1996). *Stochastic Lagrangian Models of Turbulent Diffusion*, *Meteorological Monographs*, vol. 48. Am. Meteor. Soc.

Rogallo, R. S. (1981). Numerical experiments in homogeneous turbulence. *NASA Tech. Memo 81315* .

Ryu, D., Kang, H., Cho, J. & Das, S. (2008). Turbulence and magnetic fields in the large-scale structure of the universe. *Science* **320**, 909–912.

Saffman, P. G. (1960). On the effect of the molecular diffusivity in turbulent diffusion. *J. Fluid Mech.* **8**, 273–283.

Salazar, J. P. L. C. & Collins, L. R. (2009). Two-particle dispersion in isotropic turbulent flows. *Annu. Rev. Fluid Mech.* **41**, 405–432.

Sawford, B. L. (1985). Lagrangian statistical simulation of concentration mean and fluctuation fields. *J. Climat. Appl. Meteorol.* **24**, 1152–1166.

Sawford, B. L. (1993). Recent developments in the lagrangian stochastic theory of turbulent dispersion. *Boundary-Layer Meteorol.* **62**, 197–215.

Sawford, B. L. (2001). Turbulent relative dispersion. *Annu. Rev. Fluid Mech.* **33**, 289–317.

Sawford, B. L. & Hunt, J. C. R. (1986). Effects of turbulence structure, molecular diffusion and source size on scalar fluctuations in homogeneous turbulene. *J. Fluid Mech.* **165**, 373–400.

Sawford, B. L. & Pinton, J.-F. (2013). A Lagrangian View of Turbulent Dispersion and Mixing. In *Ten Chapters in Turbulence* (ed. P. A. Davidson, Y. Kaneda & K. R. Sreenivasan). Cambridge University Press.

Sawford, B. L., Pope, S. B. & Yeung, P. K. (2013). Gaussian Lagrangian stochastic models for multi-particle dispersion. *Phys. Fluids* **25**, 055101.

Sawford, B. L. & Yeung, P. K. (2011). Kolmogorov similarity scaling for one-particle lagrangian statistics. *Phys. Fluids* **23**, 091704.

Sawford, B. L., Yeung, P. K. & Borgas, M. S. (2005). Comparsion of backwards and forwards relative dispersion in turbulence. *Phys. Fluids* **17**, 095109.

Sawford, B. L., Yeung, P. K. & Hackl, J. F. (2008). Reynolds number dependence of relative dispersion statistics in isotropic turbulence. *Phys. Fluids* **20**, 065111.

Shaw, R. (2003). Particle-turbulence interactions in atmospheric clouds. *Annu. Rev. Fluid Mech.* **35**, 183–227.

Shraiman, B. I. & Siggia, E. D. (1998). Anomalous scaling for a passive scalarr near the batchelor limit. *Phys. Rev. E* **57**, 2965–2977.

Sreenivasan, K. R. (1995). On the universality of the Kolmogorov constant. *Phys. Fluids* **7**, 2778–2784.

Sreenivasan, K. R. (1998). An update on the energy dissipation rate in isotropic turbulence. *Phys. Fluids* **10**, 528–529.

Sreenivasan, K. R. (1999). Fluid turbulence. *Rev. Mod. Phys.* **71**, s383–s395.

Srinivasan, C. & Papavassiliou, D. V. (2012). Comparsion of backwards and forwards scalar relative dispersion in turbulent shear flow. *Int. J. Heat & Mass Transf.* **55**, 5650–5664.

Sundaram, S. & Collins, L. R. (1997). Collision statistics in an isotropic particle-laden turbulent suspension. part 1. direct numerical simulations. *Journal of Fluid Mechanics* **335**, 75–109.

Taylor, G. I. (1921). Diffusion by continuous movements. *Proc. Lond. Math. Soc.* **20**, 196–202.

Tennekes, H. (1975). Eulerian and lagrangian time microscales in isotropic turbulence. *J. Fluid Mech.* **67**, 561–567.

Thomson, D. J. (1990). A stochastic model for the motion of particle pairs in isotropic high-reynolds-number turbulence, and its application to the problem of concentration variance. *J. Fluid Mech.* **210**, 113–153.

Toschi, F. & Bodenschatz, E. (2009). Lagrangian properties of particles in turbulence. *Annu. Rev. Fluid Mech.* **41**, 375–404.

Tsuji, M. & Sato, M. (2009). Performance evaluation of OpenMP and MPI hybrid programs on a large scale multi-core multi-socket cluster, T2K Open Supercomputer. In *Int. Conf. on Parallel Process. Workshops (ICPPW 2009)*, pp. 206–213. IEEE.

Visser, A. W. (2007). Biomixing of the oceans? *Science* **316**, 838–839.

Ward-Thompson, D. (2002). Isolated star formation: from cloud formation to core collapse. *Science* **295**, 76–81.

Warhaft, Z. (2009). Why we need experiments at high Reynolds numbers. *Fluid Dyn. Res.* **41**, 021401.

Watanabe, T. & Gotoh, T. (2006). Intermittency in passive scalar turbulence under the uniform mean scalar gradient. *Phys. Fluids* **18**, 058105.

Wilson, J. D. & Sawford, B. L. (1996). Review of lagrangian stochastic models for trajectories in the turbulent atmosphere. *Boundary-Layer Meteorology* **78** (1), 191–210.

Wunsch, C. (2002). What is the thermohaline circulation? *Science* **298**, 1179–1181.

Wunsch, C. & Ferrari, R. (2004). Vertical mixing, energy, and the general circulation of the oceans. *Annu. Rev. Fluid Mech.* **36**, 281–314.

Xu, H., Ouellette, N. T. & Bodenschatz, E. (2008). Evolution of geometric structures in intense turbulence. *New J. Phys.* **10**, 013012.

Yeung, P. K. (1994). Direct numerical simulation of two-particle relative dispersion in isotropic turbulence. *Phys. Fluids* **6**, 3416–3418.

Yeung, P. K. (1996). Multi-scalar triadic interactions in differential diffusion with and without mean scalar gradients. *J. Fluid Mech.* **321**, 235–278.

Yeung, P. K. (2002). Lagrangian investigations of turbulence. *Annu. Rev. Fluid Mech.* **34**, 115–142.

Yeung, P. K. & Borgas, M. S. (1997). Molecular path statistics in turbulence: simulation and modeling. In *Int. Conf. on DNS and LES*. Ruston, LA.

Yeung, P. K. & Borgas, M. S. (2004). Relative dispersion in isotropic turbulence: Part 1. Direct numerical simulations and Reynolds number dependence. *J. Fluid Mech.* **503**, 93–124.

Yeung, P. K., Donzis, D. A. & Sreenivasan, K. R. (2012). Dissipation, enstrophy and pressure statistics in turbulence simulations at high Reynolds numbers. *J. Fluid Mech.* **700**, 5 – 15.

Yeung, P. K. & Pope, S. B. (1988). An algorithm for tracking fluid particles in numerical simulations of homogeneous turbulence. *J. Comput. Phys.* **79**, 373–416.

Yeung, P. K. & Pope, S. B. (1989). Lagrangian statistics from direct numerical simulations of isotropic turbulence. *J. Fluid Mech.* **207**, 531–586.

Yeung, P. K. & Pope, S. B. (1993). Differential diffusion of passive scalars in isotropic turbulence. *Phys. Fluids A* **5**, 2467–2478.

Yeung, P. K., Pope, S. B., Lamorgese, A. G. & Donzis, D. A. (2006a). Acceleration and dissipation statistics of numerically simulated isotropic turbulence. *Phys. Fluids* **18**, 065103.

Yeung, P. K., Pope, S. B. & Sawford, B. L. (2006b). Reynolds number dependence of Lagrangian statistics in large numerical simulations of isotropic turbulence. *J. Turb.* **7(58)**, 1–12.

Yeung, P. K. & Sreenivasan, K. R. (2013). Spectrum of passive scalars of high molecular diffusivity in turbulent mixing. *J. Fluid Mech.* **716**, R14.

Yeung, P. K. & Sreenivasan, K. R. (2014). Direct numerical simulation of turbulent mixing at very low Schmidt number with a uniform mean gradient. *Phys. Fluids* **26**, 015107.

Yeung, P. K., Xu, S. & Sreenivasan, K. R. (2002). Schmidt number effects on turbulent transport with uniform mean scalar gradient. *Phys. Fluids* **14**, 4178–4191.

Yeung, P. K., Zhai, X. M. & Sreenivasan, K. R. (2015). Extreme events in computational turbulence. *Proceedings of the National Academy of Sciences* **112** (41), 12633–12638.

Yeung, P. K. & Zhou, Y. (1997). Universality of the Kolmogorov constant in numerical simulations of turbulence. *Phys. Rev. E* **56**, 1746–1752.

Yokokawa, M., Itakura, T., Uno, A., Ishihara, T. & Kaneda, Y. (2002). 16.4-Tflops direct numerical simulation of turbulence by a fourier spectral method on the earth simulator. In *Proceedings of the Supercomputing Conference*. Baltimore.

Zeldovich, Y. B., Ruzmaikin, A. A., Molchanov, S. A. & Sokoloff, D. D. (1984). Kinematic dynamo problem in a linear velocity field. *J. Fluid Mech.* **144**, 1–11.